PHOTONIC CRYSTAL CAVITIES FOR SPECTRALLY-SELECTIVE OPTOELECTRONIC DEVICES

by

HONGJUN YANG

Presented to the Faculty of the Graduate School of
The University of Texas at Arlington in Partial Fulfillment
of the Requirements
for the Degree of

DOCTOR OF PHILOSOPHY

THE UNIVERSITY OF TEXAS AT ARLINGTON
May 2010

ACKNOWLEDGEMENTS

My study at the University of Texas at Arlington is the greatest adventure that I could ever have imagined! I must express my foremost gratitude and appreciation to my PhD advisor, Dr. Weidong Zhou, who introduces me to the wonderful world of photonic crystals in the first place and led me through the study with his inspiration, insight, and encouragement. This dissertation would not have been possible without his continuous guidance and support. Besides his instruction to my research itself, he also inspires me a lot with his passion to research and positive attitude towards life.

I would also like to thank the other members of my dissertation committee, Dr. Donald Butler, Dr. Robert Magnusson, Dr. Michael Vasilyev and Dr. Seong Jin Koh for their advice and guidance. I also thank my graduate advisor Dr. William E. Dillon for his tireless advice in the past five years.

I would like to gratefully acknowledge Dr. Zhenqiang Ma at University of Wisconsin-Madison, Dr. Adrienne Stiff-Roberts at Duke University, Dr. Sanjay Krishna at the University of New Mexico and their labs, for the remarkable collaboration on Si nanomembrane transfer technique and GaAs quantum well/dot materials growth.

The past and present Nanophotonic Lab (NPLAB) members are acknowledged for their consistent help and encouragement. I would like to start by thanking the postdoc members, Dr. Zexuan Qiang, Dr. Deyin Zhao and Dr. Weiquan Yang for their willingness to help when needed. A very special gratitude goes to Santhad Chuwongin for his talent in drawing. I would like to thank Li Chen, who is my classmate, friend, labmate, and officemate, for educating me with his broad knowledge and for accompanying me the whole time.

A significant amount of my projects have been done in the NNIN facilities in the University of Texas at Austin. People there have contributed a lot to my projects. Their time and advice have been invaluable to this study. Particularly, I thank my friends Yurun Liu and Hao Ju for their accommodation during my stay in Austin and our true friendship is the treasure I would like to own and appreciate forever.

I am grateful for the funding support from DoD AFOSR MURI Program, AFRL CONTACT program, NASA TSGC New Investigator Program, NSF Nano-manufacturingAFOSR Nano Program AFOSR/AFRL SPRING Program, UTA Research Enhancement Program and travel grants from Rice University. Without their sponsorship, nothing could be done in our research.

The entire NanoFAB staff is also grateful acknowledged.

Last but not least, I thank my family for their unconditional love and enthusiastic support during my life. I also give my tremendous thanks to my elder brother and my two elder sisters, their love and care to me and to my parents make me peace in life and vigor in research.

April 16, 2010

ABSTRACT

PHOTONIC CRYSTAL CAVITIES FOR SPECTRALLY-SELECTIVE OPTOELECTRONIC DEVICES

Hongjun Yang, PhD

The University of Texas at Arlington, 2010

Supervising Professor: Weidong Zhou

Photonic crystal (PC) structures exhibit unconventional dispersion and refractive properties making possible hitherto not realizable optical and optoelectronic devices with high spectral selectivity. Functional PC devices (e.g., optical filters, reflectors, and photo detectors and light emitters) on both Si and III-V semiconductor material systems were fabricated via E-Beam lithography (EBL). The device layer can be further transferred onto foreign substrates such as glass or plastic (PET), using a low-cost “wet nanomembrane transfer technique” developed in this study.

The broadband membrane reflectors (MR) based on Fano resonances in patterned silicon nanomembranes have been demonstrated. Resonance control of the reflectors was realized either by partially removing buried oxide layer underneath the device layer, or by controlled SiO_2 film deposition on the top of the devices. Both blue- and red-shifts were demonstrated with a turning range of 50 nm for a center wavelength at 1550 nm. These results demonstrate practical post-process means for Fano resonance engineering for both narrow band filters and ultra-compact broadband reflectors.

An optically pumped resonance cavity light emitting device (RCLED) with Si based membrane reflectors (MR) has been demonstrated experimentally. The stimulated cavity mode at 1545 nm was observed at room temperature with a pulsed green pumping laser light source. We observed significant spectral narrowing in RCLEDs with linewidth reduced from 50 nm down to <4 nm, owing to the presence of top and bottom MR reflectors. The measured photoluminescence efficiency also increased by a factor of 100 in RCLEDs, as compared to the value measured from as-grown InGaAsP QW structures on InP substrate. The mode shifts were also investigated over different temperatures and different pumping power levels.

An InGaAsP QW LED array device was also fabricated and transferred onto flexible PET substrate. The devices showed very good electrical and optical performances, based measured L-I-V (light-current-voltage) characteristics and spectral and near field images. All these work can lead to the demonstration of an electrically pumped membrane-reflector vertical-cavity surface-emitting laser (MR-VCSEL).

TABLE OF CONTENTS

ACKNOWLEDGEMENTS iii

ABSTRACT v

LIST OF ILLUSTRATIONS x

LIST OF TABLES xv

Chapter Page

1. INTRODUCTION 1
    - 1.1 Photonic Crystals 1
        - 1.1.1 Periodic Structures 1
        - 1.1.2 Photonic Bandgap 2
    - 1.2 Photonic Crystals for Spectrally-Selective Infrared Photodetectors 3
    - 1.3 Photonic Crystals for Spectrally-Selective Light Sources 6
2. GAAS-BASED PHOTONIC CRYSTAL INFRARED PHOTODETECTORS 8
    - 2.1 Introduction 8
    - 2.2 InGaAs/GaAs Quantum Dot Heterstructure 9
    - 2.3 Photonic Crystal Cavity Designs 13
    - 2.4 QD-PCIP Fabrication 15
    - 2.5 Device Characteristics 18
3. SI-BASED FANO-RESONANCE FILTERS 22
    - 3.1 Introduction 22
    - 3.2 3D-FDTD Simulation 23
    - 3.3 EBL Fabrication 24
    - 3.4 Membrane Transfer Technique 26
    - 3.5 Device Characteristics 29

4. SI-BASED MEMBRANE REFLECTORS 40

4.1 Introduction.. 40

4.2 Membrane Reflector Design 41

4.3 Device Fabrication 43

4.4 Device Characteristics and Resonance Control 44

4.5 Potential Applications 51

5. MR-VCSELS 52

5.1 Introduction.. 52

5.2 Top/Bottom MR And Cavity Designs 54

5.3 Components Fabrication and Intergration.. 58

5.3.1 InGaAsP QW Mesa Fabrication 58

5.3.2 MR mirrors Fabrication.. 62

5.3.3 Optically Pumped MR-VCSEL Integration 65

5.4 Device Characteristics 66

5.4.1 MR Resonance Cavity Light Emitting Device (RCLED)................. 66

5.4.2 InGaAsP QW LED Array on PET 70

5.5 Conclusions.. 73

6. CONCLUSIONS AND FUTURE WORK 74

6.1 Research Summary 74

6.1.1 GaAs-based Photonic Crystal (PC) Cavity with the Quantum Dot Infrared Photodetector (QDIP).. 75

6.1.2 Si-based Fano-resonance Filters 75

6.1.3 Si-based Membrance Reflectors.. 76

6.1.4 MR-VCSELs.. 76

6.2 Suggestions for Future Work 77

6.2.1 High Performance Optical Modulators 77

6.2.2 Flexible Electrically Pumped MR-VCSEL 77

6.3 Conclusion...78

APPENDIX

A. ABBREVIATIONS 79

B. PUBLICATIONS..82

REFERENCES 90

BIOGRAPHICAL INFORMATION 99

LIST OF ILLUSTRATIONS

Figure Page

1.1 Schematic of photonic crystal structures: (a) one dimensional-PC (1D), (b) two dimensional-PC (2D), and (b) three dimensional-PC (3D). 1

1.2 Schematic of 2D photonic crystal slab (PCS) with square lattice air hole structure... 2

1.3 Calculated photonic crystal bandgap structures with different parameters. (a) a=0.96μm, r/a=0.4, t=1.34μm, n_{high}=3.4, n_{low}=1.0; and (b) a=1.94μm, r/a=0.4, t=1.34μm, n_{high}=3.4, n_{low}=1.0.. 3

2.1 Schematic PC-QDIP (a) designed classic QDIP structure; (b) PC structure formed in QD substrate and (c) defined PC-QDIP structure. 9

2.2 InGaAs/GaAs QD Heterostructure: (a) Schematic the quantum dot (QD) n-i-n heterostructure (b) transmission electron microscope (TEM) image and atomic force microscope (AFM) image of the epitaxial QDs.. 10

2.3 Schematic level diagrams (a) bound-to-bound state transition and (b) bound-to-continuum state transition in a biased quantum-dot infrared photodetector (QDIP). 11

2.4 Room-temperature photoluminescence (PL) for QDs heterostructure 12

2.5 The measured internal absorption quantum efficiency (no grating or cavity effects) for a 30-stack DWELL QDIP 12

2.6 (a) Photonic crystal bandgap (PCB) in the dispersion diagram (triangle lattice) and symmetric photonic crystal slab under simulation, with an absorptive layer in the center of the slab; (b) Simulation configurations with perfectly matched layers (PML) 13

2.7 (a) normalized surface normal absorption power in a single defect photonic crystal cavity for different absorption values; (b) absorption enhancement factor for different absorption values in single defect (H1) and defect free (H0) cavities. Note the dominant absorption enhancement is along vertical direction 14

2.8 Calculated Photonic Crystal Bandgap (PCB) Structure based on expension theory with: (a) a=3.33 μm; t=1.6 μm; n_{low}=1.0; n_{high}=3.4; λ_{min}=9.82 μm; λ_{max}=12.41 μm; λ_{center}=11.12 μm; and (b) a=4.19 μm; t=1.6 μm; n_{low}=1.0; n_{high}=3.4; λ_{min}=9.07 μm; λ_{max}=12.95 μm λ_{center}=11.01μm 15

2.9 Scanning electron microscope (SEM) images of EBL pattern with various defect modes: Defect Free (H0), Single Defect (H1) and couple Defect (C3H3). 16

2.10 Schematic of photonic crystal (PC) cavity quantum dot infrared photodetector (QDIP): 1. Side view of QD substrate with PC pattern formed; 2. Side view of device with top n ring metal deposited; 3. Side view of device with mesa etched into bottom contact layer; 4. Side view of fabricated device with both top and bottom contact metal coated. 17

2.11 Scanning electron microscopy (SEM) and microscope top view images of fabricated device under wire bonding. 18

2.12 Measured current-voltage (I-V) characteristics at different temperatures (a) devices with photonic crystal cavities and (b) devices without photonic crystal cavities 19

2.13 Calculated Activation Energy plots based on measured IV curves under various operation temperatures 20

2.14 Measured spectral responses (a) with and (b) without photonic crystal cavities; (c) enhanced spectral response with the incorporation of photonic crystal cavities 21

3.1 (a) Schematic of patterned silicon nanomembrane photonic crystal slab (PCS) structures (square lattice); (b) Symmetric/Asymmetric photonic crystal slab (PCS) under simulation; (c) Simulation configurations with perfectly matched layers (PML) and periodic boundary condition (PBC) 23

3.2 Simulated Reflection/Transmission Results with normal incident light for (a) symmetric photonic crystal slab and (b) asymmetric photonic crystal slab 24

3.3 The scanning electron micrographs (SEM) of the fabricated PC patterns with square lattice air hole structure for (a) SOI1115D and (b) SOI1115F 25

3.4 The scanning electron micrographs (SEM) of the fabricated large-area PC patterns with the size up to 5 mm under different zoom magnifications 26

3.5 Wet Transfer Process (From Top to Bottom): 1. Fano PC Formation on SOI (E-beam litho + Dry Etching); 2. Patterned Si NM Release (BHF Etching of BOX Layer); 3. Patterned Si NM Transfer (Glass or flexible PET) with a SU8 pre-coating. 27

3.6 (a) Microscope images of a 1 mm high “Si” through glass and SiNM; (b) Measured Transmissions of glass, SU8 coated glass and unpatterned SiNM on SU8 coated glass 28

3.7 Diffraction pattern obtained with (a) a green laser source with the green arrow showing the incident laser beam direction) passing through the SiNM on glass (shown as the dashed square), and (b) with a broadband QTH lamp source 28

3.8 Schematic of Measurement setup for Transmission based on TRIAX 320 spectrum meter and a broadband QTH light source is used 29

3.9 Measured and simulated transmission characteristics of Fano Filters for (a) a SiNM-on-glass sample; and (b) a SiNM-on-PET sample. Good agreement is seen on the spectral dip location at 1.551 μm and 1.562 μm, for (a) and (b), respectively. Note r, a, t and λ are the PC air hole radius, PC lattice constant, slab thickness and wavelength, respectively 30

3.10. Top view (top) and cross-sectional view (bottom) of simulated field profiles for (a) the resonant mode and (b) non-resonance mode 31

3.11 Angle and Polarization Dependence (θ: angle off surface normal; Φ: angle off ΓX direction; ψ: angle of polarization). 33

3.12 Measured surface-normal polarizer-dependent transmission with different angles Φ for (a) without polarizer, and (b) with polarizer fixed at *ψ*=0º 34

3.13 Measured polarizer-dependent transmission with different incident angles θ for (a) without polarizer,Φ = 0º and (b) with polarizer fixed at ψ = 0º 35

3.14 Measured polarizer-dependent transmission with different incident angles θ for (a) without polarizer, Φ = 22.5º and (b) with polarizer fixed at ψ = 22.5º 36

3.15 Measured angle-dependent transmissions with different incident angles θ with Φ = 45^0 and ψ = 45^0 (a) transmission plot; (b) complete transmission intensity map 37

3.16 Measured angle-dependent transmissions with different incident angles θ for (a) Φ = 0^0 and ψ = 0^0, and (b) Φ = 45^0 and ψ = 45^0. Note measured transmission peaks/dips (circles) agree well with the simulated dispersion curves for different incident angles 38

4.1 (a) Schematic of patterned silicon membrane reflector structure with square lattice; (b) Simulation configurations with perfectly matched layers (PML) and periodic boundary condition (PBC), the plane wave source is used 41

4.2 Simulated reflection/transmission results of membrane reflector (a=0.9 μm, r/a=0.26, t=0.34 μm) with normal incident light for (i) air-slab-air, (ii) air-slab-oxide and (iii) oxide-slab-oxide 42

4.3 (a) Schematic of a Membrane reflector with vertical air-Si-oxide (“ASO”) confinement configuration; (b) A cross-sectional SEM image of a membrane reflector on SOI, with key parameters labeled; (c) An angled, top-view SEM image of the Membrane reflector, with a close-up view shown in the inset. 43

4.4 Schematic of Fiber based Measurement setup for Reflection with Optical Spectrum Analyzer (OSA) and a broadband fiber output light source is used 44

4.4 (a) Measured and simulated reflection spectra for a Membrane reflector with a = 980 nm, r/a = 0.28, t_{Si} = 365 nm and tox =1 μm. (b) The simulated electrical field plots are also shown for both reflection band (top) and transmission band (bottom) 45

4.5 (a) Schematic and (b) cross-sectional SEM images of spectral trimming processes with controlled BHF etching time (60 sec., 2 min., 7 min.) of BOX layer for blue-shift and controlled oxide deposition for red-shift 47

4.6 Measured reflection characteristics: (a) Reflection spectra for Membrane reflectors with different BHF etching time (from 0 to 8 min). The reflection spectra are shifted up by multiples of 100's for different etching times to provide a better view of the spectra. (b) 99% reflection spectra bands for different BHF etching times. Shown in the insets are the SEM images for Fano filters with ASO (0min BHF etching time) and ASA (10 min BHF etching time) configurations 48

4.7 (a) Measured reflection spectra for different SiO_2 thicknesses deposited on top of the Si device layer (from 0 to 298 nm); and (b) 99% reflection spectral widths for different PECVD oxide thicknesses. 49

4.8 Measured reflection spectra for Membrane reflectors with three configurations: ASO (air-slab-oxide) as fabricated, ASA (air-slab -air) realized with a 4 min BHF etching from the ASO structure and OSO (oxide-slab-oxide) with SOG backfill of the ASA structure 51

5.1 Schematic diagram of a Vertical Cavity Surface Emitting Laser (VCSEL). 53

5.2 Schematic diagram of a Membrane Reflector Vertical Cavity Surface Emitting Laser (MR-VCSEL). 54

5.3 (a) Schematic of patterned silicon Membrane Reflector VCSEL structure with square lattice; (b) Simulation configurations with perfectly matched layers (PML) and periodic boundary condition (PBC), the plane wave source and planar monitor are used 55

5.4 (a) Simulated reflection properties of Top MR (r=0.25a, t=0.34 μm) and Bottom MR (r=0.45a, t=0.34 μm) with 370 nm thick SiO_2 buffer layers; (b) Simulated MR/InGaAsP QW/MR cavity mode along with the phase property 56

5.5 Simulated MR/InGaAsP QW/MR cavity modes along with the phase property with 370 nm thick SiO_2 buffer layers 57

5.6 Photoluminescence (PL) Measurement of InGaAsP QW structure over temperature (From 9 K to 310 K) 59

5.7 Plots of Photoluminescence (PL) Peak Location (left) and Linewidth (right) over Temperature (From 9 K to 310 K) of InGaAsP QW 60

5.8 Microscopy Images of Fabricated InGaAsP QW device; (a) a block area top view and (b) zoom in of two particular devices. Note the aperture size from 20 µm to 100µm 61

5.9 Scanning Electron Microscope (SEM) images in top view of Top/Bottom Membrane reflectors on SOI, with key parameters labeled 62

5.10 A Scanning Electron Microscope (SEM) image in top view of bottom Membrane Reflector on SOI with 365 nm SiO_2 on top and Measured Reflection via OSA 63

5.11 A digital single-lens reflex (DSLR) camera image in top view of top membrane reflectors transferred onto a glass slid and Measured Reflection via OSA 64

5.12 A digital single-lens reflex (DSLR) camera image of transferred InGaAsP/Bottom MR (a) Top view and (b) Angled view under a beam light (the red square shows the bottom MR area seen through the QW) 65

5.13 Schematic and DSLR images of integrated MR-VCSEL 66

5.14 Schematic of photoluminescence (PL) Measurement setup for integrated MR-VCSEL. TRIAX320 spectrum meter and a 300mW green laser (533nm) light source are used 67

5.15 Photoluminescence (PL) Measurement of integrated MR-VCSEL over temperature (From 268 K to 290 K). 67

5.16 (a) Photoluminescence (PL) Measurement of integrated MR-VCSEL over temperature (From 268 K to 290 K); (b) Plots of Photoluminescence (PL) Peak Location (left) and Linewidth (right) over Temperature (From 268 K to 290 K) of integrated MR-VCSEL. Calculated cavity resonance λ is also plotted 68

5.17 Measured Photoluminescence (PL) Peak values (at λ=1545nm) by setting the polarizer angle ψ from 0° to 360° at room temperature. The top figure shows the PL plots of start and end points 69

5.18 Measured Current-Voltage (I-V), insert is the InGaAsP QW LED array on PET under test. 70

5.19 OSA based L-I setup with kiethley pulsed current source and lensed fiber 72

5.20 (a) Light-current characteristics of InGaAsP QW LED array device at 293 K; (b) Measured spectral outputs for injection current of 45 mA and 60 mA 72

5.21 Near-field images for the InGaAsP QW LED array for different biasing levels 73

6.1 (a) Schematic of Si Membrane Modulator embedded in ITO coated PET plastics and (b) Flexible Membrane Modulator 77

6.2 (a) Schematic of electrically pumped MR-VCSEL transferred on glass and (b) Flexible MR-VCSEL 78

LIST OF TABLES

Table Page

5.1 Design Parameters of InGaAsP Quantum Well QW Cavity on InP Substrate......................... 58

5.2 Selective Wet Etching of InGaAsP QW top Mesa.. 61

CHAPTER 1

INTRODUCTION

1.1 Photonic Crystals

Photonic crystals (PCs, or PhCs), semiconductors for light, are engineered material structures with periodic modulation in refractive index (one kind of photonic metamaterials) [1, 2] It holds great promises for revolutionizing the photonics industry, owing to the ability of photon density manipulation and alternation of light-matter interaction. It offers a disruptive platform for nanophotonics, where ultra-compact, high performance light sources, modulators, detectors, sensors, solar cells, as well as waveguides, photon processing, and other left hand and meta-material based novel physical phenomena can all be realized, potentially on the same chip monolithically integrated. Significant progresses have been made on PC devices [3-6].

1.1.1 Periodic Structures

Depending on the degree of the index modulation, there are three kinds of periodic structures, namely, one-, two-, and three-dimensional, as showed in figure 1.1.

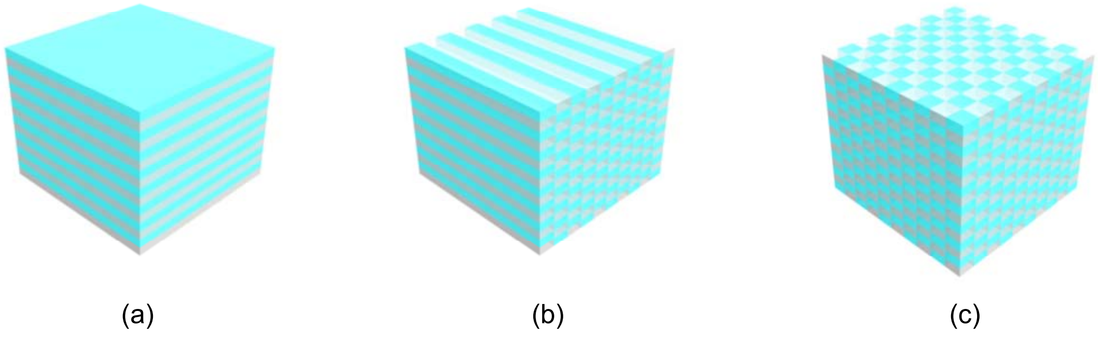

(a) (b) (c)

Figure 1.1 Schematic of photonic crystal structures: (a) one dimensional-PC (1D), (b) two dimensional-PC (2D), and (b) three dimensional-PC (3D).

For practical device applications, one of the most widely studied structures is the planar two-dimensional photonic crystal slabs (2D-PCSs), due to easy fabrication and device integration. Shown in figure 1.2 is a 2D-PCS with periodic square lattice air holes in a finite-height semiconductor substrate (e.g. Si). In this dissertation, all our work will be based on 2D PCS structures.

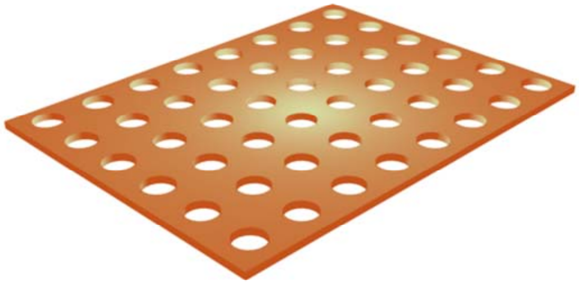

Figure 1.2 Schematic of 2D photonic crystal slab (PCS) with square lattice air hole structure.

1.1.2 Photonic Bandgap

Photonic bandgap (PBG) can be accurately predicted with computational methods, based on Maxwell’s equation. By using plane wave expansion (PWE) method, which is a common computational technique in electromagnetics to solve the Maxwell's equations by formulating an eigenvalue problem out of the equation. We can solve the band structure or dispersion relation in a given PC structure. Two calculated bandgap structures are shown in figure 1.3. The position, size and the polarization properties of the PBG depends on the refractive indexes of the materials, the dimensionality of the periodicity, the crystalline structure, and the occupation ratio between two constituted materials the configuration and the dimensions.

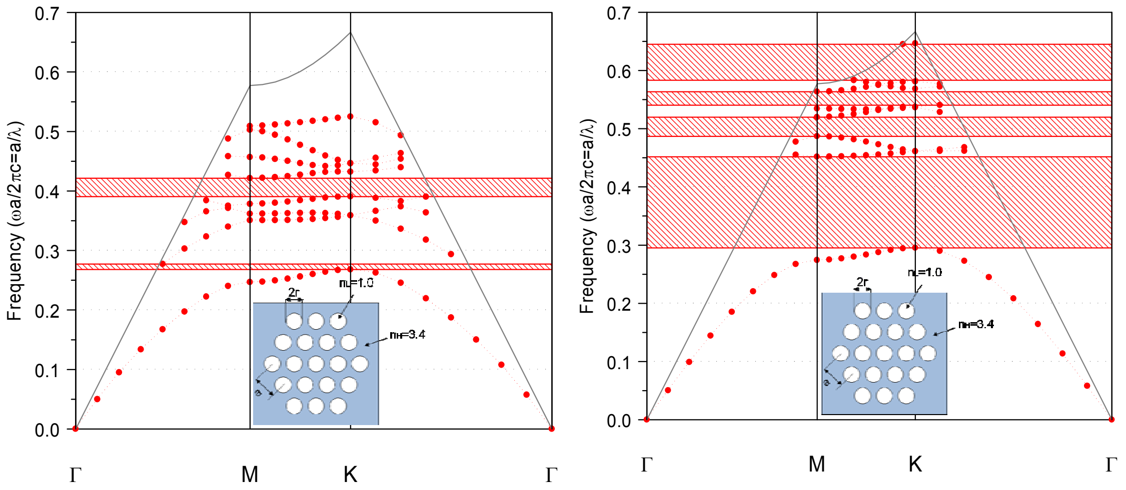

(a)

(b)

Figure 1.3 Calculated photonic crystal bandgap structures with different parameters. (a) a=0.96μm, r/a=0.4, t=1.34μm, n_{high}=3.4, n_{low}=1.0; and (b) a=1.94μm, r/a=0.4, t=1.34μm, n_{high}=3.4, n_{low}=1.0.

1.2 Photonic Crystals for Spectrally-Selective Infrared Photodetectors

The existence of photonic band gaps (PBGs) and unconventional dispersion and refractive properties makes possible hitherto not realizable spectrally-selective optical devices such as ultra-compact routers, highly wavelength selective and compact add/drop filters [5, 6]. Owing to the ability of spontaneous emission control [7, 8], PCS [9] waveguide cavities have been a subject of active research for ultra-compact high efficiency light sources [10, 11], with potentially zero threshold [12-15]. Additionally, PC structures can lead to other physical phenomena, e.g., optical absorption property alteration, through the photonic density of states (DOS) engineering [16]. Enhancement and suppression of thermal emission and absorption reported so far are mostly based on bandedge effect in various metallic PC structures or clusters. Enhanced absorption can happen near or at the band edge where the electromagnetic Bloch wave is still extended throughout the structure, its group velocity is near zero, and the photonic DOS is greatly increased. In this regime, enhanced light-matter interaction is expected and enhanced laser gain, light absorption and nonlinear effects have all been proposed [1, 2, 16-21]. Enhanced absorption in tungsten 3D PCs has been reported [22]. Both theoretical and experimental research has been carried out and confirmed the modification of the Planck blackbody radiation[23]. Most of the work so far has been focused on the absorption change in one-dimensional distributed Bragg reflector (1D DBR) based cavities [18, 24], or one-, two- and three-dimensional (1D, 2D, 3D) metallic photonic crystal cavities [2, 16, 19]. Little work has been reported on the modified absorption characteristics in 2D dielectric photonic crystal slab (PCS) cavities [20], to the best of our knowledge.

Simultaneous inhibition and redistribution of spontaneous emission in PC has been demonstrated theoretically and experimentally in a lossless dielectric PCS structure [8]. The introduction of an absorption layer in a dielectric PCS structure (e.g. quantum well, quantum dots) can lead to the modification of the absorption characteristics, due to the spectrally-selective light-matter interaction in the cavity. We propose a photonic crystal infrared photodetector (PCIP) configuration, where the photonic crystal defect cavity was integrated with the quantum dot infrared photodetectors (QDIPs) [20, 25] for higher operation temperature and spectrally selective absorption, highly desirable for infrared gas sensing and hyper-spectral imaging. High spectral selectivity with tunable wavelength coverage and spectral width can be feasible based on defect engineering and simple lithographic control, and/or external control [26].

Theoretical investigation has been carried out on the spectrally selective absorption properties in one- and two-dimensional (1D, 2D) PC structures with and without defect. The work is based on transfer-matrix method (TMM) [27] and three-dimensional (3D) finite-difference time-domain (FDTD) [28] technique. For defect-free 1D PC structures, enhanced absorption was observed at either lower or higher frequency bandedges, depending on the relative refractive index of absorptive layers. Wavelength selectivity as high as 40 was observed. For 2D symmetric air hole triangular lattice PC structures [29], [30], enhanced absorption at defect level was obtained, with the enhancement factor largely dependent upon the spectral overlap between the absorption material and the defect mode cavity. Complete absorption suppression within photonic bandgap region was observed in defect-free cavities and in single defect cavities when the absorption spectral band has no overlap with the photonic bandgap.

Recently, great attention has been paid to guided resonances, a class of “leaky” modes in PCS. These guided resonances are standing electromagnetic waves that are guided with the electric field distribution confined within PCSs, but are also strongly coupled to out-of-the-plane radiation modes due to phase matching provided by the periodic lattice structure. Therefore, guided resonances can provide an efficient way to channel light from within the slab to the external environment, and vice versa. The interaction between the discrete guided resonances and the continuum incident radiation manifests itself in the form of very sharp peaks in the transmission spectrum, called Fano resonances [3, 31], or guided mode resonance (GMR) in 1D grating structures [32, 33]. Unlike PCS structures with a complete photonic bandgap, the effects of guided resonance phenomena do not require exceptionally high index contrast. The substrate index requirement is also substantially relaxed [34]. This Fano resonance effect has been investigated, both theoretically and experimentally, in photonic crystal structures for filters [35-39], modulators[40, 41], sensors [42, 43], thermal-radiation spectral and spatial control [44], broadband reflectors[45, 46], surface emitting lasers [47], bistable and other nonlinear optical devices [48, 49].

We will also report spectrally selective IR absorption enhancement in the *defect-free* photonic crystal cavities, via Fano resonances. The spectral location of Fano resonances can be controlled with several design parameters, such as the ratio of the air hole radius to the lattice constant (r/a), the refractive index and slab thickness, and the absorption layer properties. For a symmetric slab structure (air-slab-air) with an absorptive layer in the center of the slab, enhanced absorption can be observed with enhancement factor ~180 for certain range of r/a values, where a typical absorption coefficient of 10^4 cm^{-1} at wavelength of 4 μm was used.

The impact of design parameters have been investigated in terms of the spectral tunability and absorption enhancement factor. Most importantly, we achieved similar results for an asymmetric slab structure (air-slab-substrate), with enhancement factor ~60 to 170, depending on the r/a value and the substrate index. This important feature ensures flexible design for infrared photodetectors incorporating photonic crystal cavities.

1.3 Photonic Crystals for Spectrally-Selective Light Sources

Since the first proposal of spontaneous emission control with photonic crystals [7], a large variety of light emitting devices have been demonstrated, mostly with planar 2D air hole lattice structures. These structures are incorporated in LEDs for improved extraction efficiency and directionality, in edge emitting lasers as cleave free end mirrors and/or PBG line defect defined waveguide, in DBR based VCSELs for mode control, and in photonic band edge surface emitting lasers (PBELs) as 2D DFB lasers. Most of these applications utilize the photonic bandgap purely as mirrors or filters, where there is little impact on spontaneous emission rate. On the other hand, spontaneous emission control is enabled in photonic bandgap defect mode lasers (PBDLs) by embedding the active region *inside* the photonic crystals, where 2D air columns are etched through the cavity, including active regions.

Currently, all VCSELs are Distribution Bragg Reflector (DBR)-based. Despite the wide applications of VCSEL technology, current DBR-based VCSELs still have the following critical limitations/challenges that need to be removed/overcome: (a) Low integration density due to their relatively thick device structures directly resulting from the use of multi-layer DBRs (~5-20 μm thick) and their thermal management challenges; (b) Challenges in realizing long-wavelength VCSELs due to the small index contrast for lattice matched materials to InP leading to difficulties in DBR formation; (c) Complicated design/manufacturing schemes required for realizing multi-wavelength VCSEL arrays, such as patterned growth, deformable mirrors, and complicated process control, etc.

Semiconductor nanomembranes (NMs) that were recently demonstrated by Dr. Ma *et. al.* [1, 2] to be transferable, stackable and manufacturable, offer unprecedented opportunities for novel device applications, including novel VCSEL structures. It is envisioned that, based on the stackable semiconductor NM processes, high-density 3D photonic/electronic system integration on Si, including monolithically integrated laser sources, can all be realized.

We have investigated a photonic crystal membrane reflector (PC MR) based DBR-free VCSEL (MR-VCSEL) structure here. The vertical cavity of the VCSEL is formed with two stacked single-layer Fano reflectors made of patterned Si NMs. These two reflectors replace the two thick DBR mirrors commonly used in conventional VCSELs, resulting in the ultra compactness of the overall device size. The MR-VCSEL also exhibits easy tunability, which stems from the patterning of the Fano reflectors. With intra-cavity metal contacts between the mirrors and the active region, electrical injection is enabled. The entire fabrication process of the VCSEL structure will be accomplished with our demonstrated NM transfer and bonding techniques [4, 50].

The high quality active region of the laser cavity, which consists of undoped strain-compensated InGaAsP quantum well (QW) active region and doped p- and n-InP cladding layers, is obtained via releasing it as a membrane (not transferring a finished VCSEL) from a source InP substrate. The InGaAsP QW is designed to have a center emission wavelength of 1550 nm for this project.

In what follows, a spectrally-selective absorption enhanced quantum dot photonic crystal infrared photodetector on GaAs will be discussed in Chapter 2. Fano resonance based narrow band filters and broadband reflectors will be reported in Chapter 3 and 4, respectively, based on semiconductor Si nanomembranes on Si, glass or flexible substrate. A DBR-free VCSEL structure will be introduced and discussed in Chapter 5, followed finally by a conclusion in chapter 6.

CHAPTER 2

GAAS-BASED PHOTONIC CRYSTAL INFRARED PHOTODETECTORS

2.1 Introduction

Infrared (IR) photodetectors with wide spectral coverage (2 to 20 μm) and controllable spectral resolution are highly desirable for absorption spectroscopy gas sensing and hyper-spectral imaging applications [51]. Significant progresses have been made in quantum well and quantum dot based IR photodetectors (QWIPs, QDIPs). The incorporation of photonic crystals (PCs) [52-55] can lead to engineered spectral resolution with multi-spectral coverage in IR photodetectors. Simultaneous enhancement and suppression of absorption at different spectral locations is feasible via lithographically controlled photonic bandgap (PBG) and defect mode cavity [56-59].

We find that significantly enhanced absorption at the defect mode can be obtained at surface-normal direction in a dielectric single-defect photonic crystal slab (PCS), with an absorption enhancement factor greater than 10^2 in the defect mode, based on three-dimensional finite-difference time-domain (FDTD) technique. Complete absorption suppression within the photonic bandgap region can also be observed in defect-free photonic crystal cavities. Based on these findings, we investigate here experimentally a new type of infrared detectors, as shown in figure 2.1, by incorporating the photonic crystal (PC) cavity with the quantum dot infrared photodetector (QDIP). With the embedment of the PC structures into the QD substrate, the absorption can be dramatically enhanced at certain spectral locations. This can lead to spectrally selective IR detection and multi-wavelength IR detector arrays.

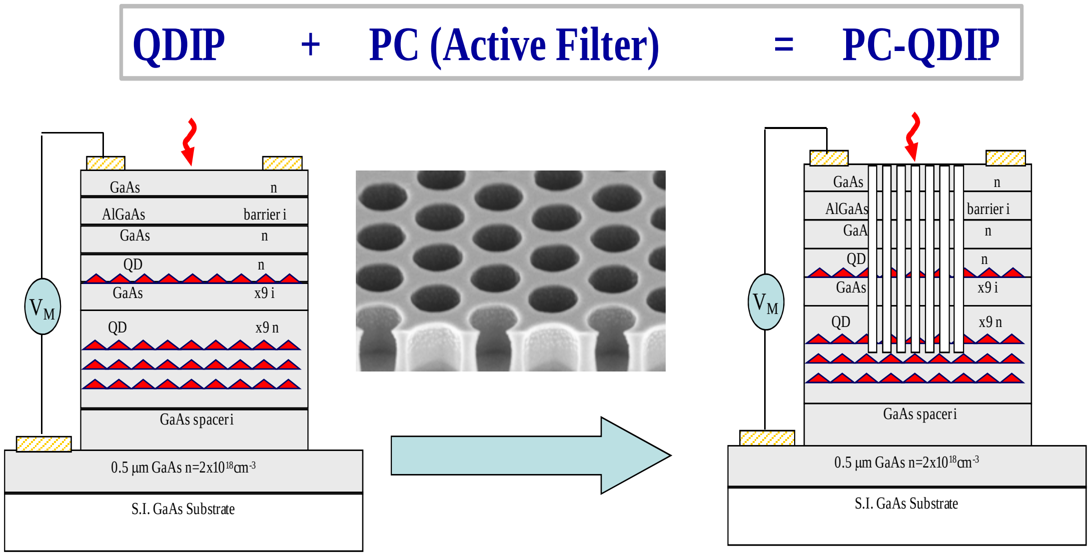

(a) (b) (c)

Figure 2.1 Schematic PC-QDIP (a) designed classic QDIP structure; (b) PC structure formed in QD substrate and (c) defined PC-QDIP structure.

2.2 InGaAs/GaAs Quantum Dot Heterstructure

The quantum dot (QD) n-i-n heterostructure (figure 2.2a) was designed at UTA, and grown at University of New Mexico and Duke University by Molecular Beam Epitaxy technology. Shown in figure 2.2b are transmission electron microscope (TEM) image and atomic force microscope (AFM) image of the epitaxial QDs. QDIP operation principle is based on the intersubband transitions inside QDs[60, 61], as shown in figure 2.3. For the DWELL (dot in a well) structure we used here, InAs dots are placed in a thin $In_{0.15}Ga_{0.85}As$ well, then both of them are embedded in 50 nm thick GaAs layers. This structure which detects IR light through intersubband transitions within the conduction band provides better confinement for the carriers trapped in the QDs by lowering the ground state of the QD relative to the GaAs bandedge. This leads to lower thermionic emission, which offers great promises for high operation temperature (HOT) QDIP with better signal to noise ratio (SNR) due to the suppressed dark current. In summary, QDIP has the following advantages:

- Wide Spectral Coverage (3 to 15+ µm)
    - Extrinsic, intersubband transitions
- Large Responsivity
    - Large optical absorption coefficient due to electron localization and long electron lifetime in excited states
- High-Operation Temperature (HOT)
    - Reduced dark current due to 3D carrier confinement
- Normal Incidence Detection
    - Polarization selection rules allow absorption of normal-incidence light

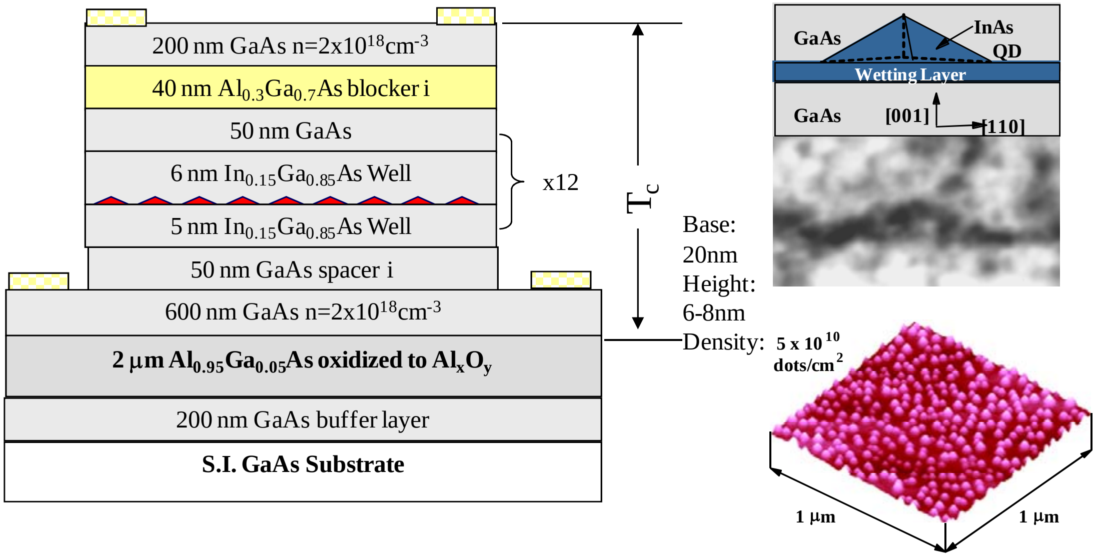

(a) (b)

Figure 2.2 InGaAs/GaAs QD Heterostructure: (a) Schematic the quantum dot (QD) n-i-n heterostructure (b) transmission electron microscope (TEM) image and atomic force microscope (AFM) image of the epitaxial QDs.

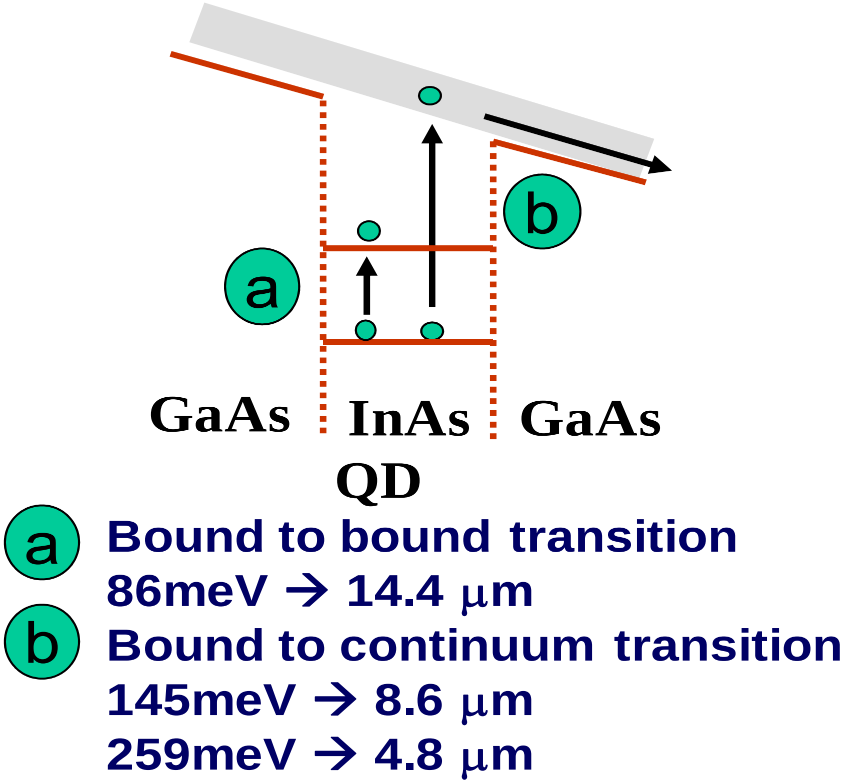

Figure 2.3 Schematic level diagrams (a) bound-to-bound state transition and (b) bound-to-continuum state transition in a biased quantum-dot infrared photodetector (QDIP).

The measured photoluminescence (PL) under room temperature is showed in figure 2.4. The PL peaks around 1040 nm, which is typical for InAs QD systems. Such emission arises from the inter-band transition between conduction and valence bands. A typical absorption spectral for a 30-stack DWELL QDIP structure is also shown in figure 2.5, with a peak absorption wavelength at 8 µm. The absorption peak location can be tuned by control the QD sizes and the QW layer thicknesses.

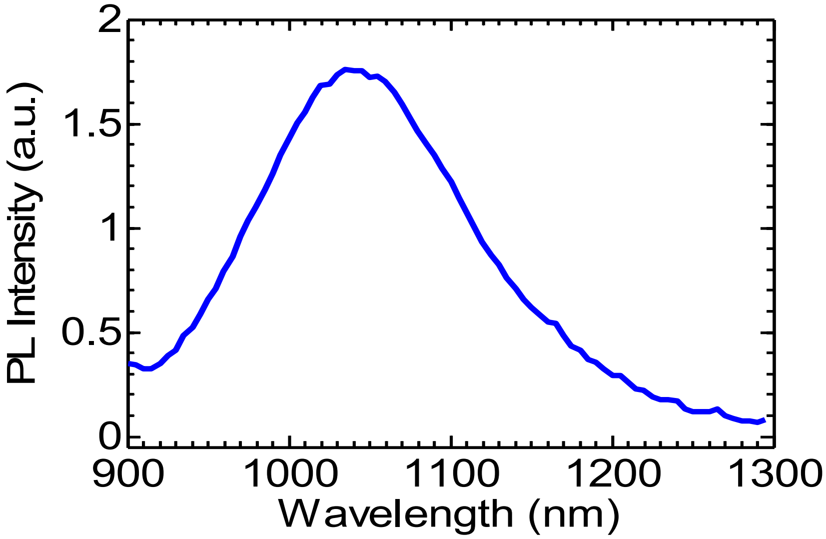

Figure 2.4 Room-temperature photoluminescence (PL) for QDs heterostructure.

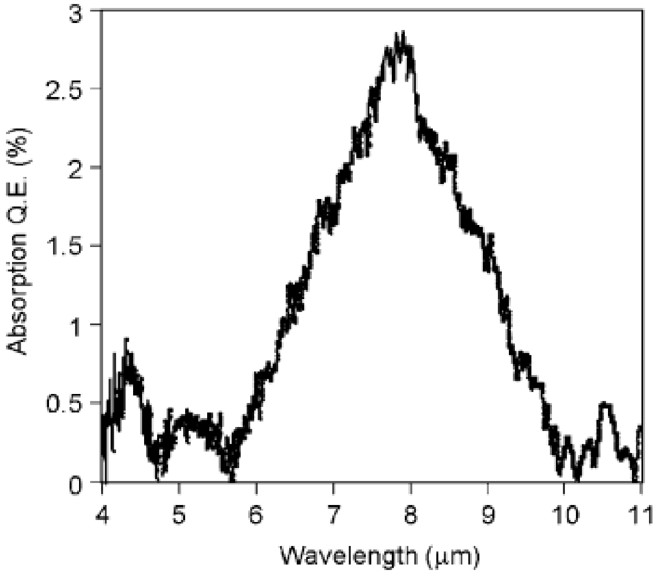

Figure 2.5 The measured internal absorption quantum efficiency (no grating or cavity effects) for a 30-stack DWELL QDIP.[62]

2.3 Photonic Crystal Cavity Designs

By applying 3D-FDTD (finite difference time domain) technique, we simulated the absorption behavior incorporation with PC cavities and designed photonic crystal structures of our PCIP devices. As showed in figure 2.6 the simulation was carried out on a symmetric slab waveguide, with a thin absorptive layer in the center of the slab, along with the PML (perfectly matched layers) and PBC (periodic boundary condition). PC cavities with and without defect were investigated. The simulated absorption results were normalized to the absorption obtained from the same slab without PC cavity (as reference).

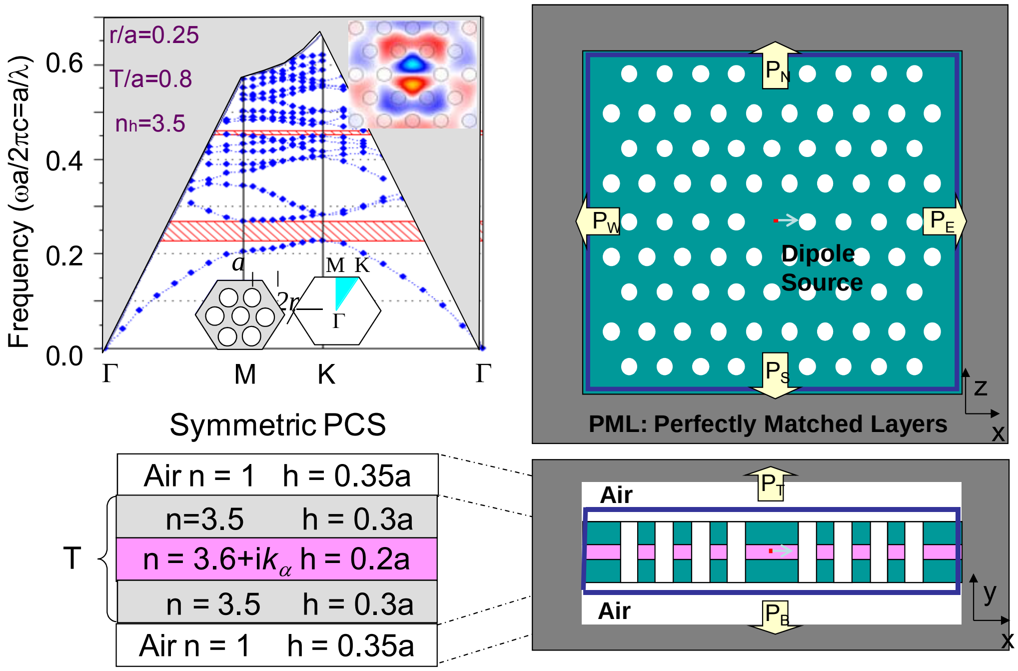

(a) (b)

Figure 2.6 (a) Photonic crystal bandgap (PCB) in the dispersion diagram (triangle lattice) and symmetric photonic crystal slab under simulation, with an absorptive layer in the center of the slab; (b) Simulation configurations with perfectly matched layers (PML).

For 2D symmetric air hole triangular lattice PC structures, enhanced absorption at defect level was obtained, with the enhancement factor (ratio of the absorption in PCS to the absorption in slab only) greater than 35 (figure 2.7). This enhancement factor is largely dependent upon the spectral overlap between the absorption material and the defect mode cavity. Complete absorption suppression within photonic bandgap region was observed in defect-free cavities and in single defect cavities when the absorption spectral band has no overlap with the photonic bandgap. In single mode cavities (single-defect), similar alternation was obtained for spontaneous emission in lossless cavities and absorption in lossy cavities.

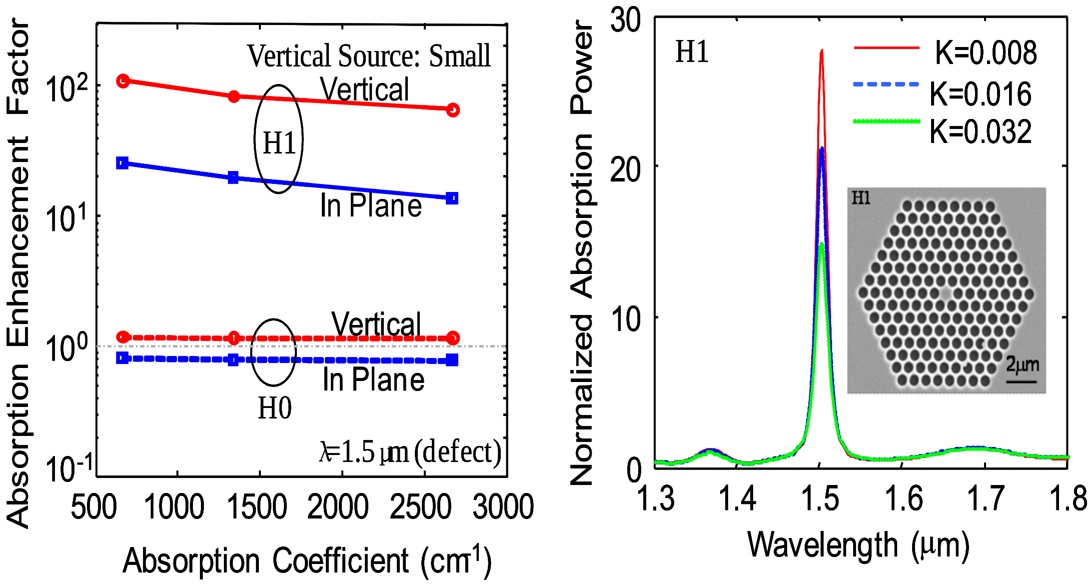

(a) (b)

Figure 2.7 (a) normalized surface normal absorption power in a single defect photonic crystal cavity for different absorption values; (b) absorption enhancement factor for different absorption values in single defect (H1) and defect free (H0) cavities. Note the dominant absorption enhancement is along vertical direction.

According to the simulation, we could get three parameters for the design: air hole's radius r, lattice constant a, and slab thickness t, as we see in the figure 2.6. Two typical designs are given for the center wavelength located at 11 µm for the QDIP materials (figure 2.8).

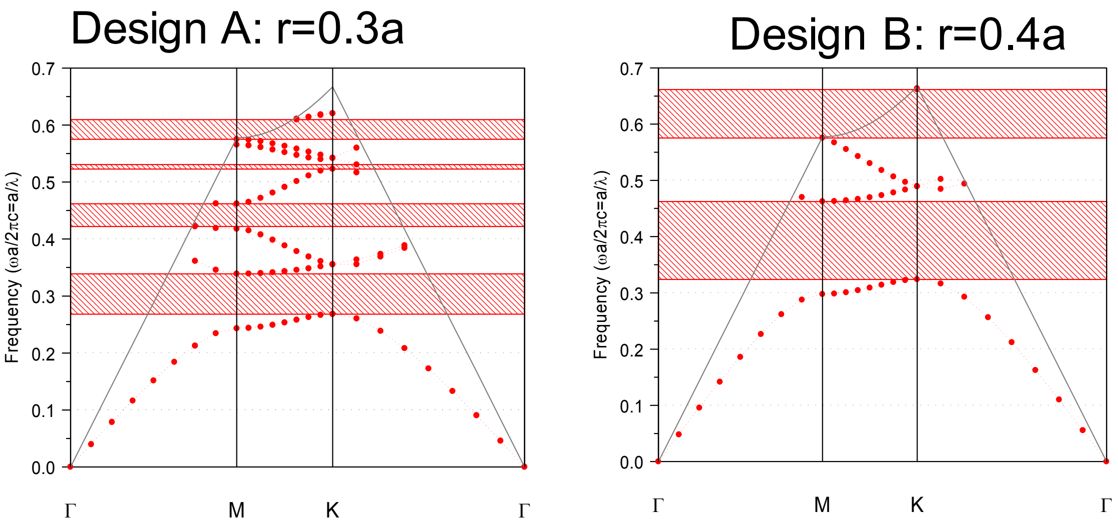

(a) (b)

Figure 2.8 Calculated Photonic Crystal Bandgap (PCB) Structure based on expension theory with: (a) a=3.33 µm; t=1.6 µm; n_{low}=1.0; n_{high}=3.4; λ_{min}=9.82 µm; λ_{max}=12.41 µm; λ_{center}=11.12 µm; and (b) a=4.19 µm; t=1.6 µm; n_{low}=1.0; n_{high}=3.4; λ_{min}=9.07 µm; λ_{max}=12.95 µm λ_{center}=11.01µm.

2.4 QD-PCIP Fabrication

The device fabrication start with E-Beam lithography to form the photonic crystal patterns into the InGaAs/GaAs QD substrate, in order to have a better etching selectivity we used SiO_2 as a hard mask. We first deposited a 160 nm thick SiO_2 on the substrate via PECVD under 200°C, then we spin-coated a ~300 nm thick E-Beam resist Zep520-A which has a very good etching selectivity to SiO_2. The E-Beam writer used is JOEL 6000 E-Beam lithography system, which has a finely focused beam of electrons, and the electrons are accelerated at 50keV with point beam, Gaussian in distribution, vector scanned over the desired area, stage stationary during the writing operation. After the development the PC patterns with E-Beam resist, the patterns were first transferred into SiO_2 layer by dry etching technique, and then the residual resist was removed by immersing the sample in acetone solution; we then used SiO_2 as mask to etch the InGaAs/GaAs substrate in Plasma RIE chamber. The scanning electron microscope (SEM) images of the E-Beam patterned QD substrate are shown in figure 2.9.

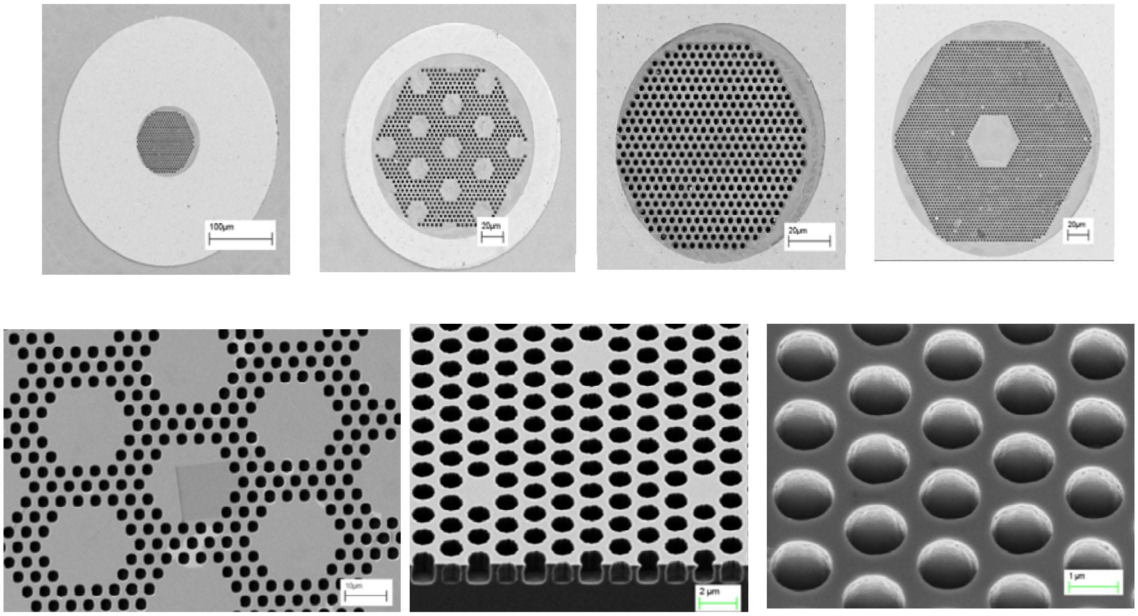

Figure 2.9 Scanning electron microscope (SEM) images of EBL pattern with various defect modes: Defect Free (H0), Single Defect (H1) and couple Defect (C3H3).

With the photonic crystal structures formed in InGaAs/GaAs substrate, the standard optical lithography process was applied as shown in figure 2.10. The n type top ring contact was first fabricated by optical lithography, descum, metallization and lift-off process, followed with mesa etching including both dry and wet etching process. Finally, we made the n type bottom contact via E-Beam evaporator. A schematic of the fabrication flow is shown in figure 2.10, together with the complete device sketch and scanning electron microscope (SEM) images.

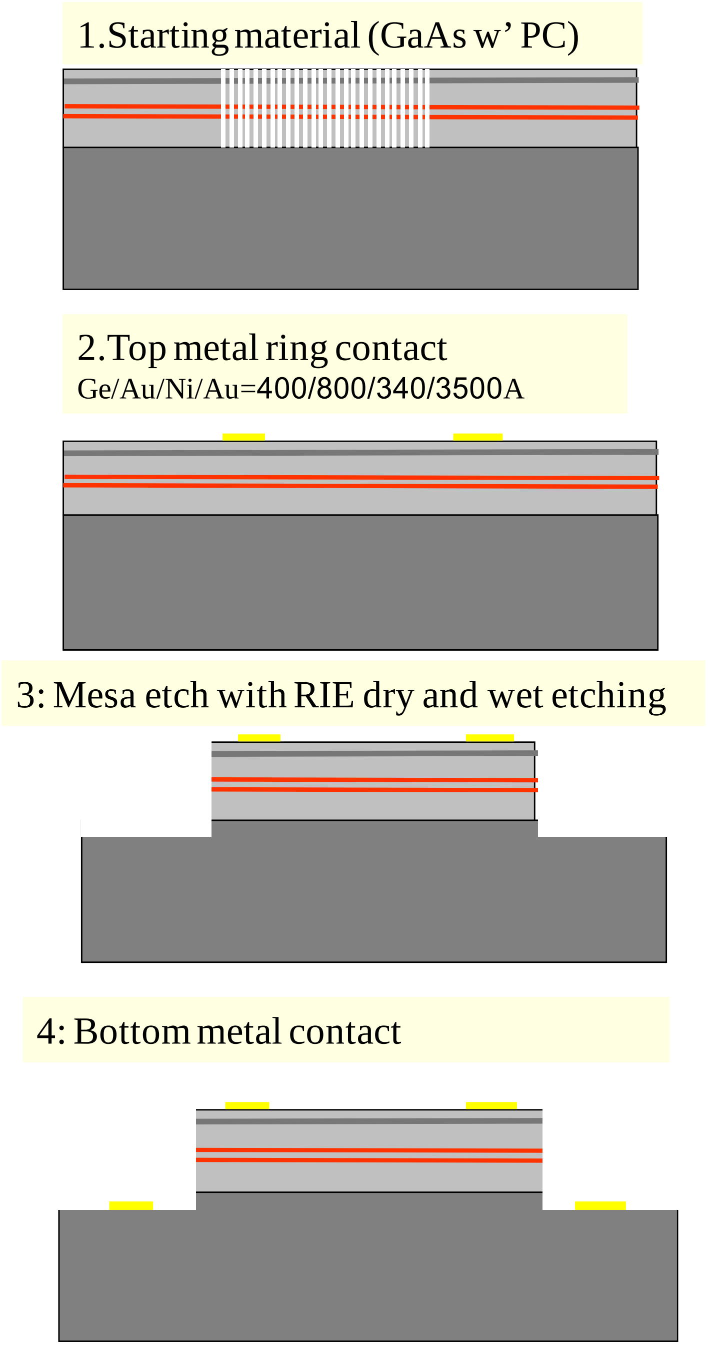

Figure 2.10 Schematic of photonic crystal (PC) cavity quantum dot infrared photodetector (QDIP): 1. Side view of QD substrate with PC pattern formed; 2. Side view of device with top n ring metal deposited; 3. Side view of device with mesa etched into bottom contact layer; 4. Side view of fabricated device with both top and bottom contact metal coated.

These SEM images of our fabricated devices indicate that various defect designs of photonic crystals were formed, the quality of etching is reasonable and the PC pattern after etching is relative smooth and straight.

2.5 Device Characteristics

The fabricated devices were finally packaged (no top lids) for precisely electrical measurements. The sub-50 μm gold ball wire-bonding was applied and the die was cut into 5 mm square (showed in figure 2.11). Dark current measurements were then done under both ambient temperature and low temperature.

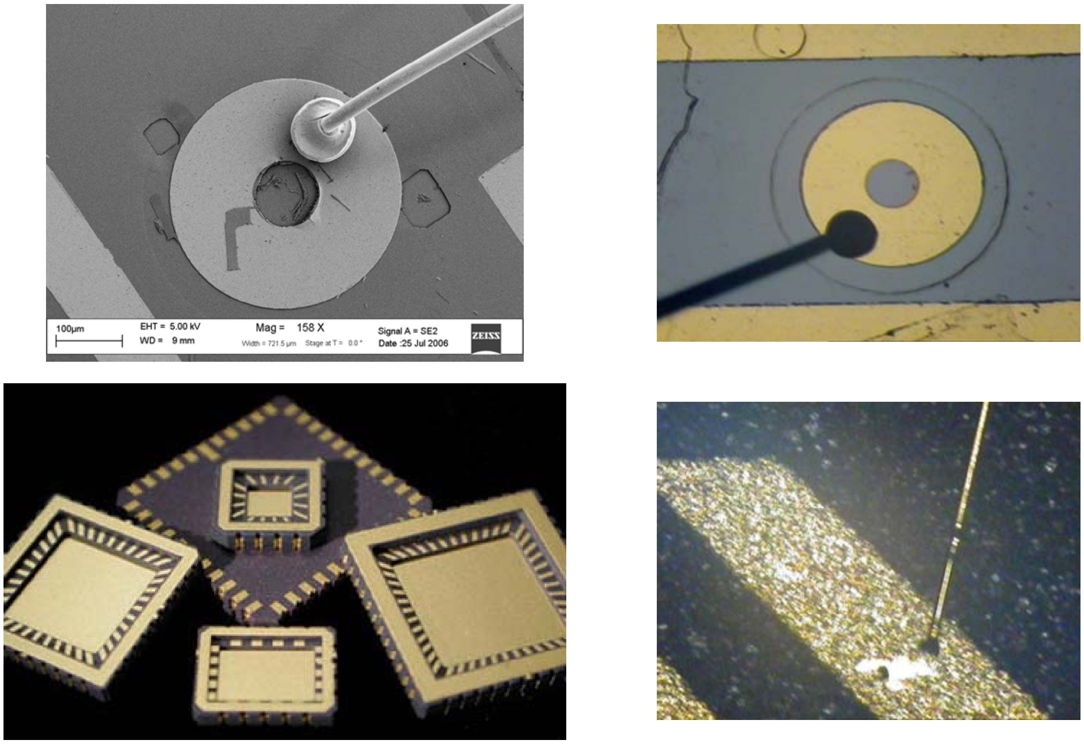

Figure 2.11 Scanning electron microscopy (SEM) and microscope top view images of fabricated device under wire bonding.

From the dark current results (in figure 2.12), with the comparison of the device with and without photonic crystals structure, we found the dark current with PC cavity has been slightly reduced. This also indicated a relatively good quality dry etching.

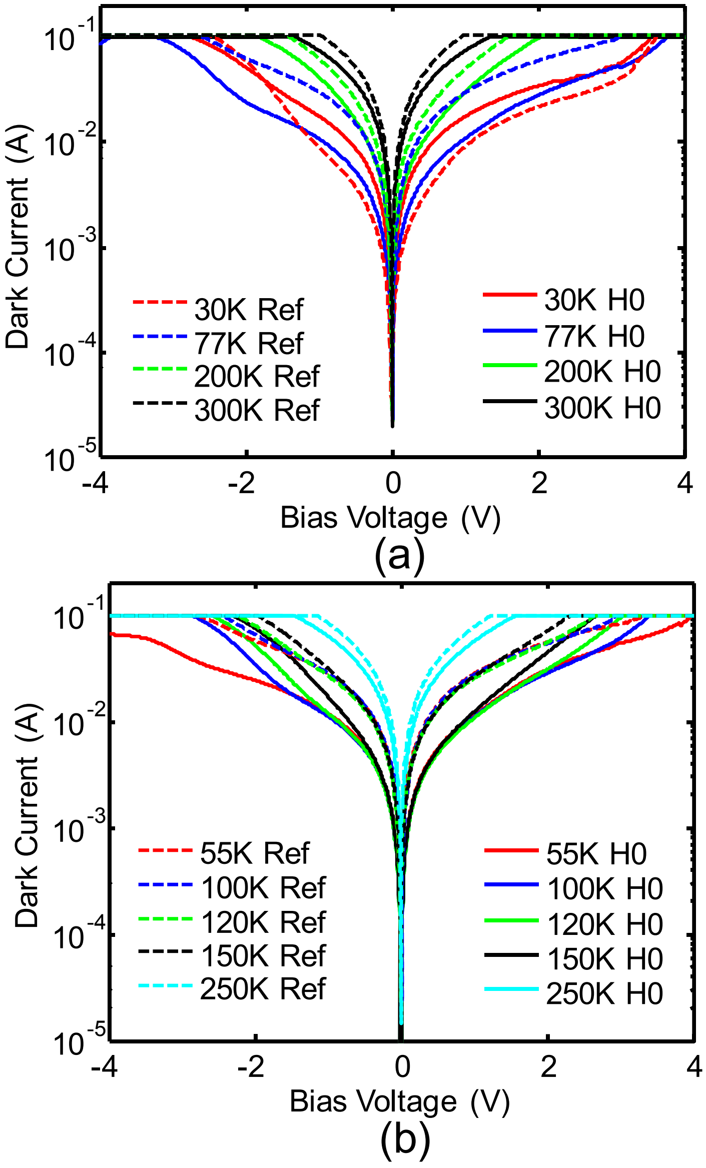

Figure 2.12 Measured current-voltage (I-V) characteristics at different temperatures (a) devices with photonic crystal cavities and (b) devices without photonic crystal cavities.

According the IV test under different temperatures, we calculated the activation energy plot (in figure 2.13), and from the result we can see the increase in the activation energy for the PC cavity, which might be due to the defect related to the dry etched surface.

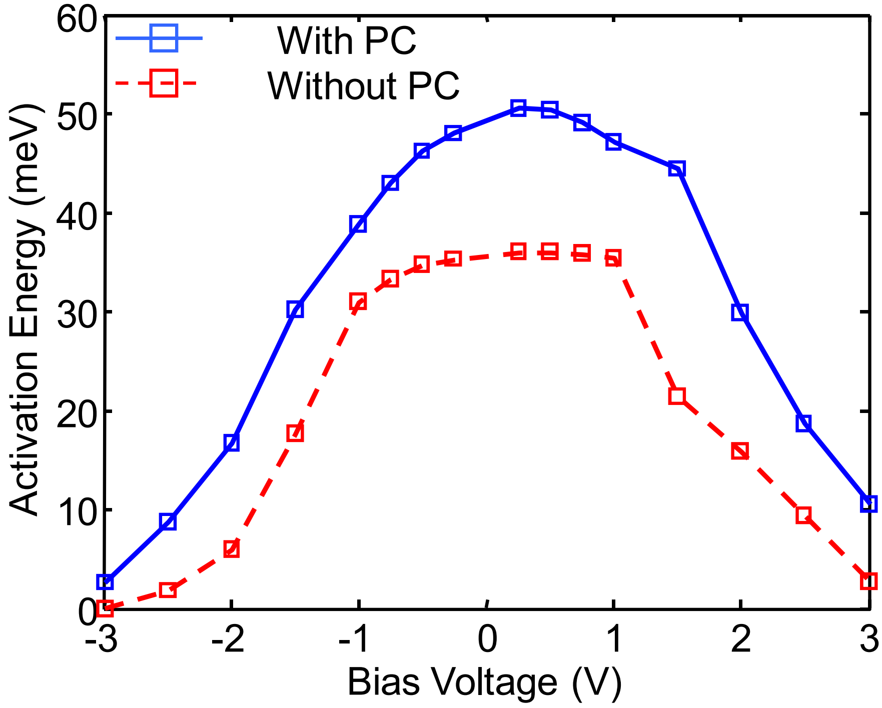

Figure 2.13 Calculated Activation Energy plots based on measured IV curves under various operation temperatures.

The spectral response measurement was also done and the measured spectral response did show an increase with the incorporation of the PC cavity (figure 2.14). For the devices without PC, we can observe the spectral response up to 55 K and with the incorporation of the PC we can observe the spectral response over 100 K.

As a conclusion, 3D FDTD technique was applied to 2D PC slab waveguide with absorptive layers: Enhanced absorption was observed in the single defect PC structures, with simultaneous absorption suppression observed in the photonic bandgap region. Dominant absorption occurs along the surface normal direction, similar the spontaneous emission process observed in photonic crystal surface-emitting lasers, where the dominant spontaneous emission occurs in the surface normal direction. The defect absorption properties remain largely the same for the coupled defect cavities, which is essential for large area infrared photodetector applications.

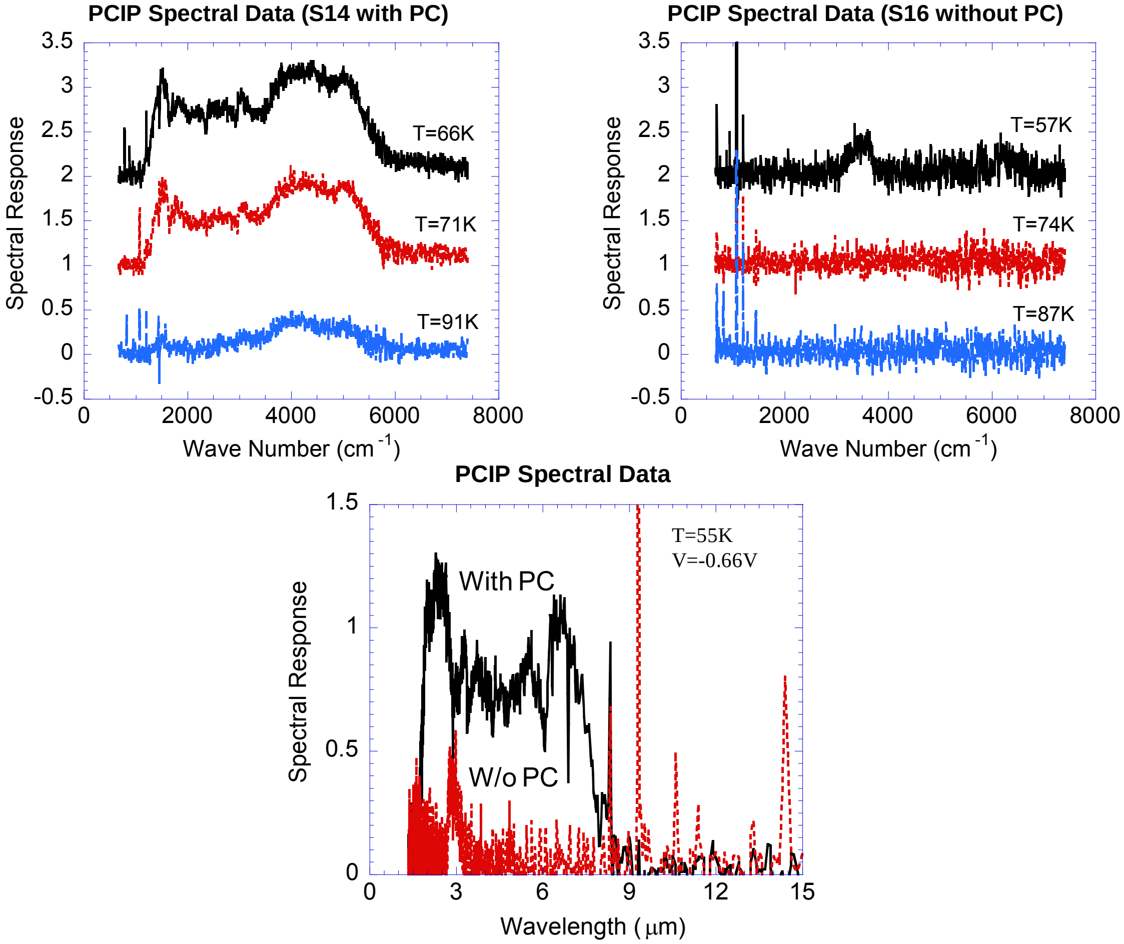
PCIP Spectral Data (S14 with PC)

PCIP Spectral Data (S16 without PC)

PCIP Spectral Data

Figure 2.14 Measured spectral responses (a) with and (b) without photonic crystal cavities; (c) enhanced spectral response with the incorporation of photonic crystal cavities.

CHAPTER 3

SI-BASED FANO-RESNANCE FILTERS

3.1 Introduction

Photonic crystal slabs (PCS), with in-plane periodic modulation of dielectric constant introduced in a high-index guiding layer, offer one of the most promising platforms for large-scale on-chip photonic integration. The out-of-the-plane optical mode coupling in the PCS is feasible with the Fano or guided mode resonance (GMR) effect [3, 31, 63], where the in-plane guided resonances above the lightline are also strongly coupled to the out-of-the-plane continuum radiation modes due to the phase matching provided by the periodic lattice structure. Therefore, the guided resonances can provide an efficient way to channel light from within the slab to the external environment, and vice versa [34, 64].

Crystalline semiconductor nanomembranes (NMs), which are transferable, stackable, bondable and manufacturable, offer unprecedented opportunities for some unique and novel electronic and photonic devices suitable for vertically stacked high-density photonic/electronic integration. High quality single crystalline silicon NMs (SiNM) have been transferred onto various foreign substrates, such as glass, polyethylene terephthalate (PET) plastics, etc. [65-68]. Record high speed electronic devices on flexible substrate were reported recently[67, 69]. Employing a slightly modified transfer process, we reported the first experimental demonstration of Fano filters[4], based on transferred single crystalline SiNMs on glass substrates, as well as on flexible PET substrates. Such a spectrally-selective filter component can be used as the building blocks for a suite of flexible and vertically stacked ultra-compact high performance photonic devices, such as switches, modulators, and spectrally-selective photodetectors.

3.2 3D-FDTD Simulations

The surface-normal Fano filter is schematically shown in figure 3.1 (a), where a patterned photonic crystal (PC) structure with square lattice air holes is formed in a SiNM that is transferred onto a glass substrate. The filter design is based on a frequency-dependent three-dimensional (3D) finite-difference time-domain (FDTD) technique. For the asymmetric air-SiNM-glass structure (figure 3.1(a)), the SiNM thickness (t) is 270 nm, and the substrate index is 1.45 - 1.48 for glass and PET substrates. The design parameters for the air hole radius (r) and the lattice constant (a) are chosen with the target filter operation wavelength (λ) of 1.55 μm.

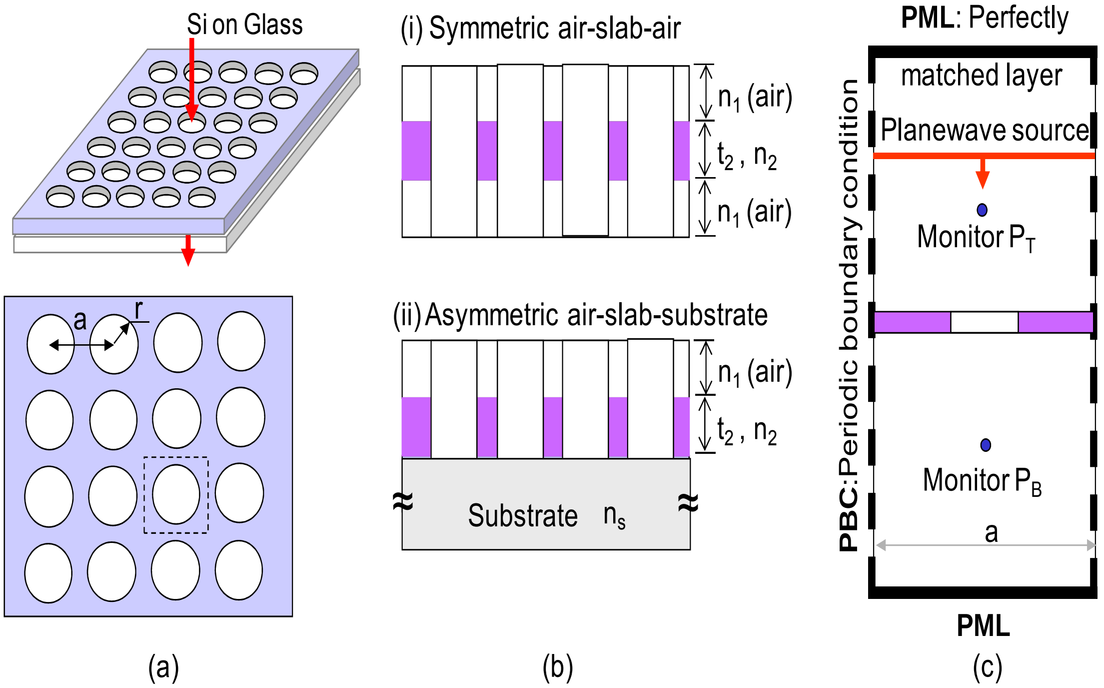

Figure 3.1 (a) Schematic of patterned silicon nanomembrane photonic crystal slab (PCS) structures (square lattice); (b) Symmetric/Asymmetric photonic crystal slab (PCS) under simulation; (c) Simulation configurations with perfectly matched layers (PML) and periodic boundary condition (PBC).

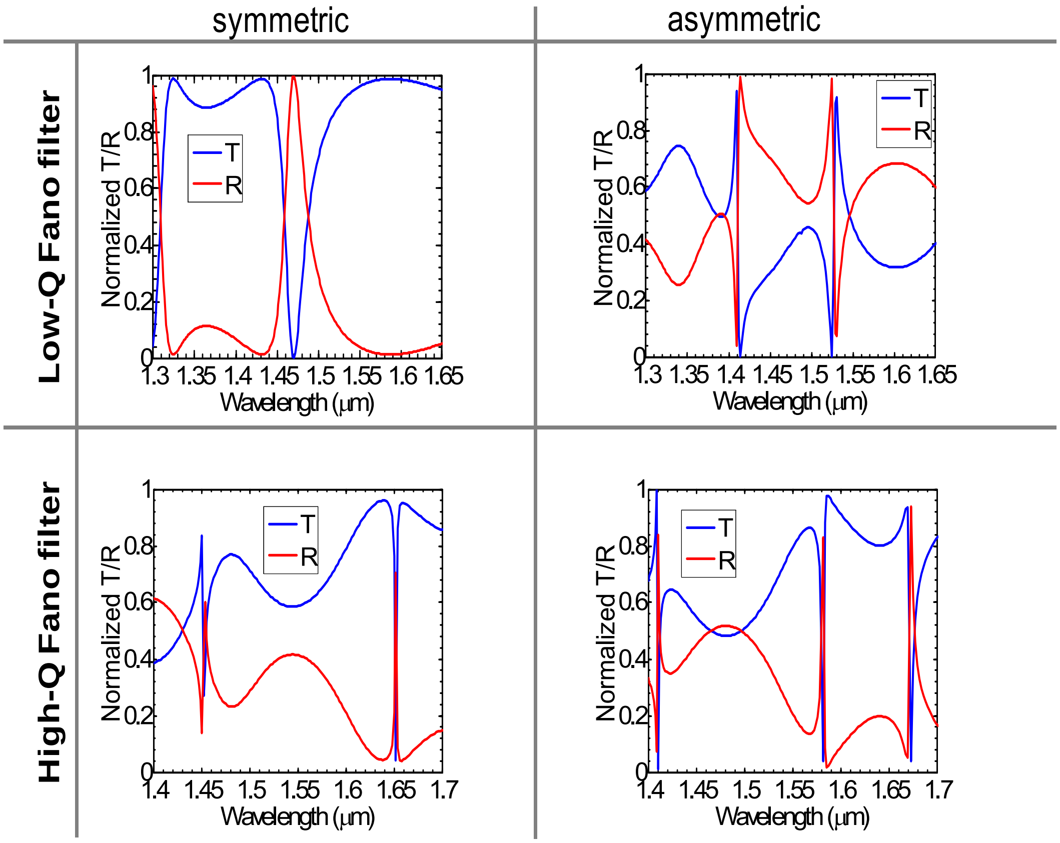

(a) (b)

Figure 3.2 Simulated Reflection/Transmission Results with normal incident light for (a) symmetric photonic crystal slab and (b) asymmetric photonic crystal slab.

3.3 EBL Fabrication

The starting material is a silicon-on-insulator (SOI) wafer with a 270 nm top Si layer, and a 3 μm-thick buried oxide (BOX) layer on the Si substrate. The PC was first fabricated on the SOI wafer using a standard ZEP520A E-Beam lithography technique and an HBr/Cl_2 chemistry based plasma reactive-ion etching (RIE) process. Shown in figure 3.3 (a) and (b) are the scanning electron micrographs (SEM) of the fabricated large area PC patterns (~5x5 mm^2), also shown in figure 3.4, where the high quality uniform patterns are formed with optimized fabrication processes. Note the large-area pattern is generated here only for the purpose of simplified testing scheme, where a focused beam can be easily aligned to the patterned PC area for a transmission test. In practice, the typical patterned PC device area shall only be about ten times the period of the lattice constant a, or 5-10 μm in lateral dimension for the device with the operation wavelength of 1.55 μm.

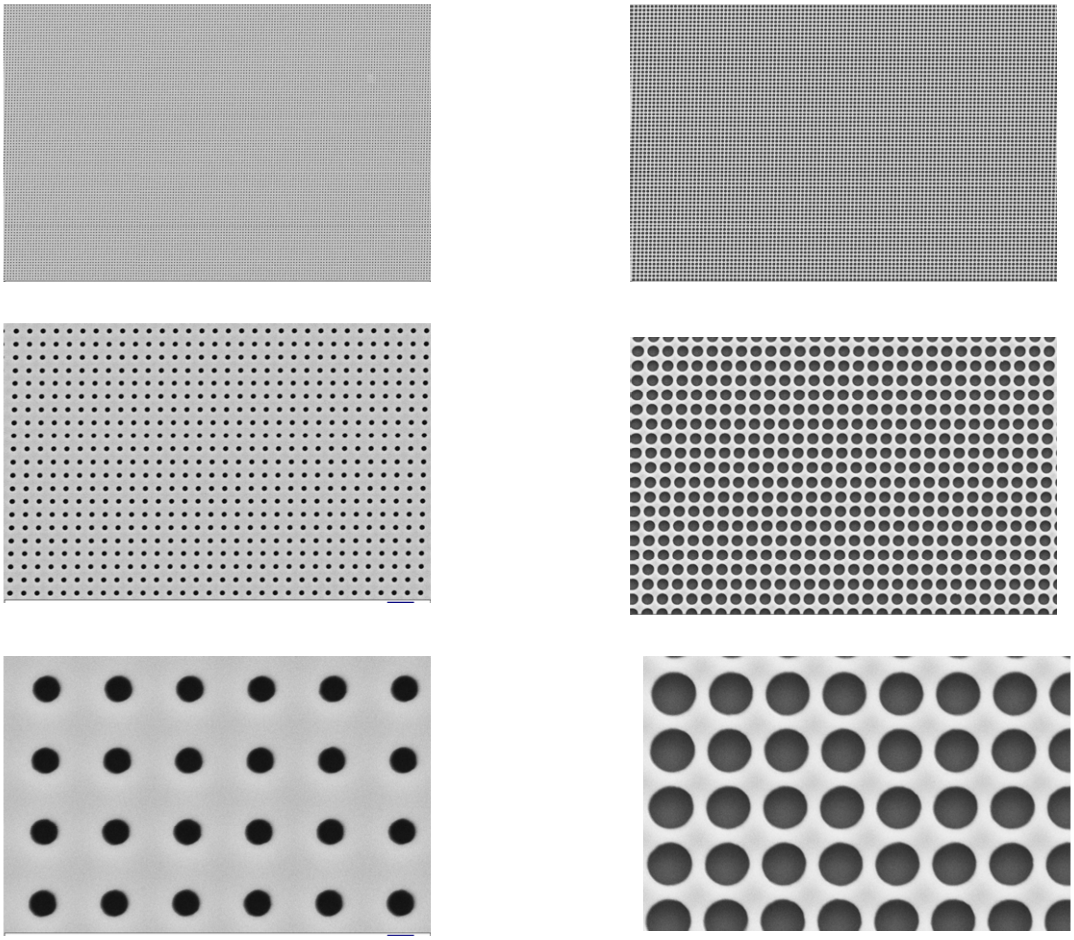

SOI1115D SOI1115F

Figure 3.3 The scanning electron micrographs (SEM) of the fabricated PC patterns with square lattice air hole structure for (a) SOI1115D and (b) SOI1115F

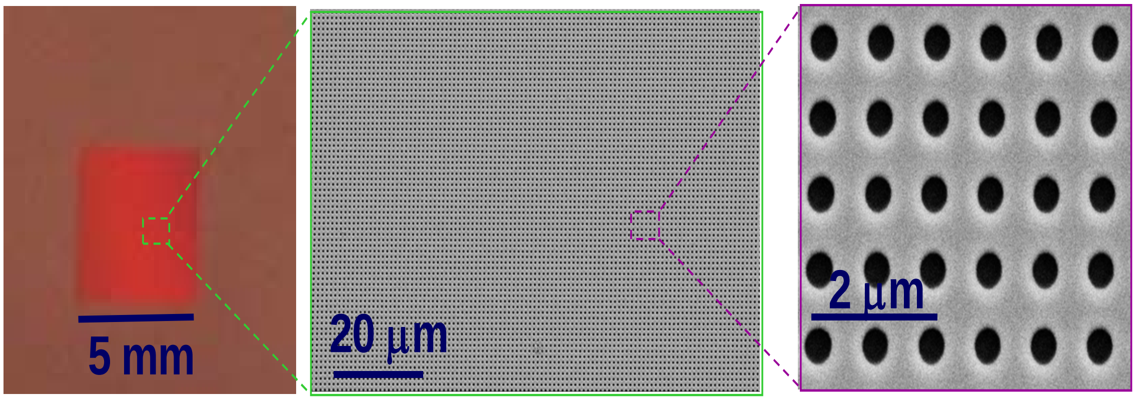

Figure 3.4 The scanning electron micrographs (SEM) of the fabricated large-area PC patterns with the size up to 5 mm under different zoom magnifications.

3.4 Membrane Transfer Technique

The patterned PC SOI structure was subsequently transferred onto a glass or a polyethylene terephthalate (PET) substrate, based on a modified wet transfer process shown in figure 3.5 [10]. The structure was immersed in aqueous diluted HF solution (49% HF: DI water =1:4) for several hours to etch away the BOX layer selectively. Once the top patterned PC SiNM was completely released, it was rinsed in DI water and transferred onto glass or PET flexible plastic substrates. It is worth noting that an optional SU8 coating on the glass may be used for improved adhesion and mechanical stability for the final device structure. The microscope images were taken for the transferred SiNM as shown in figure 3.6 (a), it shows a quasi-transparent compared to pure glass and the measured transmission results are also shown in figure 3.6 (b); The transferred high-quality SiNM PC patterns were verified with diffraction pattern measurements, as shown in figure 3.7, with a micrograph shown in the inset being the transferred PC patterned SiNM on the glass substrate under the test. A well-defined diffraction pattern was observed with a continuous-wave green laser source passing through the SiNM on the glass substrate. Also shown to the right of figure 3.7 is the highly ordered diffraction pattern obtained with a focused broadband Quartz Tungsten Halogen (QTH) light source passing though the device.

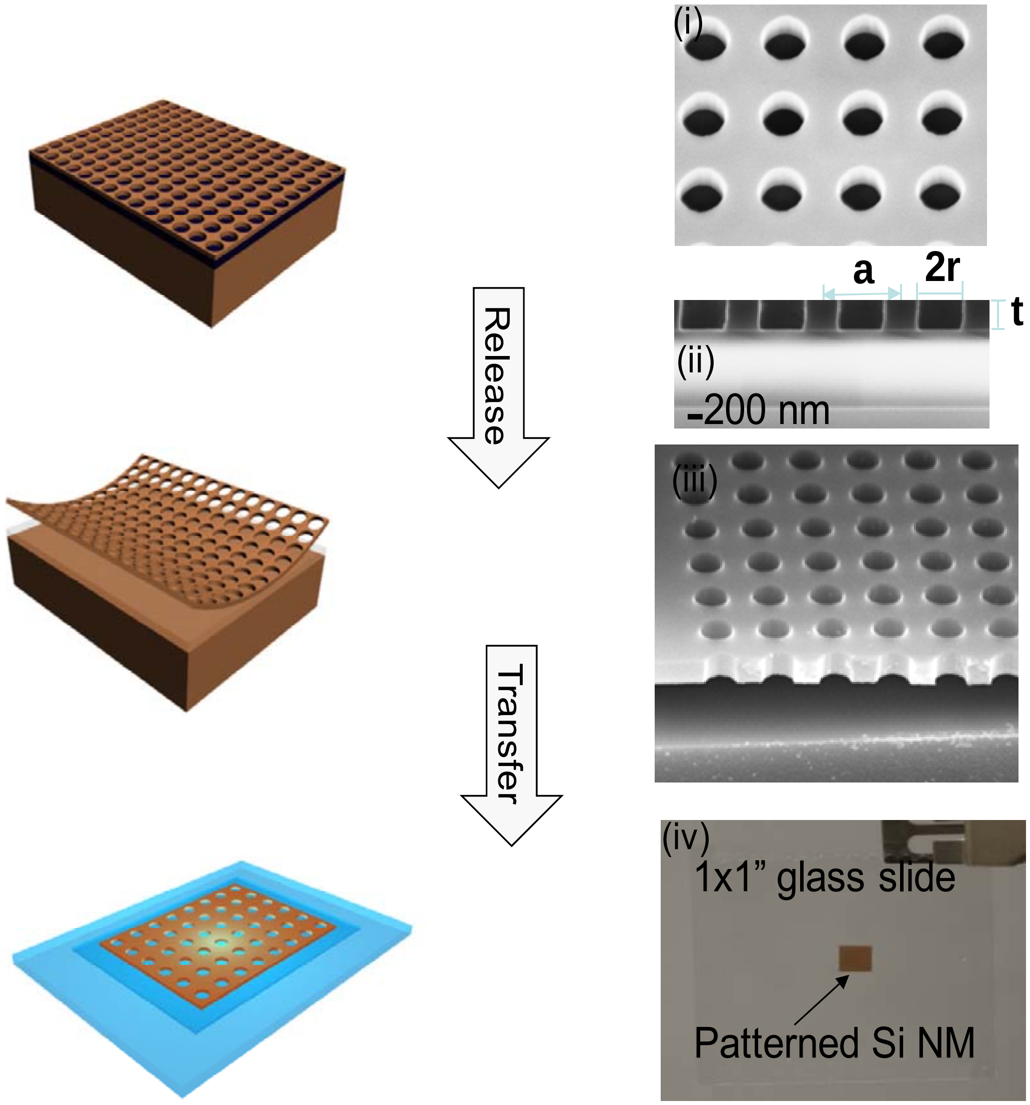

Figure 3.5 Wet Transfer Process (From Top to Bottom): 1. Fano PC Formation on SOI (E-beam litho + Dry Etching); 2. Patterned Si NM Release (BHF Etching of BOX Layer); 3. Patterned Si NM Transfer (Glass or flexible PET) with a SU8 pre-coating.

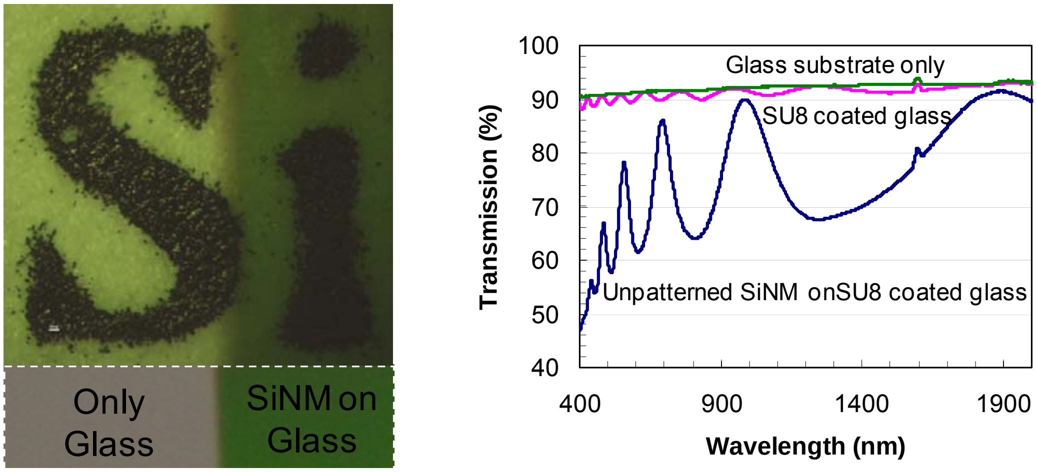

(a) (b)

Figure 3.6 (a) Microscope images of a 1 mm high “Si” through glass and SiNM; (b) Measured Transmissions of glass, SU8 coated glass and unpatterned SiNM on SU8 coated glass

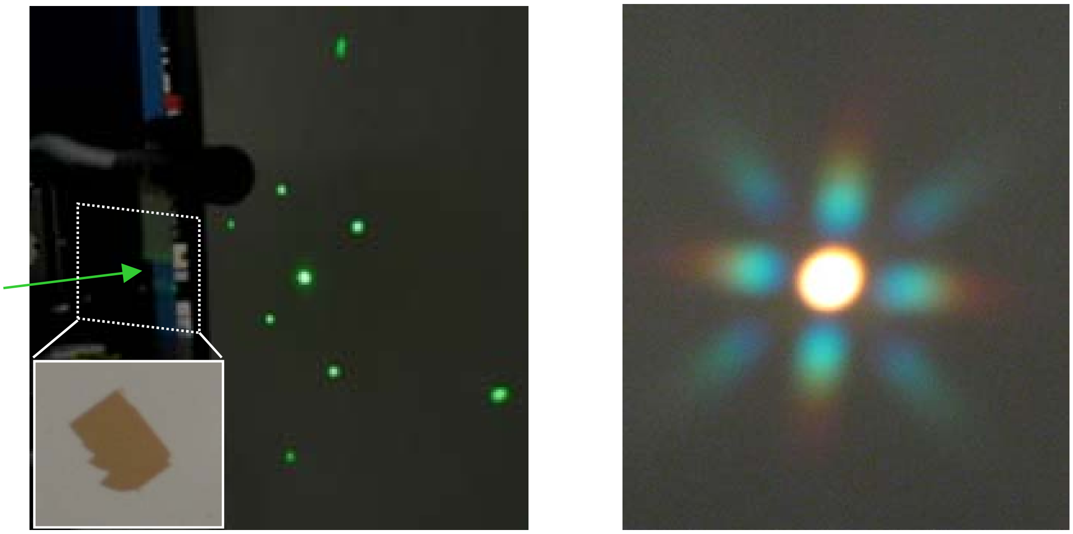

(a) (b)

Figure 3.7 Diffraction pattern obtained with (a) a green laser source with the green arrow showing the incident laser beam direction) passing through the SiNM on glass (shown as the dashed square), and (b) with a broadband QTH lamp source.

3.5 Device Characteristics

A broadband QTH light source was used for the transmission measurement of the fabricated Fano filters as shown in figure 3.8. The QTH light beam was focused onto the patterned PC area with an objective lens. The transmitted light is collected with a monochromator and a thermoelectrically cooled InGaAs detector. The transmitted signal was normalized to the reference transmission signal measured with light transmitting through the glass substrate only.

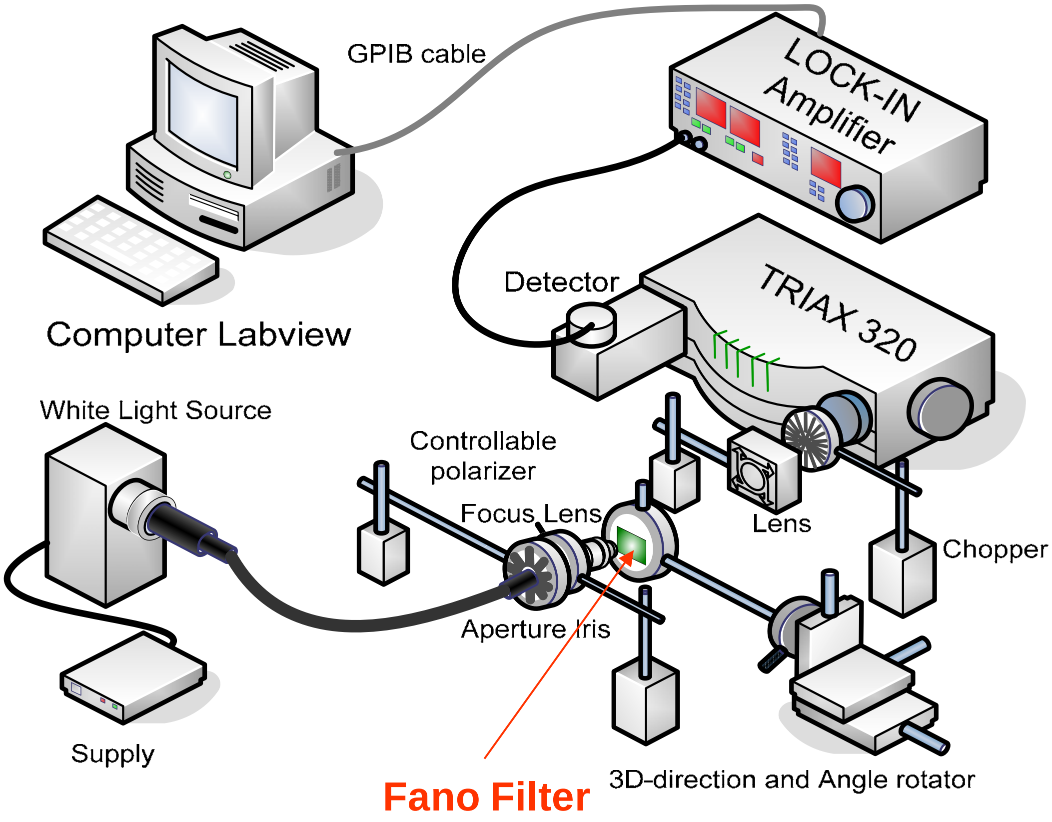

Figure 3.8 Schematic of Measurement setup for Transmission based on TRIAX 320 spectrum meter and a broadband QTH light source is used.

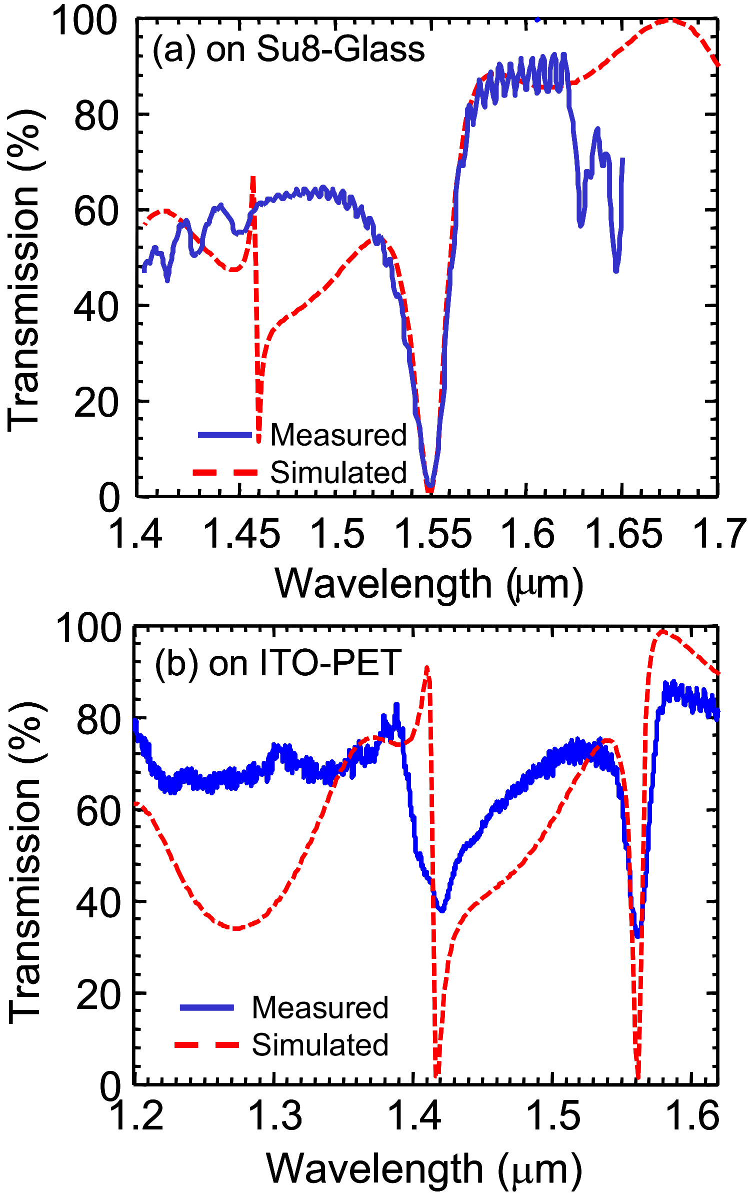

(a) a = 0.9 µm; r/a = 0.22; t/a = 0.29

(b) a = 0.6 µm; r/a = 0.19; t/a = 0.43

Figure 3.9 Measured and simulated transmission characteristics of Fano Filters for (a) a SiNM-on-glass sample; and (b) a SiNM-on-PET sample. Good agreement is seen on the spectral dip location at 1.551 µm and 1.562 µm, for (a) and (b), respectively. Note r, a, t and λ are the PC air hole radius, PC lattice constant, slab thickness and wavelength, respectively.

The measured and simulated Fano-filter transmission characteristics are shown in figure 3.9 (a) and (b) for a SiNM-on-glass substrate sample and a SiNM-on-PET flexible substrate sample, respectively.

The experimental results agree very well with the design ones, with the target wavelengths of 1.551 μm for the glass substrate and 1.562 μm for the PET substrate, respectively. Another dip appears at 1.42μm in figure 3.9 (b), for both measurement and simulation. But it is not clear why we did not see a dip experimentally at 1.46 μm in figure 3.9 (a). Further design and process optimizations can lead to higher quality factor (Q) filters with symmetric spectral responses that are suitable for ultra-compact surface-normal filters, switches, and modulators. These devices are highly desirable in high-density vertical integration of photonic systems and flexible infrared photonics.

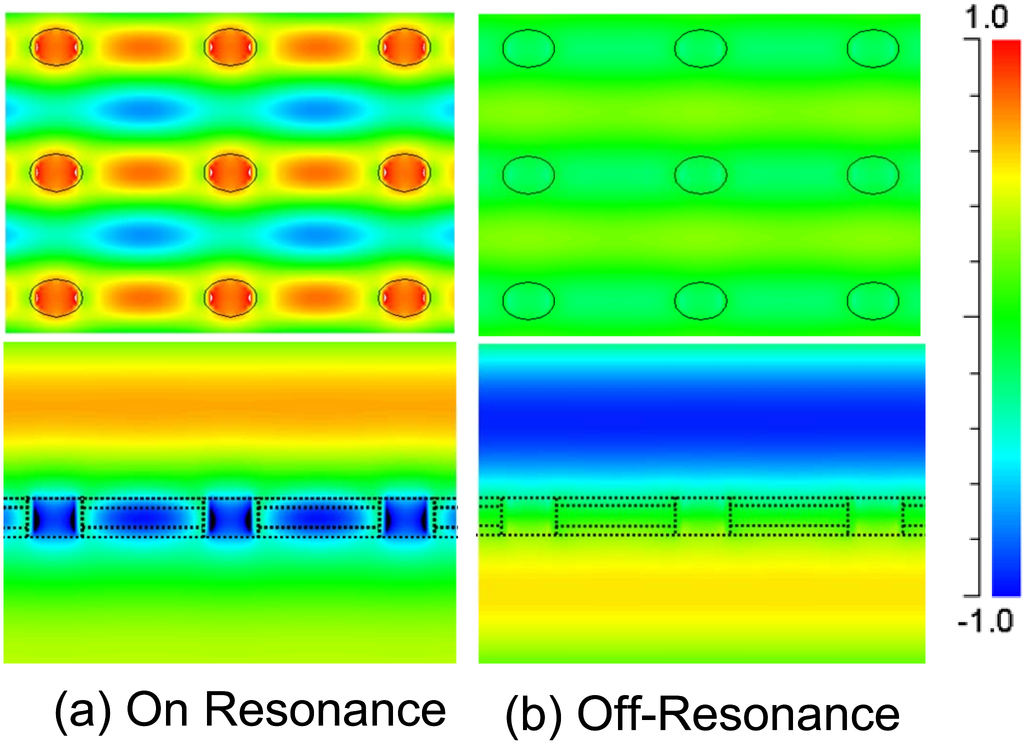

Figure 3.10. Top view (top) and cross-sectional view (bottom) of simulated field profiles for (a) the resonant mode and (b) non-resonance mode.

Note that the asymmetric line shapes observed in the filter spectral responses, which is based on Fano resonance effect, originated from the coupling between the vertical continuum of radiation modes and the in-plane discrete resonant modes, as shown in figure 3.10. In figure 3.10, the top view and the cross-sectional view of the mode field profiles are shown for both the resonant and the non-resonance modes. For the Fano resonant modes, the modes are strongly confined to the photonic crystal slab region. In contrast, the non-resonant modes have a field intensity distribution that quickly radiates away from the slab and into the surrounding medium. Based on simulation, it is feasible to achieve very high spectral selective filters with high quality factor Q and symmetric spectral responses, by varying the design parameters to adjust the mode coupling and Fano resonance properties. This is essential in high performance filter/switch/modulator applications, where high spectral selectivity and low insertion losses are required.

The cross-sectional view shows the strong interaction between vertical modes with in-plane guided resonance for the resonant modes shown in figure 3.10 (a). However, for non-resonance modes, the field intensity distribution quickly radiates away from the slab and into the surrounding medium.

We then analyze the angle- and polarization-dependent characteristics of Fano-filter with transferred SiNM on PET substrate for the first time[70, 71]. The incident angle θ, the in-plane angle Φ and the polarization angle ψ are defined in figure 3.11. Figure 3.12 shows the polarization dependence of our filters under surface-normal incidence by rotating sample with different angles Φ, defined in figure 3.11. Very little spectral shifts were observed for all three aforementioned Fano resonant modes (λ_{1-3}). This is in agreement with previously reported results based on free-standing structures [64].

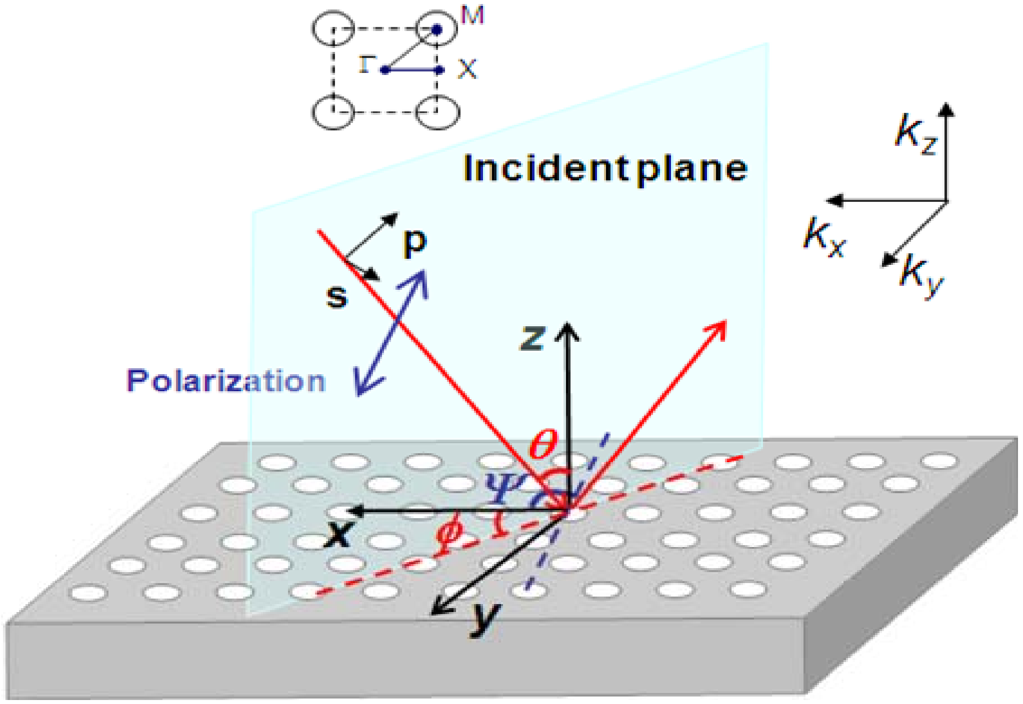

Figure 3.11 Angle and Polarization Dependence (θ: angle off surface normal; Φ: angle off ΓX direction; ψ: angle of polarization).

However, when the incident angle θ changes, all these Fano resonance modes show different shifting behavior. Figure 3.12 shows the result of one representative case, the incident beam with $\Phi = 0°$ and $\psi = 0°$, i.e., the incident beam plane is kept in parallel to the ΓX direction. As compared to the one without polarizer shown in figure 3.13 (a), it is very interesting that the dominant Fano resonant mode (λ_1) remains almost unchanged over the range of angles we measured (from 0 to 20°). At the same time, the other two modes (λ_2 and λ_3), shift towards longer wavelengths, with the increase of incident angle. Those differences between with and without polarizer can also be obviously found in the right complete transmission intensity map where the vertical blue line in figure 3.13 (b) corresponds to the 1556 nm dip in the left transmission plot.

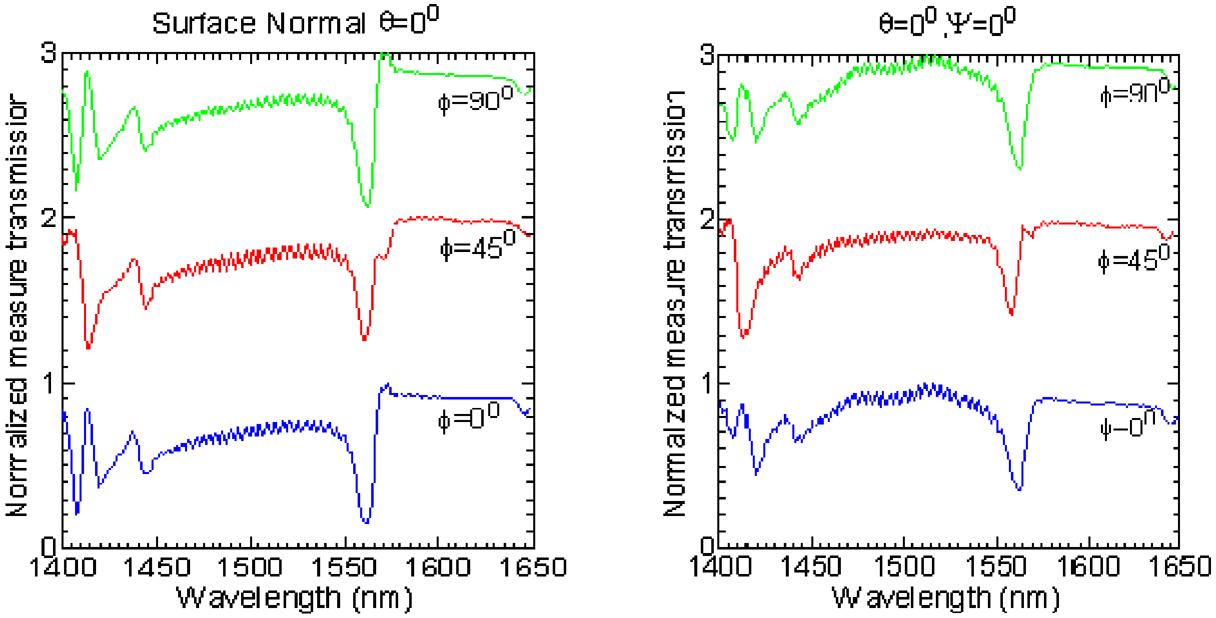

(a) (b)

Figure 3.12 Measured surface-normal polarizer-dependent transmission with different angles Φ . for (a) without polarizer, and (b) with polarizer fixed at *ψ*=0º.

To understand the influence of polarizer, we consider a random angle case by setting Φ = 22.5° and ψ = 22.5°, shown in figure 3.14 (b). By comparing the scenarios with polarizer, the transmission spectra map for the case without polarizer, shown in figure 3.14 (a), is more complicated. In figure 3.14 (b), the dominant mode (λ1) can still remain little spectral shift with incident angle less than 10°. When incident angle beyond 10°, the dominant mode shifts towards shorter wavelength. And other two modes keep shifted towards longer wavelength with the increase of incident angle. It is obvious that the modal behavior can be well controlled by using polarizer.

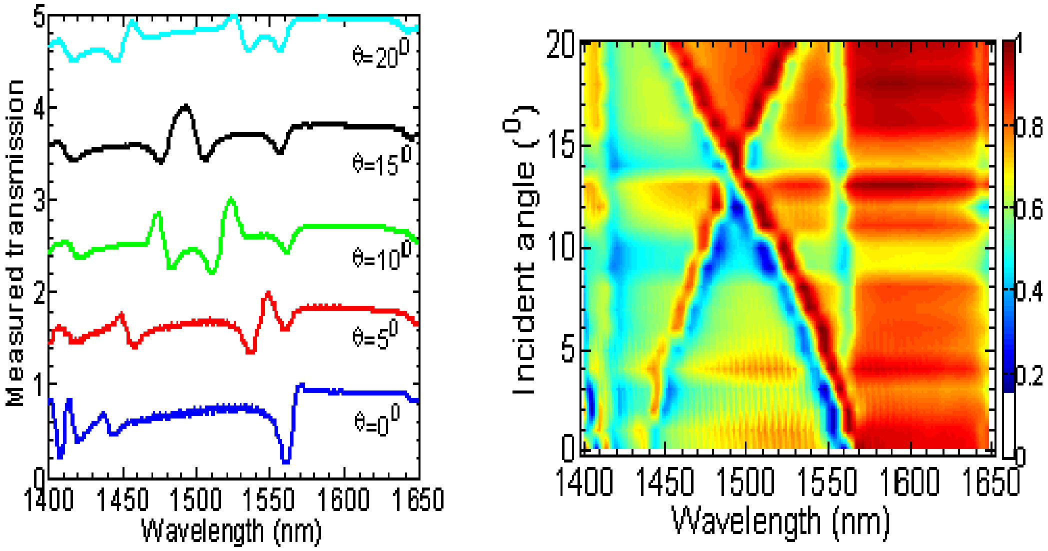

(a) without polarizer, ϕ=0º

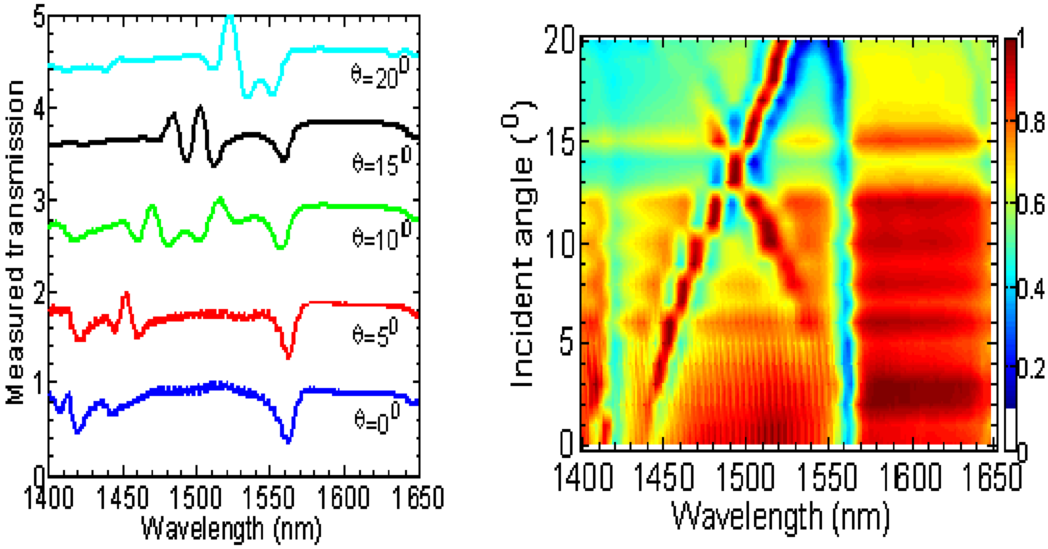

(b) with polarizer, ϕ=0º and Ψ=0º

Figure 3.13 Measured polarizer-dependent transmission with different incident angles θ for (a) without polarizer,Φ = 0º and (b) with polarizer fixed at ψ = 0º.

Similar measurements were also carried out with Φ = 45^0 and ψ = 45^0, another representative case, i.e., the incident beam plane is kept in parallel to the ΓM direction. Shown in figure 3.15, both the dominant Fano resonant mode (λ_1) and the other two modes (λ_2 and λ_3), shifted significantly. All these three modes merge at incident angle of θ = 20^0.

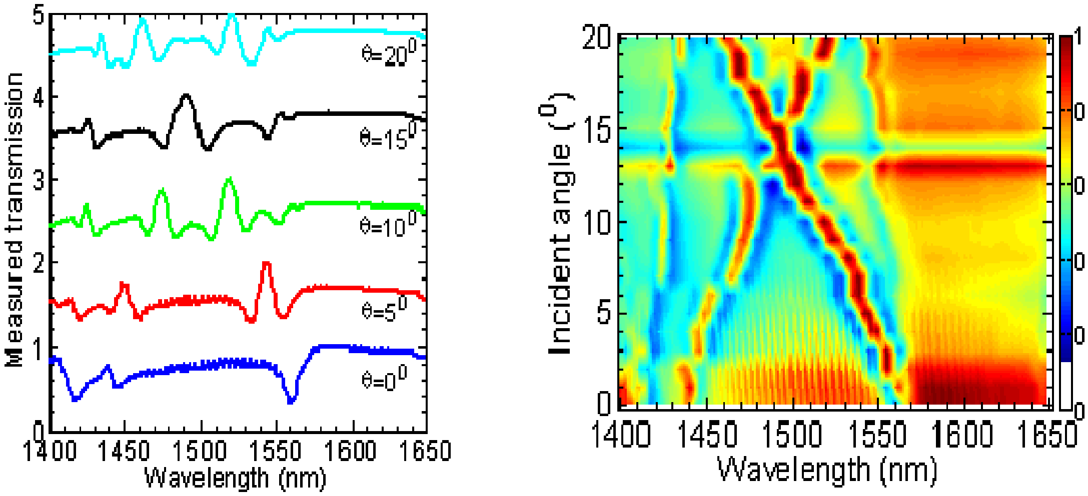

(a) without polarizer, ϕ=22.5°

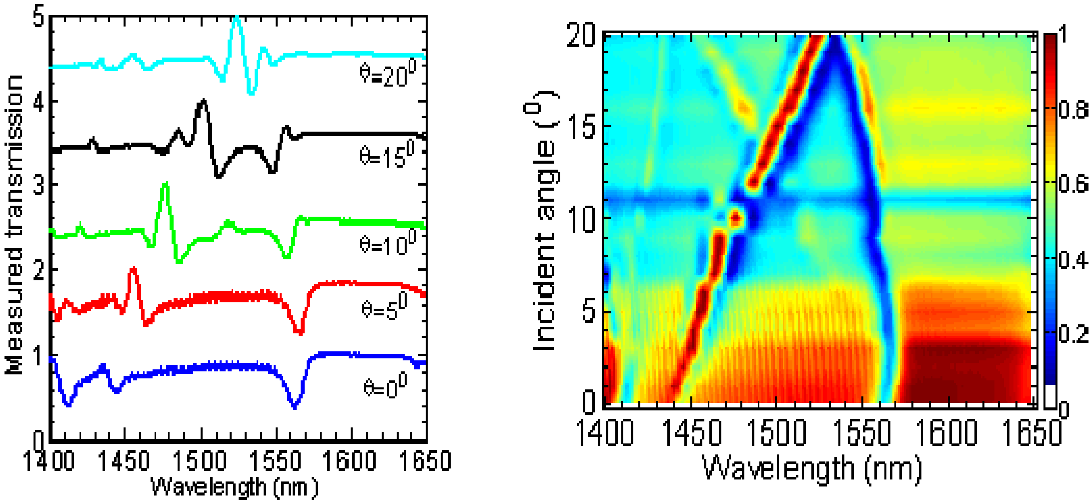

(b) with polarizer, ϕ=22.5° and Ψ=22.5°

Figure 3.14 Measured polarizer-dependent transmission with different incident angles θ for (a) without polarizer, Φ = 22.5° and (b) with polarizer fixed at ψ = 22.5°.

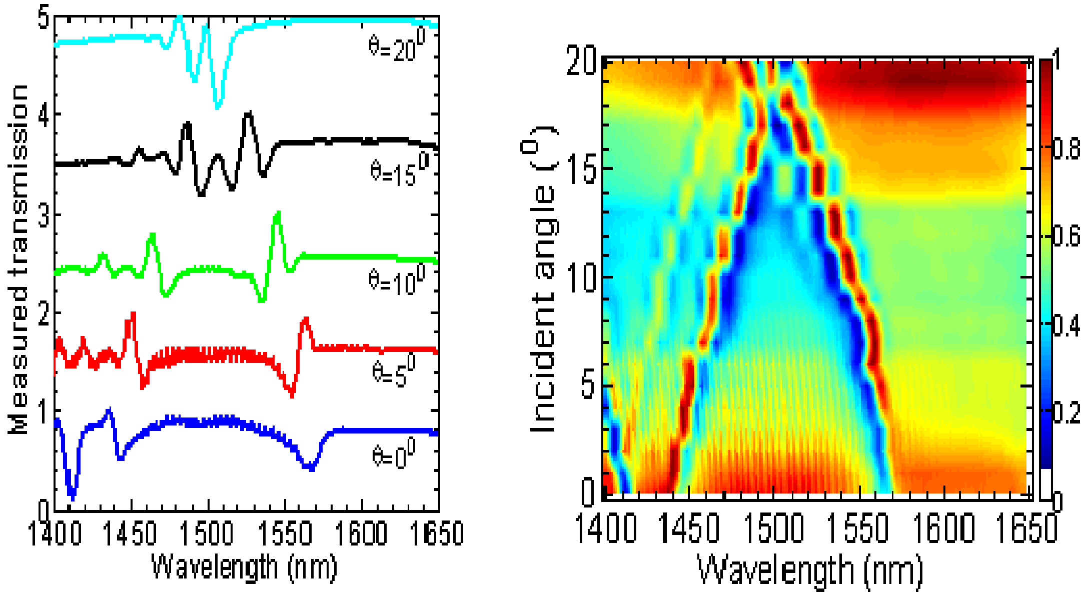

(a) (b)

Figure 3.15 Measured angle-dependent transmissions with different incident angles θ . with Φ = 45^0 and ψ = 45^0 (a) transmission plot; (b) complete transmission intensity map

The corresponding simulation results [64, 71] for aforementioned two representative cases are shown in figure 3.16 (a) and (b), respectively, where the measured transmission peaks/dips shown in figure 3.13 (b) and figure 3.15 (b) are also plotted in the dispersion chart for the corresponding incident angles. Here we correlate dispersion plot with the experiment results; as we know the in-plane momentum can be written as the equation below:

$$k_x = \frac{2\pi}{\lambda}\sin\theta_{inc}$$

$$\Rightarrow k_{\Gamma\rightarrow X}\left(\frac{2\pi}{a}\right) = \left(\frac{2\pi}{a}\right)\bullet\frac{a}{\lambda}\sin\theta_{inc} \quad \ldots\ldots\ldots\ldots\ldots\ldots\ldots\ldots\ldots\ldots..(3.1)$$

$$\overset{f=\frac{a}{\lambda}}{\Rightarrow} k_{\Gamma\rightarrow X} = f\bullet\sin\theta_{inc}$$

(Where θ=0 corresponds to Γ symmetric point.)

If we keep symmetry direction and incident angle constant during one measurement, from equation 3.1, changing the wavelength corresponds to a movement along one of the dotted lines in figure 3.16 (b). The measurement and the simulation results agree very well.

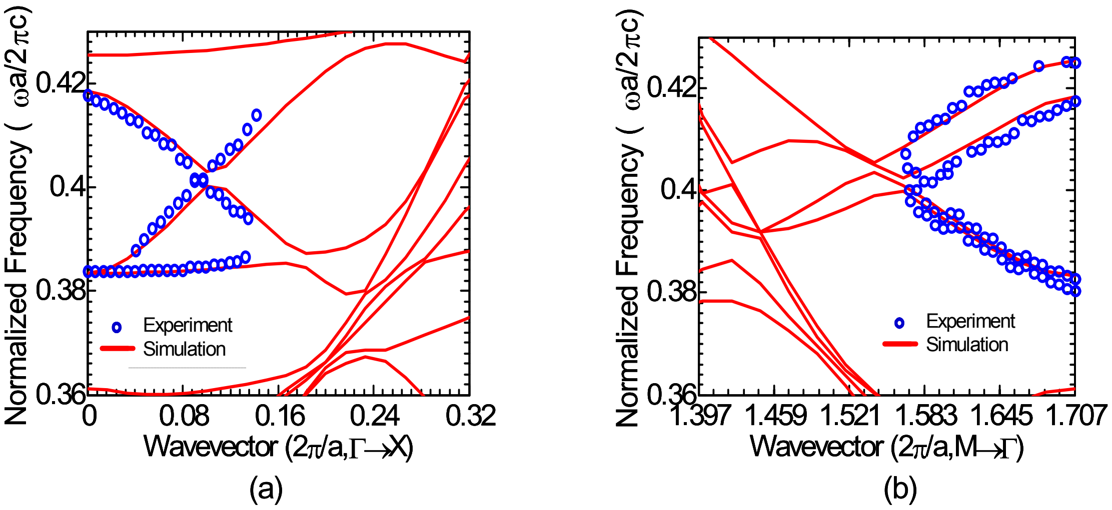

Figure 3.16 Measured angle-dependent transmissions with different incident angles θ for (a) $\Phi = 0^0$ and $\psi = 0^0$, and (b) $\Phi = 45^0$ and $\psi = 45^0$. Note measured transmission peaks/dips (circles) agree well with the simulated dispersion curves for different incident angles.

In conclusions: Surface-normal optical filters based on Fano resonances in patterned SiNMs on glass were proposed, designed and fabricated, based on a disruptive nanomembrane wet transfer process. The measured filter transmission results agree well with designs using a finite difference time domain (FDTD) technique. Switches, modulators and photodetectors with high quality factors suitable for high density integration of photonic and electronic integration may be further realized based on the same operation principle and the nanomembrane technology. For the desired angular and polarization properties including ultra-compact surface-normal filters, switches, and modulators, which are very significant important for high-density vertical integration of photonic systems and flexible infrared photonics. The flexible integration schemes of stacked SiNMs can lead to simplified device fabrication processes for high performance flexible photonics and high density photonic integration systems.

CHAPTER 4

SI-BASED MEMBRANE REFLECTORS

4.1 Introduction

Surface-normal ultra-compact narrowband optical filters and broadband reflectors are essential components for numerous device applications. They can be used in optical switches, modulators, lasers, sensors and beam steering devices. One dimensional sub-wavelength grating (SWG) structures have long been recognized for this purpose. Both narrowband filters and broadband mirrors [63, 72-76] based on SWG have been demonstrated. On the other hand, two-dimensional photonic crystal slab (2D PCS) structures hold great promises in realizing more compact photonic devices and they can be used for both in-plane and vertically-coupled light guiding and manipulating. In this regard, Fano resonance can be explored for device applications. Based on Fano resonances, out-of-the-plane optical mode coupling in 2D PCS becomes feasible, because the in-plane guided resonances above the lightline are strongly coupled to the out-of-the-plane radiation modes due to phase matching provided by the periodic lattice structure[3]. In recent years, devices based on Fano resonances such as narrowband filters [63, 76, 77] and broadband reflectors [64, 78, 79] have been reported. Recently, we also reported narrow band Fano filters and broadband membrane reflectors with patterned silicon nanomembranes (SiNM) transferred onto glass and flexible polyethylene terephthalate (PET) substrates[80, 81], employing a low temperature wet-transfer process [71, 82]. The angular and polarization properties of Fano filters can also be tailored with the dispersion engineering, which is highly desirable for photonic integration applications [71, 83]. However, none of the previous work demonstrated resonance control which is needed in many practical applications.

Here we report the post-fabrication resonance control for broadband membrane reflectors with precise control of cavity resonances, based on effective index control of low index medium surrounding patterned SiNM device layer.

4.2 Membrane Reflector Design

The Membrane reflector design was carried out based on three dimensional finite difference time-domain (3D FDTD) simulations and rigorous coupled-wave analysis (RCWA) techniques [4, 84]. With the control of design parameters, broadband reflectors with various spectral bandwidths and different peak reflections can all be realized. Figure 4.1 shows the setup configurations for our simulation.

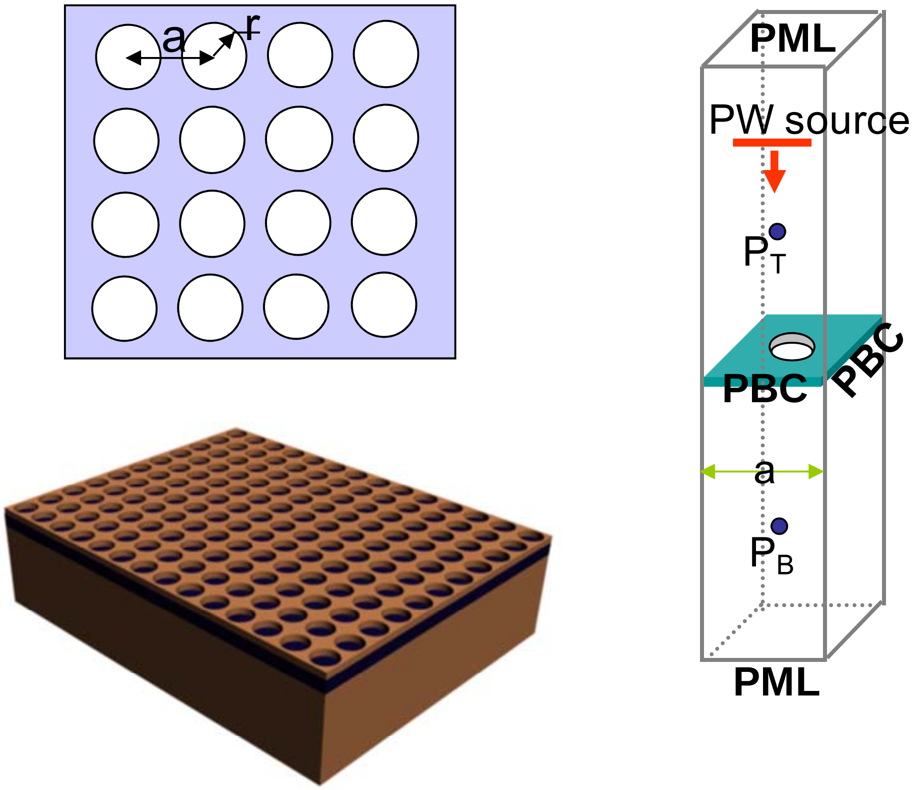

(a) (b)

Figure 4.1 (a) Schematic of patterned silicon membrane reflector structure with square lattice; (b) Simulation configurations with perfectly matched layers (PML) and periodic boundary condition (PBC), the plane wave source is used.

A typical design is given in figure 4.2, as we can see three scenarios were investigated: ‘ASA’ (Air (top)-Silicon-Air (bottom)), ‘ASO’ (Air (top)-Silicon-Oxide (bottom)) and ‘OSO’ (Oxide (top)-Silicon-Oxide (bottom)),

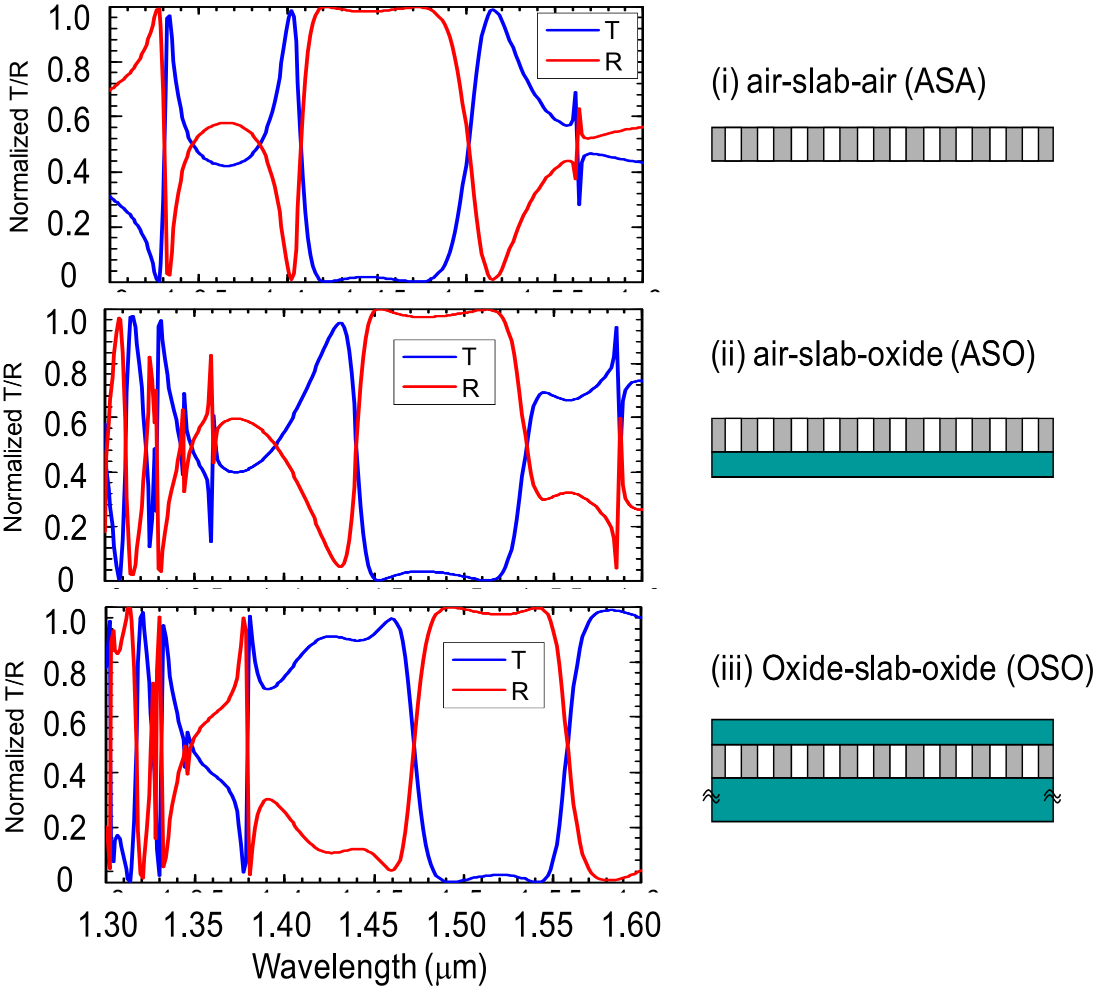

(a) (b)

Figure 4.2 Simulated reflection/transmission results of membrane reflector (a=0.9 μm, r/a=0.26, t=0.34 μm) with normal incident light for (i) air-slab-air, (ii) air-slab-oxide and (iii) oxide-slab-oxide.

4.3 Device Fabrication

The PCS structure was fabricated on silicon-on-insulator (SOI) wafers, using E-Beam lithography and plasma dry-etching processes [4]. The target wavelength is around 1550 nm.

A membrane reflector fabricated on the SOI substrate is shown schematically in figure 4.3 (a). It is also denoted as the "ASO" structure, following the sequence of the vertical confinement layers: Air (top)-Silicon-Oxide (bottom). Shown in figure 4.3 (b) and figure 4.3 (c) are the cross-sectional view and top-view of the scanning electron micrographs (SEMs) of the fabricated membrane reflectors on SOI substrates, respectively. The periodicity (a) and air hole radius (r) in this square lattice structure are 980 nm and 274 nm, respectively. The thickness of the thin Si device layer is 365 nm. High quality etching is essential in achieving the desired reflection performance.

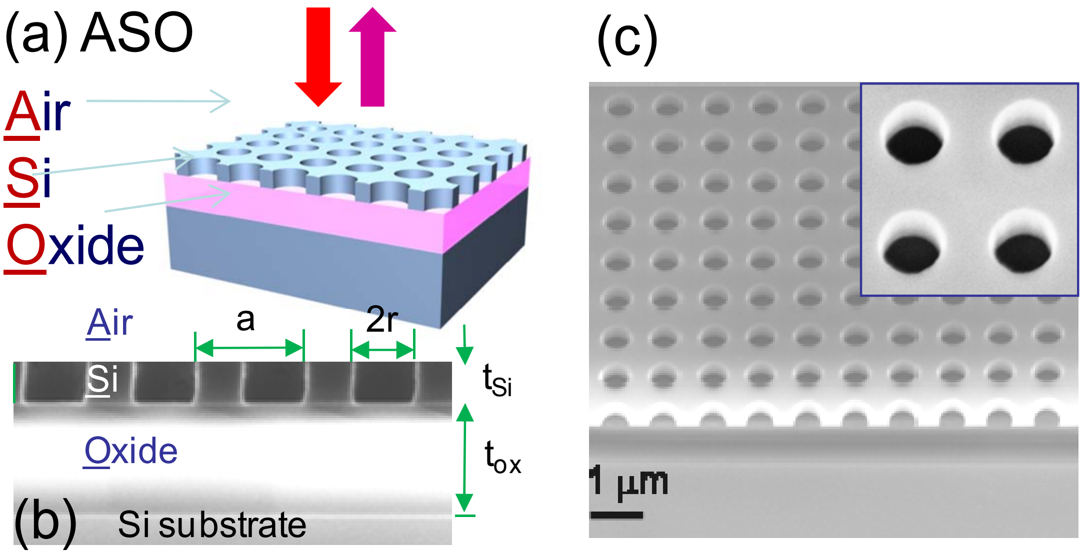

Figure 4.3 (a) Schematic of a Membrane reflector with vertical air-Si-oxide ("ASO") confinement configuration; (b) A cross-sectional SEM image of a membrane reflector on SOI, with key parameters labeled; (c) An angled, top-view SEM image of a membrane reflector, with a close-up view shown in the inset.

4.4 Device Characteristics and Resonance Control

The refllection measurement setup is sketched in figure 4.4, the Ocean Optics HALOGEN HL-2000-FHSA with fiber output is used for broadband light source, and we employee YOKOGAWA AQ6370B Optical Spectrum Analyzer (OSA) as the detector for the output light which reflected from the membrane reflectors.

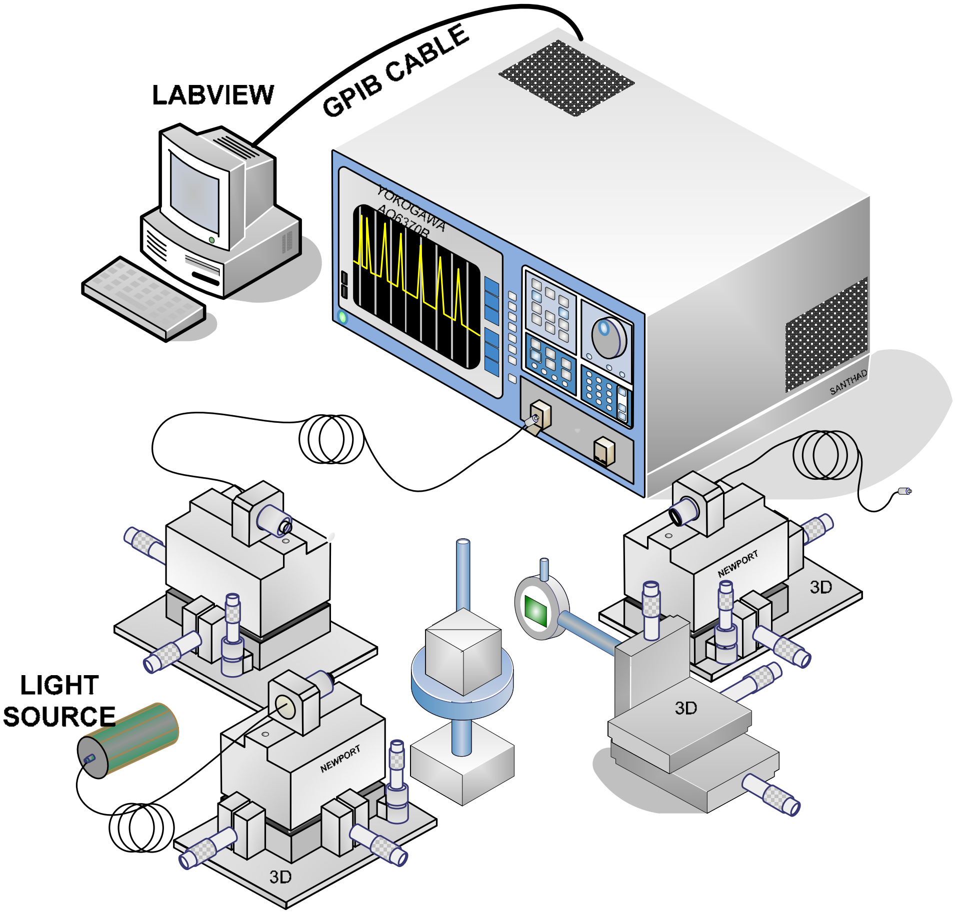

Figure 4.4 Schematic of Fiber based Measurement setup for Reflection with Optical Spectrum Analyzer (OSA) and a broadband fiber output light source is used.

Shown in figure 4.4 (a) are the measured and simulated reflection spectra. Notice that some degradation of measured maximum reflection may be due to process imperfection. Theoretically, the maximum reflection can be ~100%. The simulated electrical field plots are also shown in the figure 4.3 (b) for both the reflection band (top) and the transmission band (bottom).

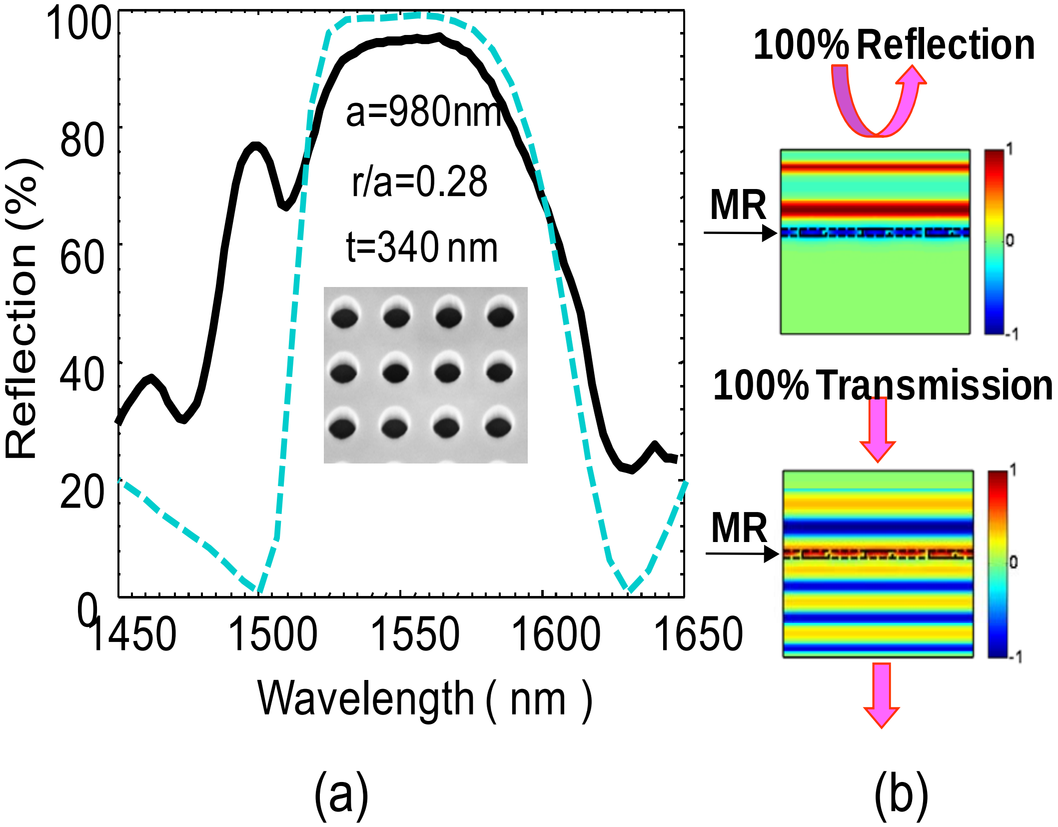

Figure 4.4 (a) Measured and simulated reflection spectra for a membrane reflector with a = 980 nm, r/a = 0.28, t_{Si} = 340 nm and t_{ox} =1 μm. (b) The simulated electrical field plots are also shown for both reflection band (top) and transmission band (bottom).

It is well known that photonic crystal and Fano resonance spectral properties can be controlled by varying design parameters, such as the lattice structure and material indices, including the medium surrounding the patterned photonic crystal layer[85]. As a result, post-process spectral tuning is feasible by controlling the effective indices of surrounding environment. In order to precisely trim the spectral locations, we report the following two approaches to precisely controlling the effective indices below and above the Si device layer: (1) To realize a spectral blue-shift by reducing the effective index of material below the device with controlled partial-etching of SiO_2 buried oxide (BOX) layer and; (2) To achieve a spectral red-shift by increasing the effective index of material above the device with oxide deposition on its top.

The processes for realizing blue-shift are shown schematically in figure 4.5 (a) (i-iii), along with the corresponding cross-sectional SEM images shown in figure 4.5 (b). With controlled BHF etching times, the buried oxide BOX layer is partially etched away, which results in reduction in the effective index of the bottom oxide layer (in figure 4.5 (i, ii)). When the BHF etching time is sufficiently long (e.g. >7 min, in figure 4.5 (iii)), the Si device layer is completely released (still supported at edges) with bottom layer effective index approaching the index of air ("ASA" stands for Air (top)-Silicon-Air (bottom)).

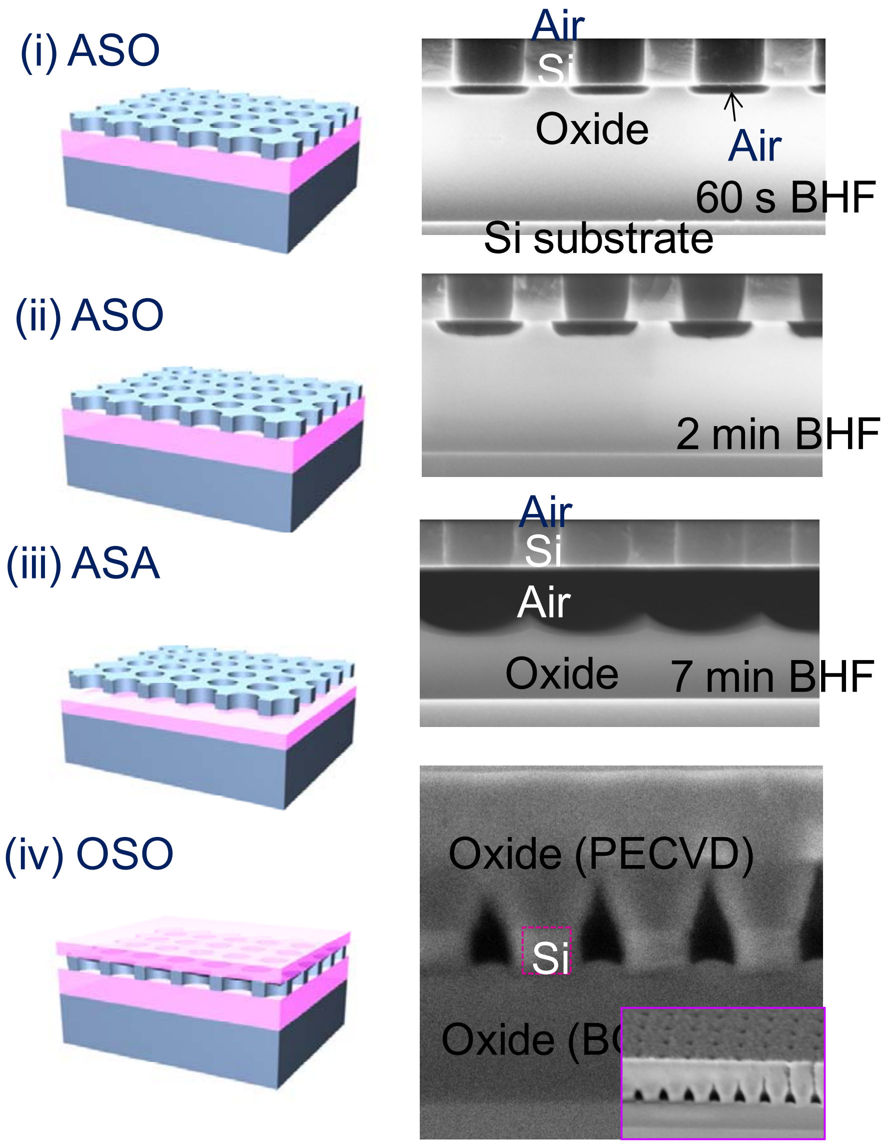

(a) (b)

Figure 4.5 (a) Schematic and (b) cross-sectional SEM images of spectral trimming processes with controlled BHF etching time (60 sec., 2 min., 7 min.) of BOX layer for blue-shift and controlled oxide deposition for red-shift.

The measured broadband reflection results are shown in in figure 4.6 for different BHF etching times. The measured spectra are shown in figure 4.6 (a), where the spectra curves are shifted by a multiple of 100's to have a better view for comparison.

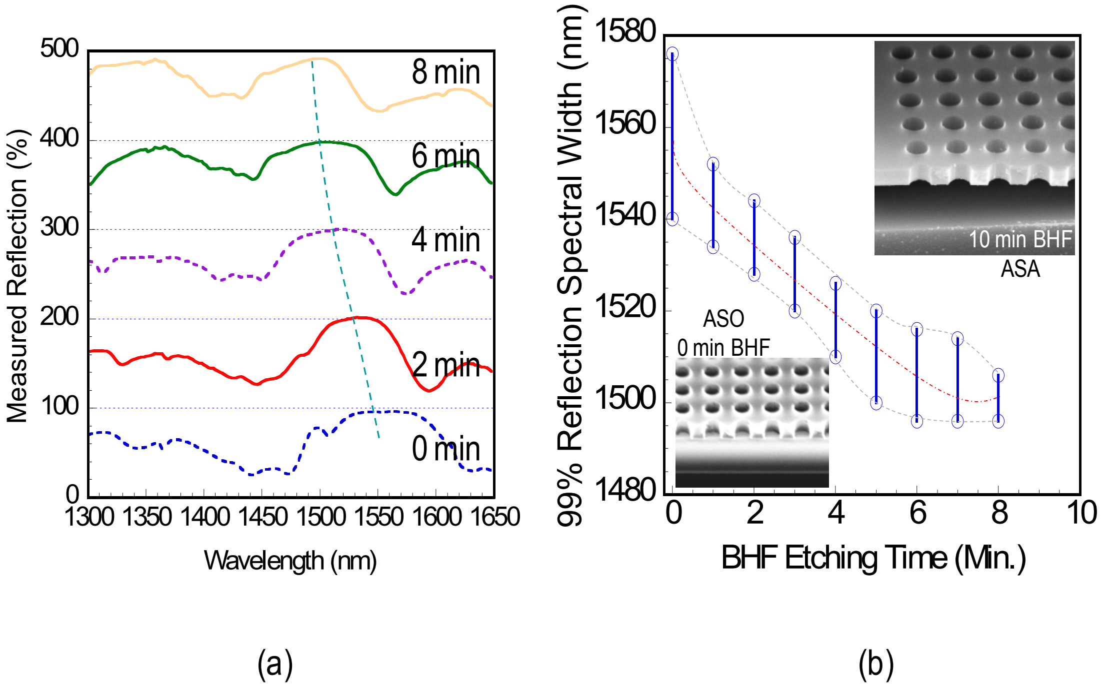

Figure 4.6 Measured reflection characteristics: (a) Reflection spectra for Membrane reflectors with different BHF etching time (from 0 to 8 min). The reflection spectra are shifted up by multiples of 100's for different etching times to provide a better view of the spectra. (b) 99% reflection spectra bands for different BHF etching times. Shown in the insets are the SEM images for membrane reflector with ASO (0min BHF etching time) and ASA (10 min BHF etching time) configurations.

The reflection spectra bandwidths with 99% reflection are summarized in figure 4.6 (b). The center wavelengths (red dotted line in figure 4.6 (b)) shifted almost linearly for etching time less than 7 min., when the top portion of BOX oxide layer are completly removed (in figure 4.5b)iii). Beyond 7 min., further etching has little impact on the center wavelength of the reflection bands, simply because the effective index underneath of the device has no more changes (air). The results indicate that the Fano resonance shift is only related to the effective index of very thin layers (~200 nm) above and below the patterned SiNM layer where field interaction is strong (in figure 4.4 (b)). As seen in figure 4.6, a total of 53 nm blue-shift was obtained for a total etching time of 6 min. It is worth mentioning that similar trends can be found for the reflection spectra bands at different reflection levels (e.g. 99.9%, 95%, etc.).

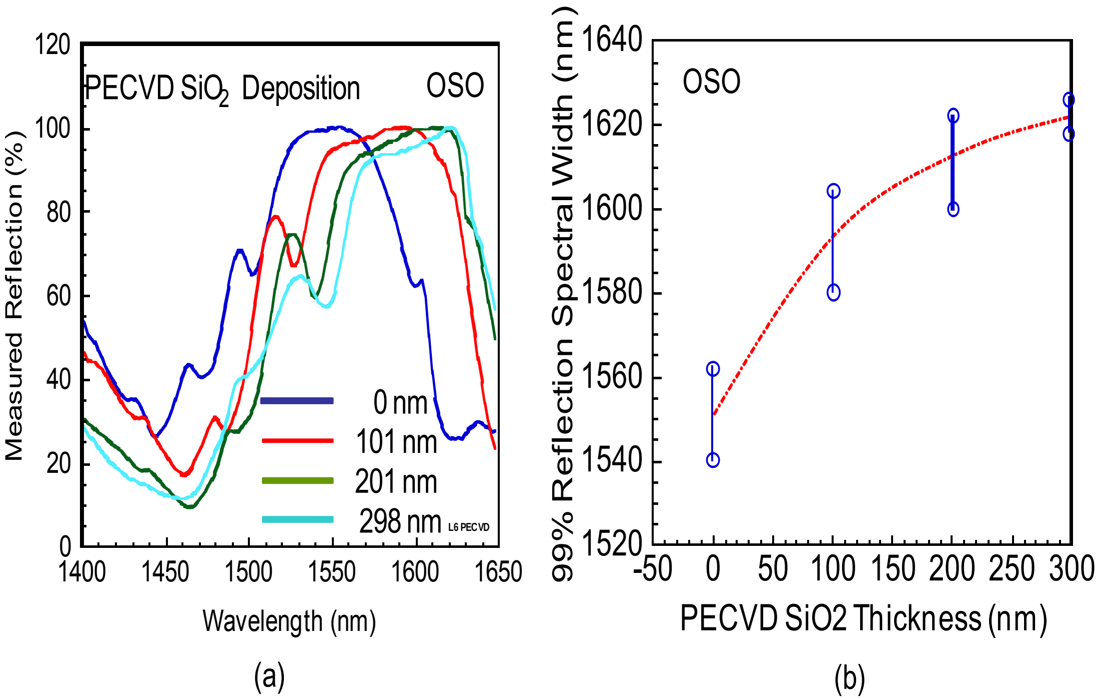

Figure 4.7 (a) Measured reflection spectra for different SiO_2 thicknesses deposited on top of the Si device layer (from 0 to 298 nm); and (b) 99% reflection spectral widths for different PECVD oxide thicknesses.

Similarly, red-shift via spectral trimming can also be realized with the addition of oxide layer surrounding the patterned Si device layers with different thicknesses. This can be accomplished with either PECVD deposition of oxide on the top of Si device layer, or with spin-on-glass (SOG) backfilling of the air regions above, below and in the air holes. The oxide deposition process is schematically shown in figure 4.5 (iv), where 1 µm thick PECVD oxide is deposited on the patterned Si layer. Notice that the air hole is partially filled with oxide deposited during the initial phase of deposition process. This is typical where PECVD oxide cannot fill nano-scale air holes effectively. A more conformal process can be introduced to fill the air holes more effectively by the spin-on-glass (SOG) coating process. The Oxide (top)-Silicon-Oxide (bottom) structure is denoted as "OSO".

The measured reflection results are shown in figure 4.7, for different PECVD oxide thicknesses. Notice a saturation behavior in resonance shift is observed for the oxide layer beyond 150 nm. For the initial oxide deposition thickness from 0 to 100 nm, the resonance can shift 45 nm towards longer wavelengths at a rate of 0.45 nm (wavelength) /nm (oxide).

Finally, we demonstrated spectral trimming with SOG are on the same SOI sample, as shown in Figure 4.8. Beginning with an as-fabricated ASO structure, which has a peak reflection at 1551 nm, the spectral peak first shifted to 1500 nm after controlled BOX layer removal ("ASA" shown in figure 4.5 (iii)). The peak reflection then shifted back to 1580 nm after the sample was back-filled with spin-coated SOG solution (also denoted as "OSO", as shown in figure 4.5 (iv)). The SOG solution used here is the Honeywell Accuglass® 211 with thickness of ~200 nm.

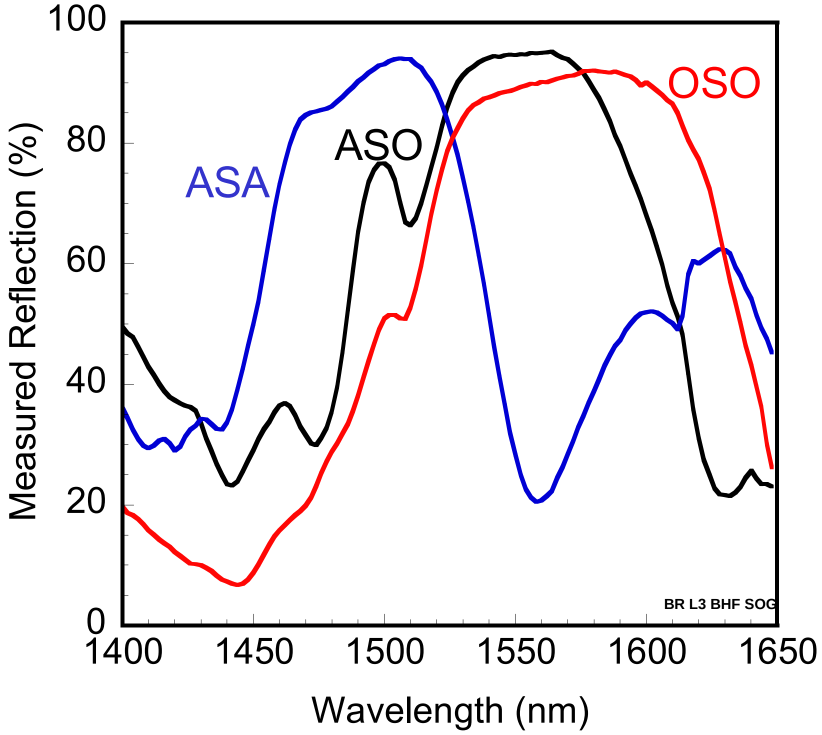

Figure 4.8 Measured reflection spectra for Membrane reflectors with three configurations: ASO (air-slab-oxide) as fabricated, ASA (air-slab-air) realized with a 4 min BHF etching from the ASO structure and OSO (oxide-slab-oxide) with SOG backfill of the ASA structure.

4.5 Potential Applications

Fano resonance broadband reflectors are realized with the controlled spectral locations based on the post-fabrication spectral processes. Spectral trimming was accomplished by partially removing the buried oxide layer (BOX) underneath the device layer, or by controlled SiO_2 film deposition on the top. Resonance tuning was demonstrated with a turning range over 50 nm for both blue- and red-shifts, making it a practical post-process design tool for Fano resonance trimming for both narrowband filters and ultra-compact broadband reflectors.

CHAPTER 5

MR-VCSELS

5.1 Introduction

Since invented by K. Iga [86] in 1979, Vertical Cavity Surface Emitting Lasers (VCSELs) are becoming more and more promising semiconductor optoelectronic devices which emit the beam perpendicular to the active region of the laser, from top or bottom surfaces. A VCSEL provides unique advantages over the traditional edge-emitting lasers most used in the current fiber optic communications [87-90]. There are various applications including sensors, optical interconnects & communications, Gigabit Ethernet, light sources, laser displays, laser printers, etc. Especially, a 1550 nm VCSEL can significantly improve data process efficiency and increase the speed, which is exactly the main challenge nowadays to develop a high-power VCSEL device with an emission wavelength of 1550 nm [91-93].

A typical vertical cavity surface emitting laser (VCSEL) is formed by two Distributed Bragg Reflectors (DBRs) and active gain medium in between as shown in figure 5.1[94]. To obtain the required high reflection the number of pairs of AlGaAs/GaAs DBRs has to be ~30 which is about 3 μm in thickness. This drawback of DBRs limits the further application in on-chip integration with other semiconductor components, tunable lasing and so on.

Photonic crystals Membrane Reflectors (MRs) offer the most promising alternative to the current DBR based VCSEL technology. As we have discussed in Chapter 4, a MR can have ~100% in reflection at desired wavelength range (up to 200 nm bandwidth) with proper design and fabrication, plus a single layer Si MR itself can be successfully transferred onto any foreign substrates such as glass and plastic. High Q microcavity can be formed between the top and bottom PC membrane reflectors, where an active layer (typically III-V QW structures) is indispensably placed as the gain medium. Thus, by replacing the DBRs reflectors with Si based

MR reflectors, the reflector thickness can be reduced significantly. This can lead to ultra-compact VCSELs and heterogeneous integration with current Si CMOS manufacturing systems.

We propose Si based membrane reflector vertical cavity surface emitting laser (MR-VCSEL) as shown in figure 5.2; the laser resonator consists of two membrane reflector (MR) mirrors parallel to the wafer surface with an active region consisting of InGaAsP quantum wells (QWs) for the laser light generation in between. The planar MR-mirrors consist of layers are fabricated with photonic crystals pattern in a 340 nm thick single crystalline Si. Each layer has a SiO_2 (or air gap) buffer to yield intensity reflectivity up to 100%. The InGaAsP QW structure is designed for 1550 nm operation.

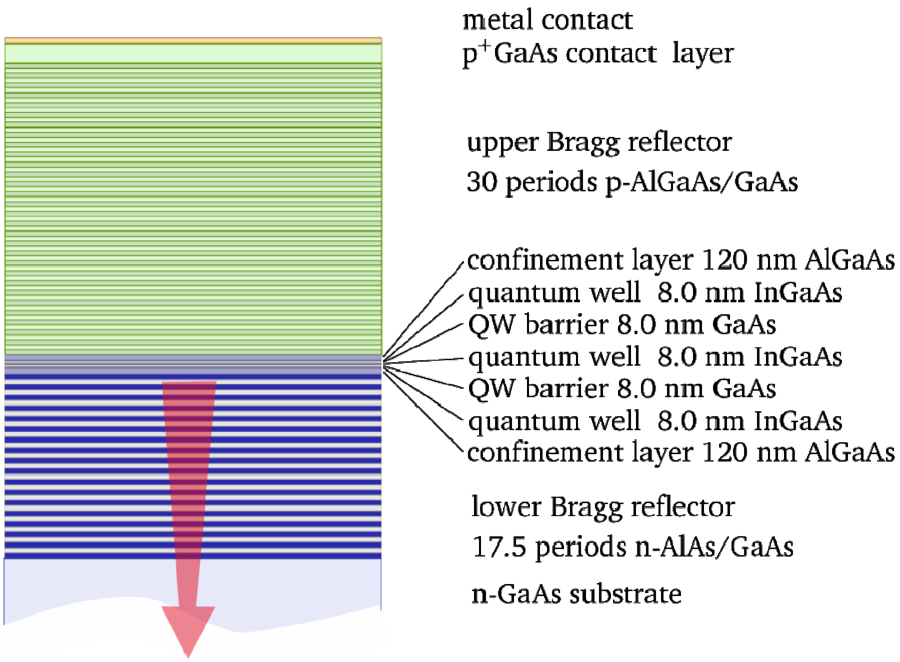

Figure 5.1 Schematic diagram of a Vertical Cavity Surface Emitting Laser (VCSEL).

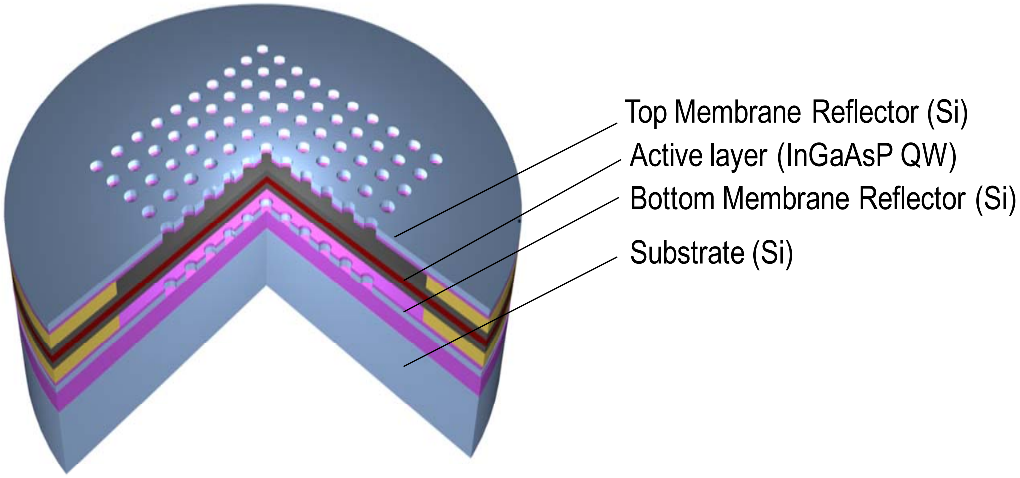

Figure 5.2 Schematic diagram of a Membrane Reflector Vertical Cavity Surface Emitting Laser (MR-VCSEL).

5.2 Top/Bottom MR and Cavity Designs

The Membrane reflector design was carried out based on three dimensional finite difference time-domain (3D FDTD) simulations and rigorous coupled-wave analysis (RCWA). By the control of design parameters, membrane reflectors with various spectral bandwidths and different peak reflections can all be realized. Figure 5.3 shows the setup configurations for our simulation.

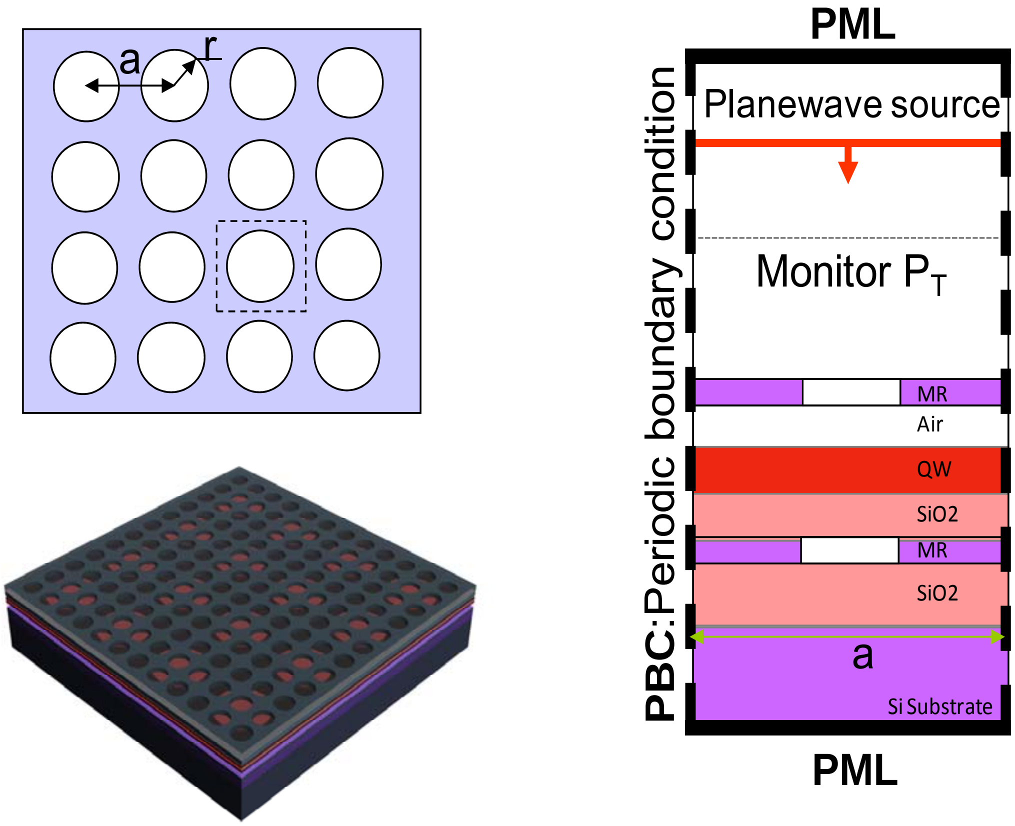

(a) (b)

Figure 5.3 (a) Schematic of patterned silicon Membrane Reflector VCSEL structure with square lattice; (b) Simulation configurations with perfectly matched layers (PML) and periodic boundary condition (PBC), the plane wave source and planar monitor are used.

The simulations were carried out to calculate the reflectivities of top MR mirror, bottom MR mirror, and the entire MR/InGaAsP QW/MR cavity. The results are shown in figure 5.4.

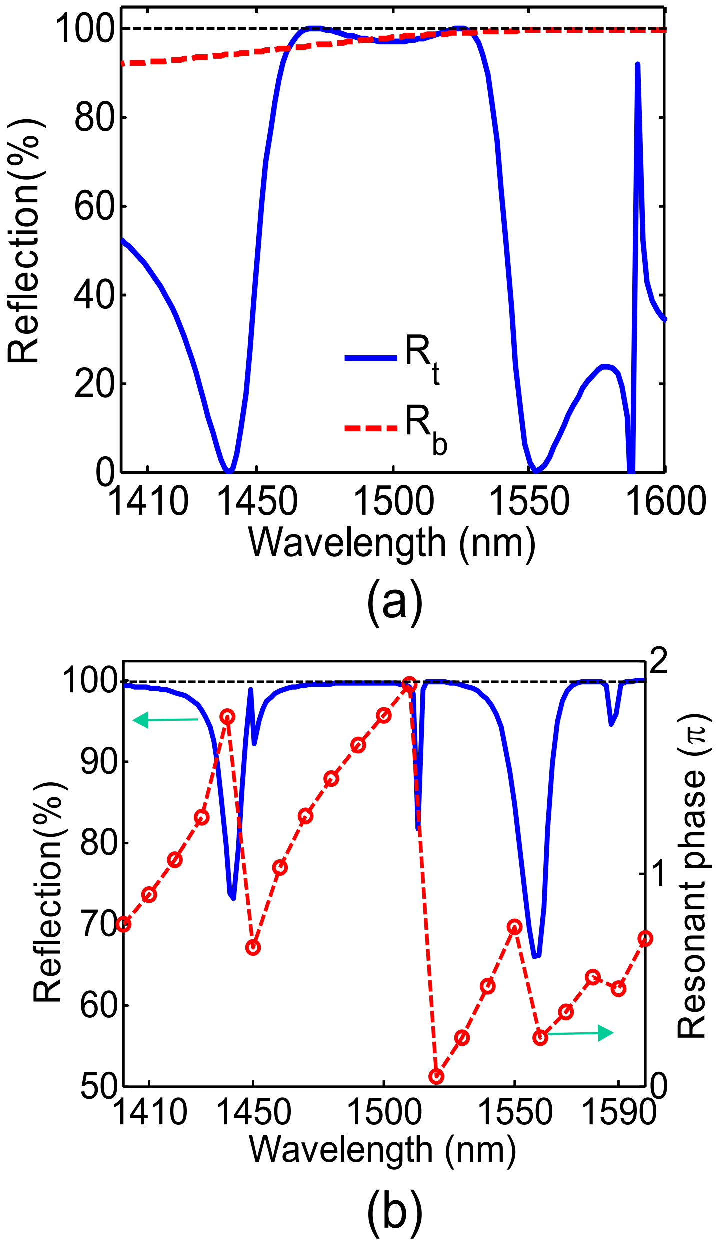

Figure 5.4 (a) Simulated Reflection properties of Top MR (r=0.25a, t=0.34 μm) and Bottom MR (r=0.45a, t=0.34 μm) with 370 nm thick SiO_2 buffer layers; (b) Simulated MR/InGaAsP QW/MR cavity mode along with the phase property.

From the cavity design in figure 5.4 (b), there is a dominant cavity mode at around 1520 nm, and by tuning the design parameters as SiO_2 buffer layer thickness (or air gap separation), the cavity mode will change accordingly as shown in figure 5.5.

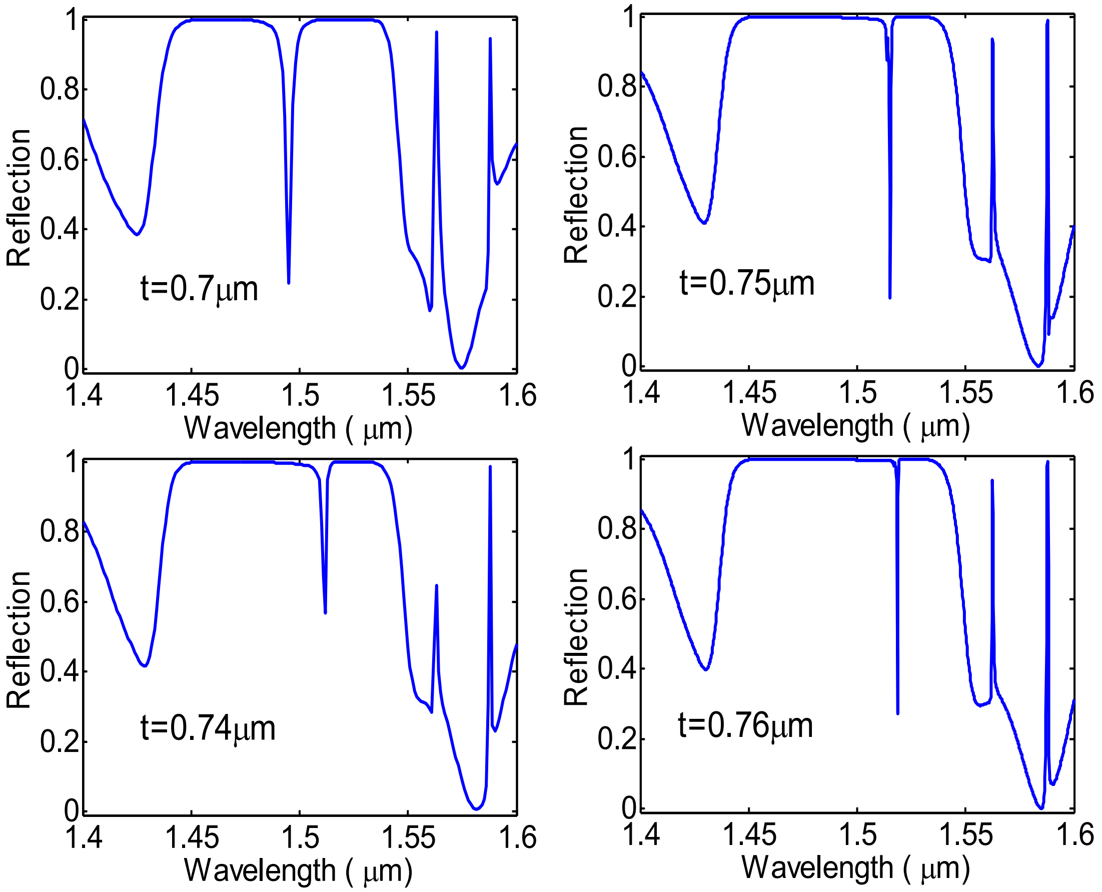

Figure 5.5 Simulated MR/InGaAsP QW/MR cavity modes along with the phase property with 370 nm thick SiO_2 buffer layers.

5.3 Component Fabrication and Integration

The MR-VCSEL device as we proposed in figure 5.2 has sandwich-like structure, from bottom to the top there are: (1) bottom membrane reflector which is fabricated in SOI substrate; (2) active region InGaAsP QW heterostructre which was designed by us and grown at the Royal Institute of Technology (KTH) in Stockholm, Sweden; and (3) top membrane reflector which is currently transferred onto glass as an alternative option.

5.3.1 InGaAsP QW Mesa Fabrication

InGaAsP Quantum Well heterostructure is shown in table 5.1. An InGaAs layer and an InP layer are used as sacrificial etch stop layers for the substrate removal and release of top heterostructure. The total physical thickness of active region is designed to be 463.4 nm (one-wavelength cavity). There are no DBRs in this heterostructure.

Table 5.1 Design Parameters of InGaAsP Quantum Well QW Cavity on InP Substrate.

Layer	Description	Material	Thickness (nm)	Dopant	Doping (cm^{-3})	Optical Index	Optical Thickness
23	Contact layer	InGaAs	40	Zn	1e19	3.444	0.0889
22	Cladding layer	InP	50	Zn	2e18	3.172	0.1023
21	Spacer layer	InP	81.5	Undoped (UID)		3.172	0.16679
20	Barrier (0.9% ts)	$In_{0.485}Ga_{0.515}As_{0.83}P_{0.17}$	7.5	Undoped (UID)		3.4	0.0165
5…19	Quantum wells (1% cs) (x8)	$In_{0.76}Ga_{0.24}As_{0.83}P_{0.17}$	7.5	Undoped (UID)		3.5	0.1355
4…18	Barrier (0.9% ts) (x8)	$In_{0.485}Ga_{0.515}As_{0.83}P_{0.17}$	7.5	Undoped (UID)		3.4	0.1316
3	Spacer layer	InP	81.5	Undoped (UID)		3.172	0.16679
2	Cladding layer	InP	50	Si	2e18	3.172	0.1023
1	Contact layer	InGaAs	40	Si	1e19	3.444	0.0889
	Sacrificial layer	InP	100	Si	5e18		
	Sacrificial layer	InGaAs	500	Si	5e18		
InP Substrate (n+)							

The photoluminescence (PL) measurement was performed on such InGaAsP QW sample over temperature from 9 K to 310 K, the PL results is plotted in figure 5.6, the PL peak at room temperature locates at 1530 nm, and during the decreasing the chamber temperature the peak moves toward shorter wavelength, the blue shift happens due to the larger semiconductor bandgap at lower temperature; furthermore, the line width also compressed during the cooling process which is shown in figure 5.7. These features are the keys we will follow in the following fabrication and integration step.

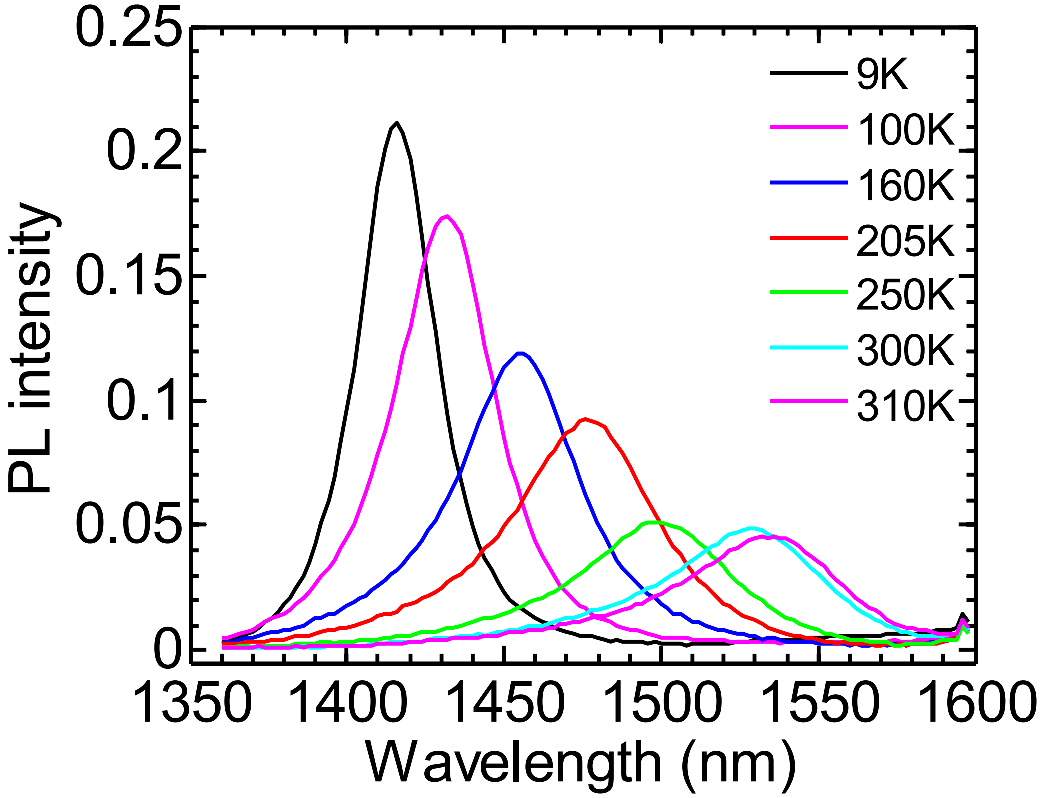

Figure 5.6 Photoluminescence (PL) Measurement of InGaAsP QW structure over temperature (From 9 K to 310 K).

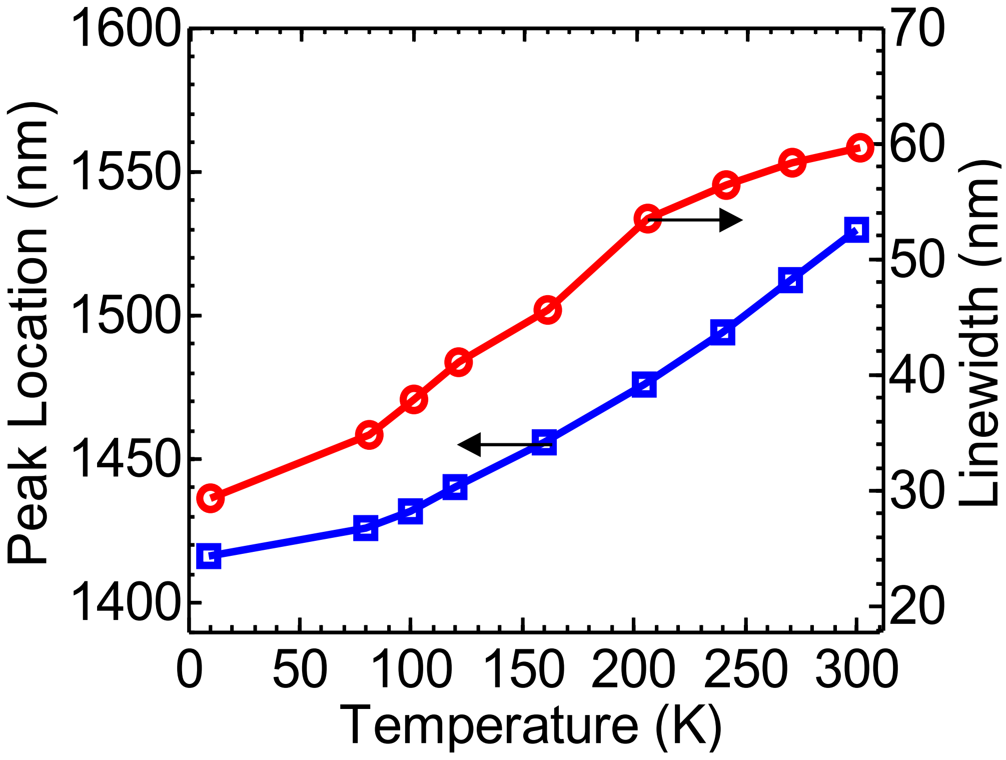

Figure 5.7 Plots of Photoluminescence (PL) Peak Location (left) and Line Width (right) over Temperature (From 9 K to 310 K) of InGaAsP QW.

We have fabricated two kinds of devices so far. One is for an optically pumping light emitter with mesa etching only for electrical isolation and lateral optical cavity definition. The other is an electrically pumping light emitter with mesa etching, as well as metallizations for both top and bottom ohmic contacts. For optically pumped light emitter, after mesa patterning process, wet chemical selective etching processes were used to define the mesa region by etching down ~100 nm to remove top p+ InGaAs (40nm) and InP (50nm). The etching recipes are shown in table 5.2.

Table 5.2 Selective Wet Etching of InGaAsP QW top Mesa

	InGaAs	InP
$HF:H_2O_2:H_2O=1:1:10$	9nm/sec	stop
$HCL : H_3PO_4=1:4$	stop	42nm/sec

For electrically pumped light emitters, the top p-type ohmic contact ring metal was deposited by lift-off technique before the similar mesa etching mentioned in table 5.2, then following the bottom trench etching and bottom n-type ohmic contact metal deposition. After such structure was done, a 400 nm thick passivation SiO_2 was deposited via PECVD; and then the open-hole process was employed to open up the contact regions, at last, the inter-connect metal was formed by lift-off. A fabricated device is shown in figure 5.8.

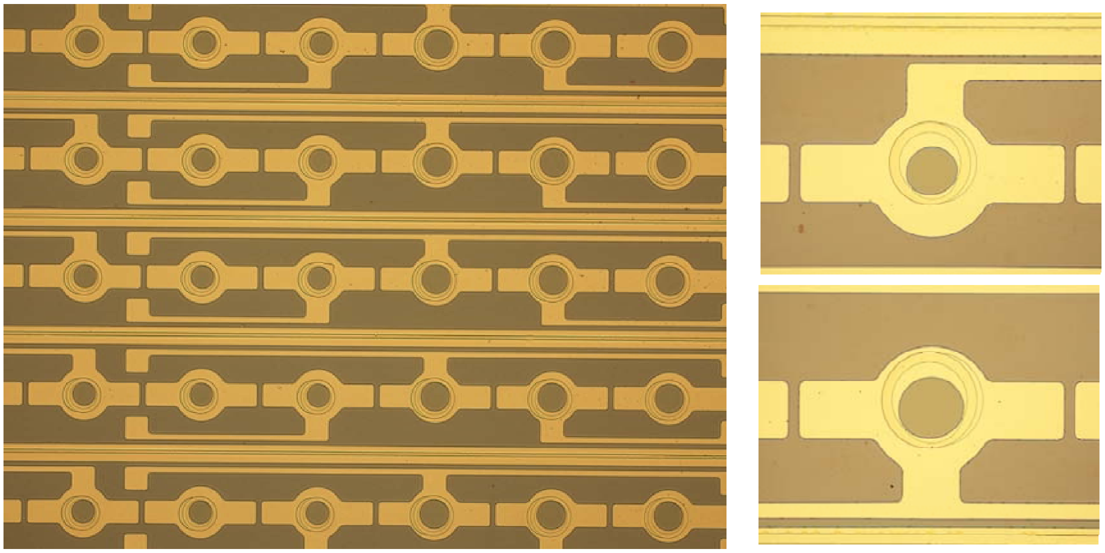

(a) (b)

Figure 5.8 Microscopy Images of Fabricated InGaAsP QW device; (a) a block area top view and (b) zoom in of two particular devices. Note the aperture size from 20 μm to 100μm.

5.3.2 MR mirrors Fabrication

As we designed in figure 5.4, the required Top/Bottom membrane reflectors were fabricated on SOI substrates by E-Beam lithography and Plasma Reactive Ion Etching (RIE), the scanning electron microscope (SEM) images showed very good hole-size (radius) control and smooth vertical side profile in figure 5.9.

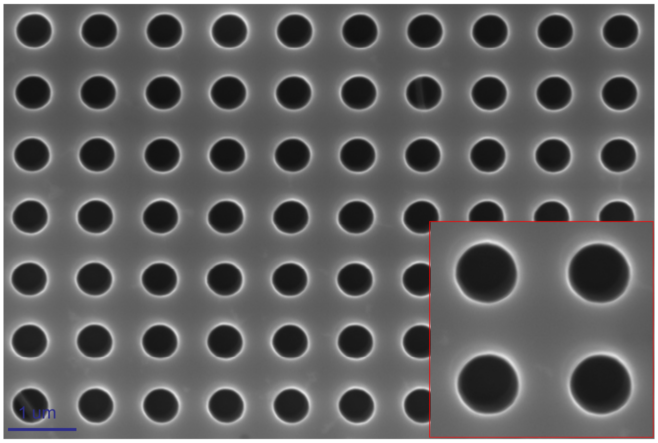

Top MR (a=980nm/r=274nm)

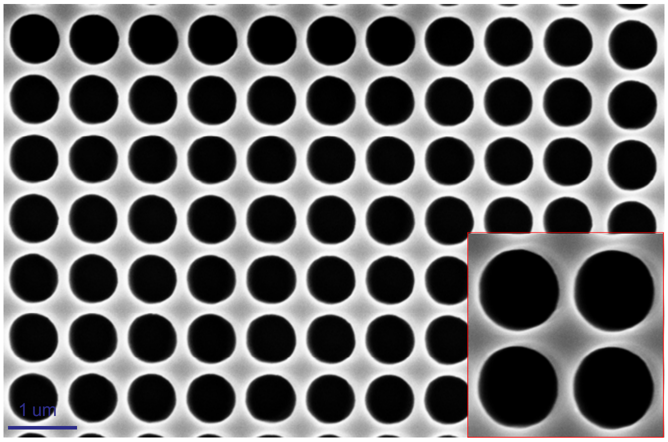

Bottom MR (a=880nm/r=390nm)

Figure 5.9 Scanning Electron Microscope (SEM) images in top view of Top/Bottom Membrane reflectors on SOI, with key parameters labeled.

Considering the cavity length formed by Top MR/QW/Bottom MR, a desired thick SiO_2 (or air gap) is required for a resonance cavity mode at 1550 nm. Low index oxide buffer layers are essential for the desired vertical index profiles between single layer bottom MR reflector, high index InGaAsP QW cavity, and top MR reflector. Therefore, we deposited a 365 nm thick SiO_2 via PECVD on the bottom MR and Scanning Electron Microscope (SEM) images of SiO2 coated MR are shown in figure 5.10, along with measured reflection result.

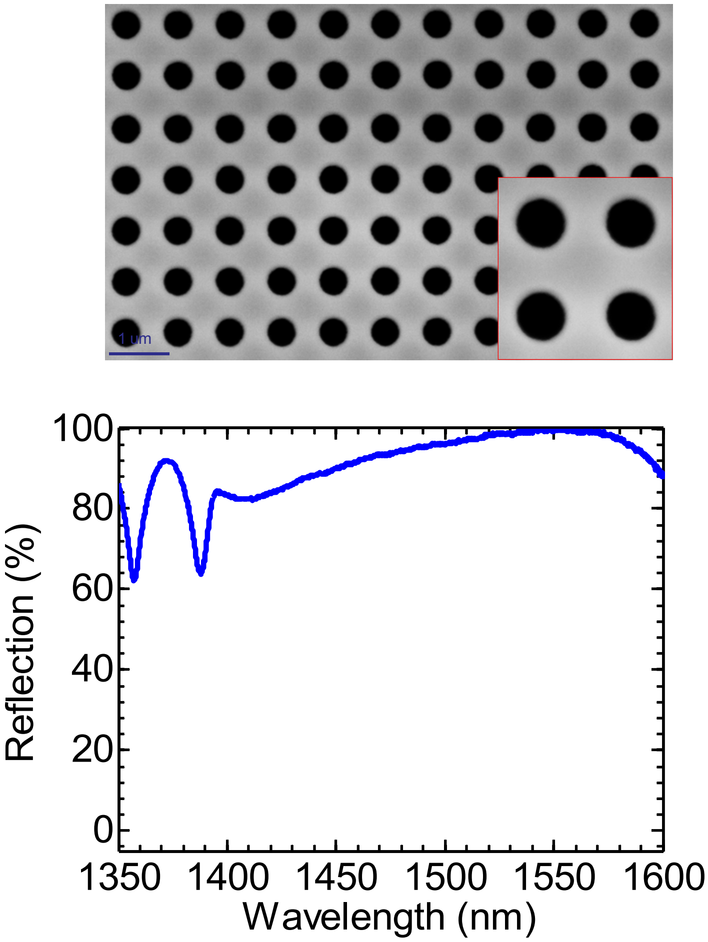

Figure 5.10 A Scanning Electron Microscope (SEM) image in top view of bottom Membrane Reflector on SOI with 365 nm SiO_2 on top and Measured Reflection via OSA.

For the top MR, we currently transferred it onto a thin (~150 μm) glass slide without SiO_2 coating, the wet transfer process is exactly same as we used for SiNM Fano Filters in Chapter 3. The transferred MR is shown in figure 5.11 along with measured reflection result.

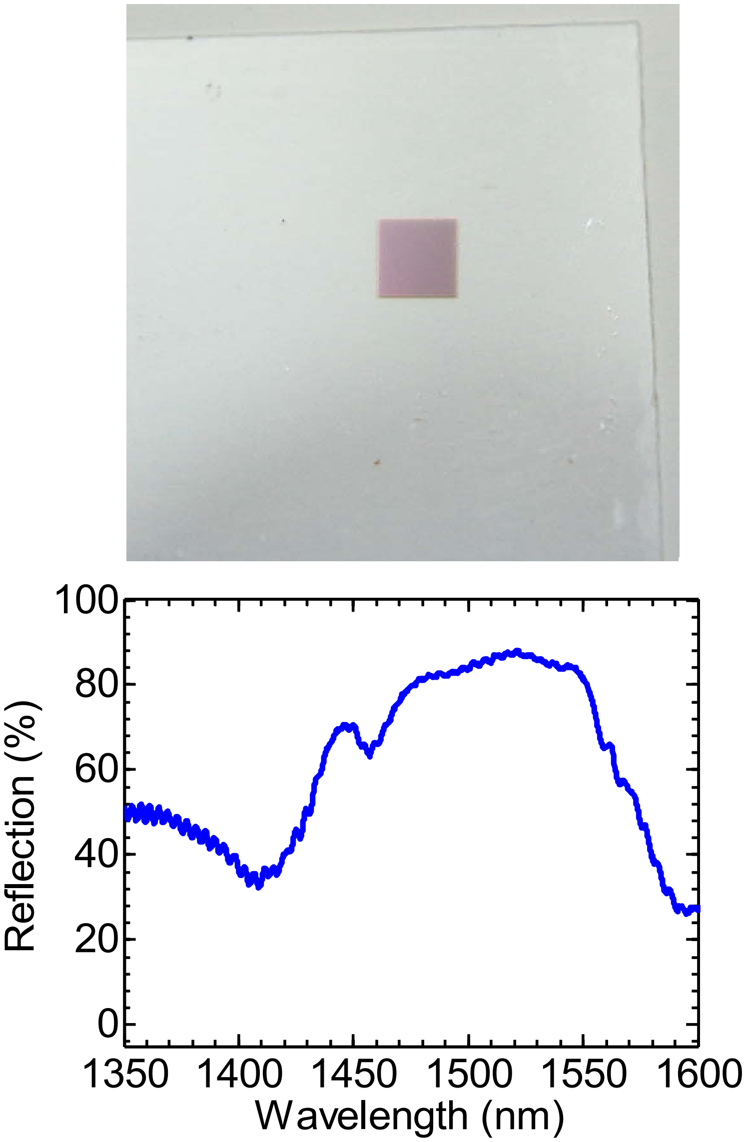

Figure 5.11 A digital single-lens reflex (DSLR) camera image in top view of top Membrane Reflectors transferred onto a glass slide and measured reflection via OSA.

5.3.3 Optically Pumping MR-VCSEL Integration

In order to construct a MR/QW/MR layer-by-layer structure, we utilize another wet transfer technique by using black wax to transfer patterned InGaAsP QW membrane onto the bottom MR mirror with proper alignment which is similar to what we used in our latest publication [95]. Basically, the top surface of InGaAsP QW was coated by black wax (Apiezon W) which requires a 10 minutes bake on the hot plate at 120 °C. Then the InP substrate, the sacrificial InGaAs layer and InP layer have been etched away by immerging it to the etching solutions in sequence. As a result, the expected InGaAsP QW membrane was obtained with the black wax still on top. At this moment, we transfer such thin film onto the bottom MR with drops of deionized (DI) water. Once the water evaporates naturally, the top black wax is removed by TCE (Trichloroethane) solvent. One transferred device (QW/MR) is shown in figure 5.12.

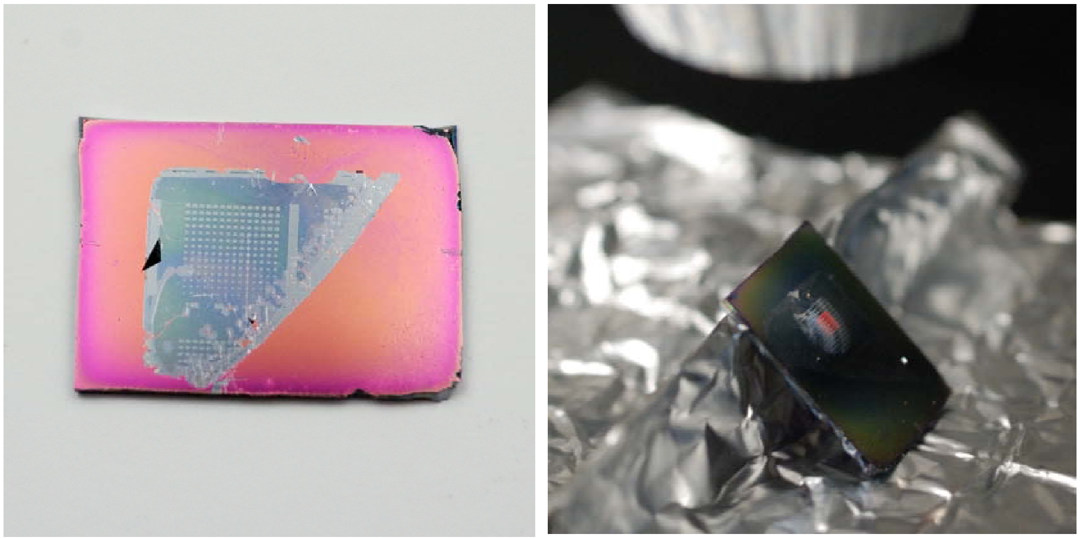

(a) (b)

Figure 5.12 A digital single-lens reflex (DSLR) camera image of transferred InGaAsP/Bottom MR (a) Top view and (b) Angled view under a beam light (the red square shows the bottom MR area seen through the QW).

5.4 Device Characteristics

We investigated mainly photoluminescence (PL) related measurements for the optically pumped MR-VCSEL with room/low temperature, also the polarization dependence was also carried out. For the electrically pumped MR-VCSEL, since we are still working on the final integration, the optoelectronic properties measurements such as pulsed Current-Voltage (I-V), Light-Current-Voltage (LIV) and Near-Field image system are performed on the main electrical component (fabricated InGaAsP QW LEDs).

5.4.1 MR Resonance Cavity Light Emitting Device (RCLED)

The final optically pumping MR-VCSEL was formed by stack the transferred top MR/glass on to QW/bottom MR as shown in figure 5.13.

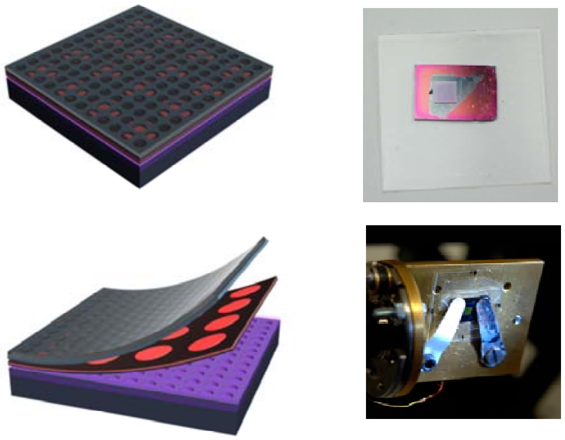

Figure 5.13 Schematic and DSLR images of integrated MR-VCSEL.

The photoluminescence (PL) setup is shown in figure 5.14 and measured PL results of MR-VCSEL device at room temperature in figure 5.15, along with comparisons to QW/MR and MR structures. The MR-VCSEL device shows a very strong stimulated emission at 1545 nm, although the full width at half maximum (FWHM) is 4 nm which is rather large due to relatively low reflectivity of the top MR mirror we used for this device.

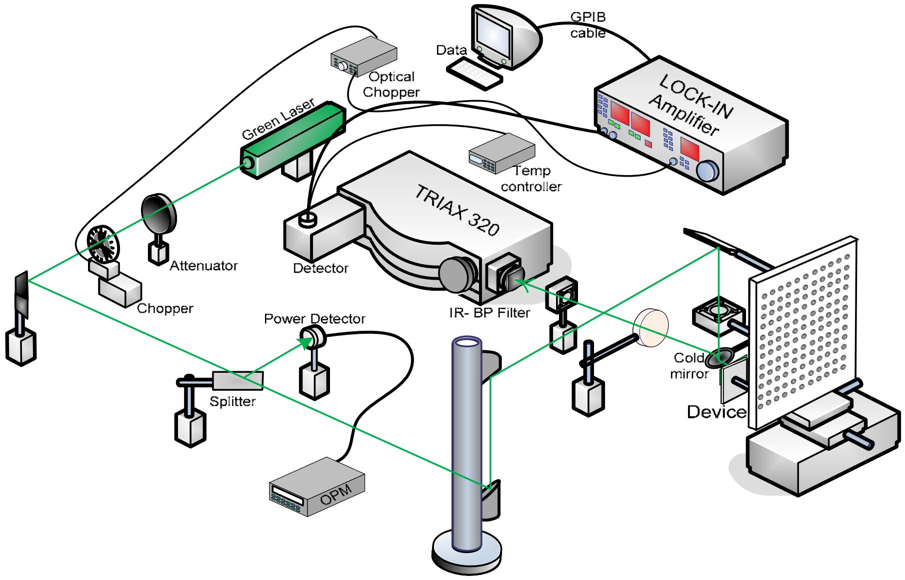

Figure 5.14 Schematic of photoluminescence (PL) Measurement setup for integrated MR-VCSEL. TRIAX320 spectrum meter and a 300mW green laser (533nm) light source are used.

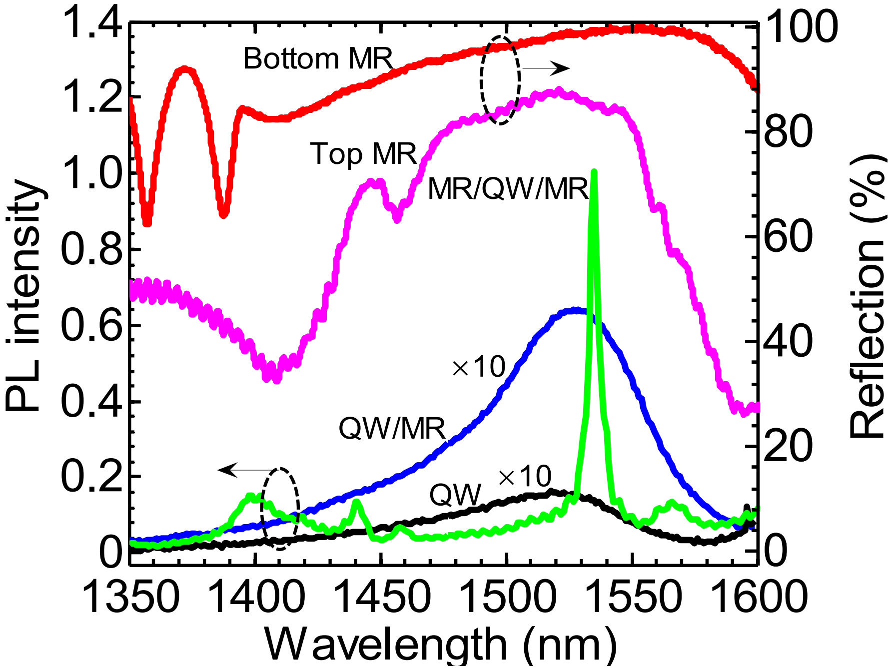

Figure 5.15 Photoluminescence (PL) Measurement of integrated MR-VCSEL over temperature (From 268 K to 290 K).

The figure 5.16 shows PL peak location (also cavity resonance mode) and line width changes at different temperatures (from 268 K to 290 K) for the MR-VCSEL device, the oscillating shift of the PL peak location is essentially due to change of the cavity length during the temperature varies

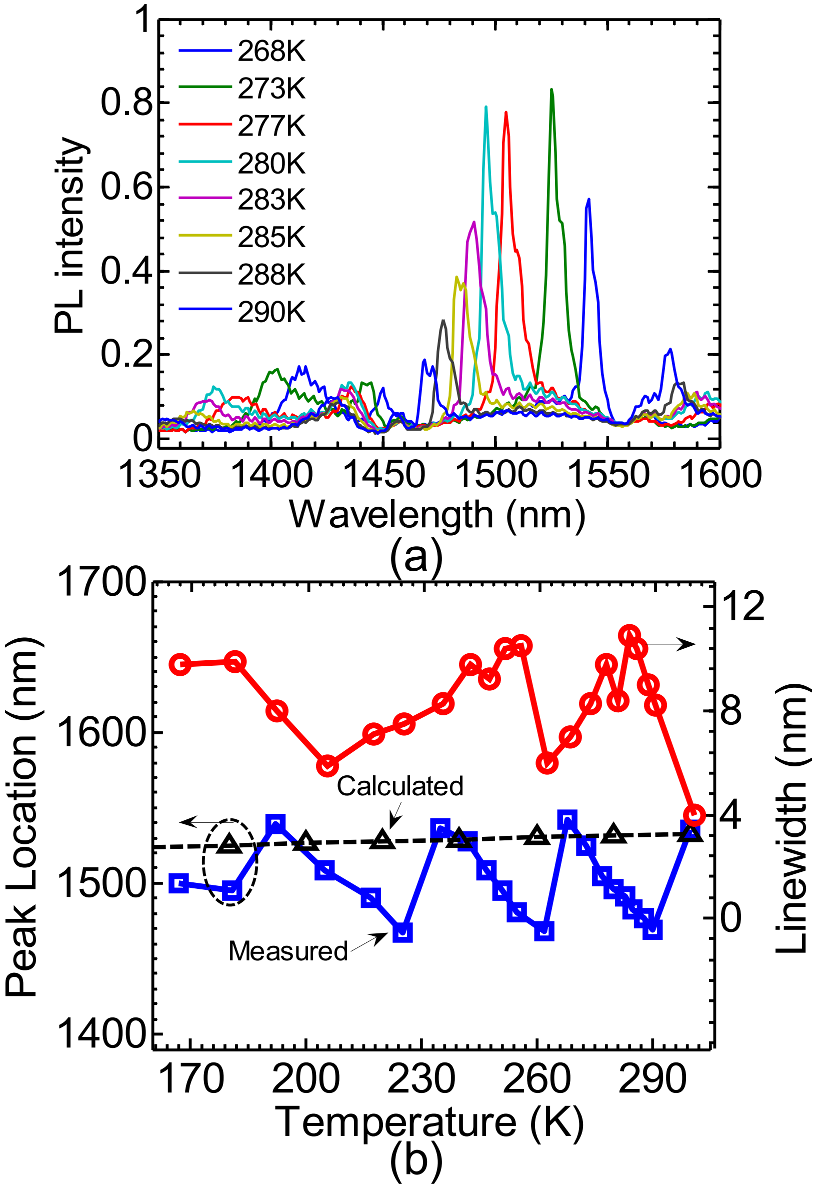

Figure 5.16 (a) Photoluminescence (PL) Measurement of integrated MR-VCSEL over temperature (From 268 K to 290 K); (b) Plots of Photoluminescence (PL) Peak Location (left) and Linewidth (right) over Temperature (From 268 K to 290 K) of integrated MR-VCSEL. Calculated cavity resonance λ is also plotted.

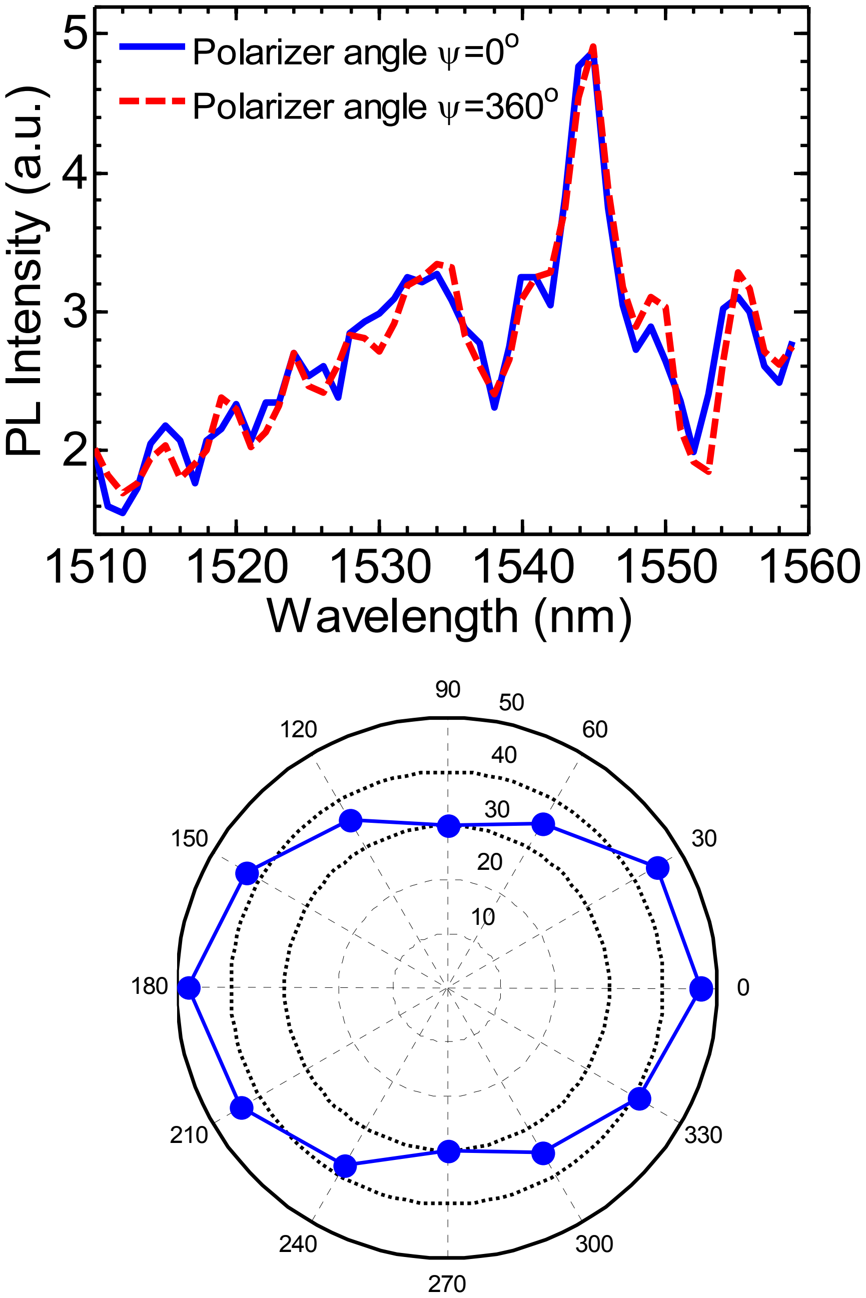

Figure 5.17 Measured Photoluminescence (PL) Peak values (at λ=1545nm) by setting the polarizer angle ψ from 0° to 360° at room temperature. The top figure shows the PL plots of start and end points.

The measured polarization dependence results at 1545 nm are showed in figure 5.17. A preferential polarization direction can be easily identified, but the output light is clearly not in one definite polarization state. By increasing the reflection of the top MR and improving the cavity performance, we can expect a better-defined polarized output.

5.4.2 InGaAsP QW LED Array on PET

The pulsed (1 ms width with 1% duty cycle) Current-Voltage (I-V) measurement was carried out on fabricated InGaAsP QW LED array devices which were further transferred on to PET plastic; one measured result is shown in figure 5.18, which shows a reasonable curve as expected.

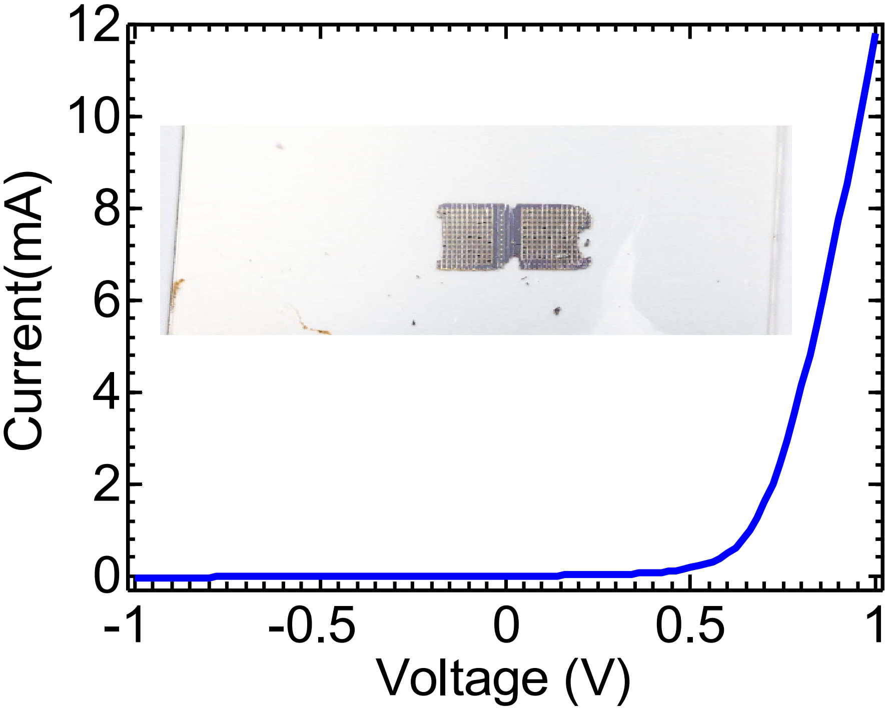

Figure 5.18 Measured Current-Voltage (I-V), insert is the InGaAsP QW LED array on PET under test.

The Light-Current (L-I) and spectral characteristics (OSA based setup shown in figure 5.19) of the InGaAsP QW LED array device were measured in the pulsed mode (1 ms width with 1% duty cycle) with lensed fiber coupling. The results are shown in figure 5.20 (a) and Figure 5.19 (b), respectively.

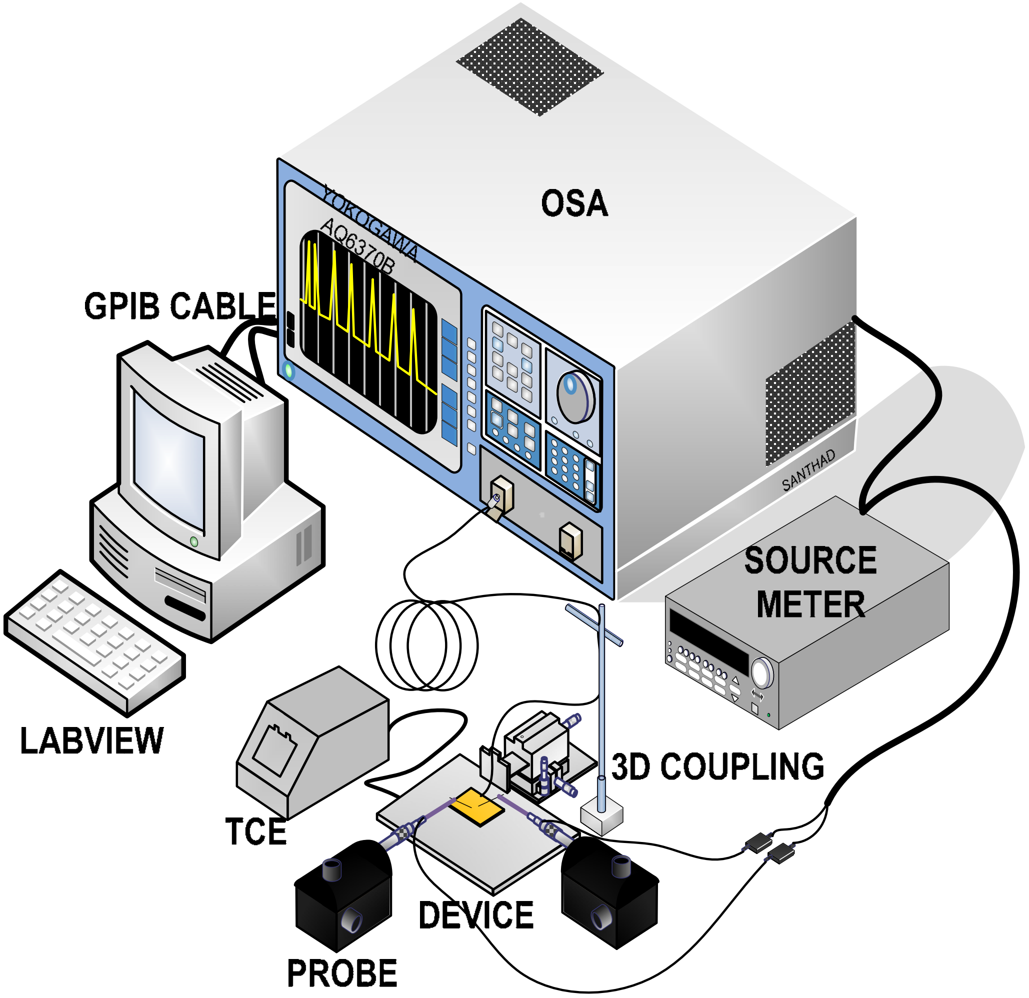

Figure 5.19 OSA based L-I setup with kiethley pulsed current source and lensed fiber.

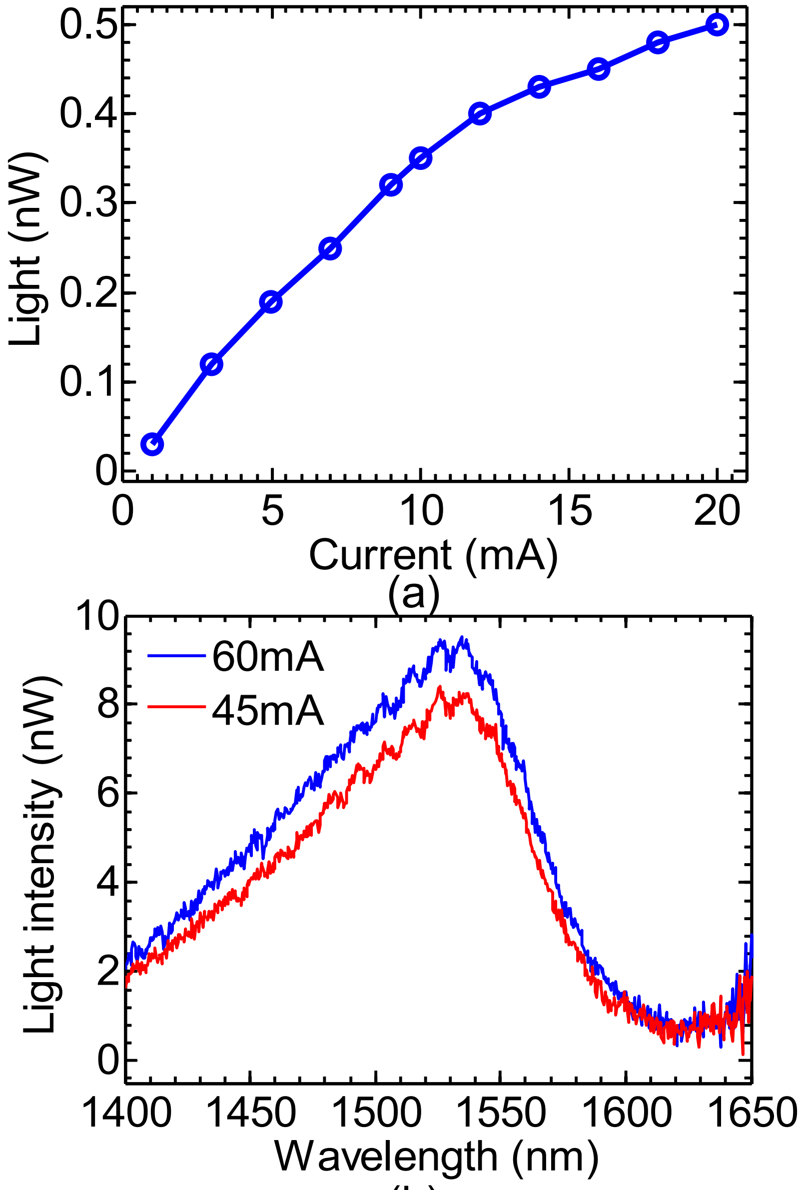

(a)

(b)

Figure 5.20 (a) Light-current characteristics of InGaAsP QW LED array device at 293 K; (b) Measured spectral outputs for injection current of 45 mA and 60 mA.

Finally, we also measured near-field images for the InGaAsP QW LED array for different biasing levels as shown in figure 5.21.

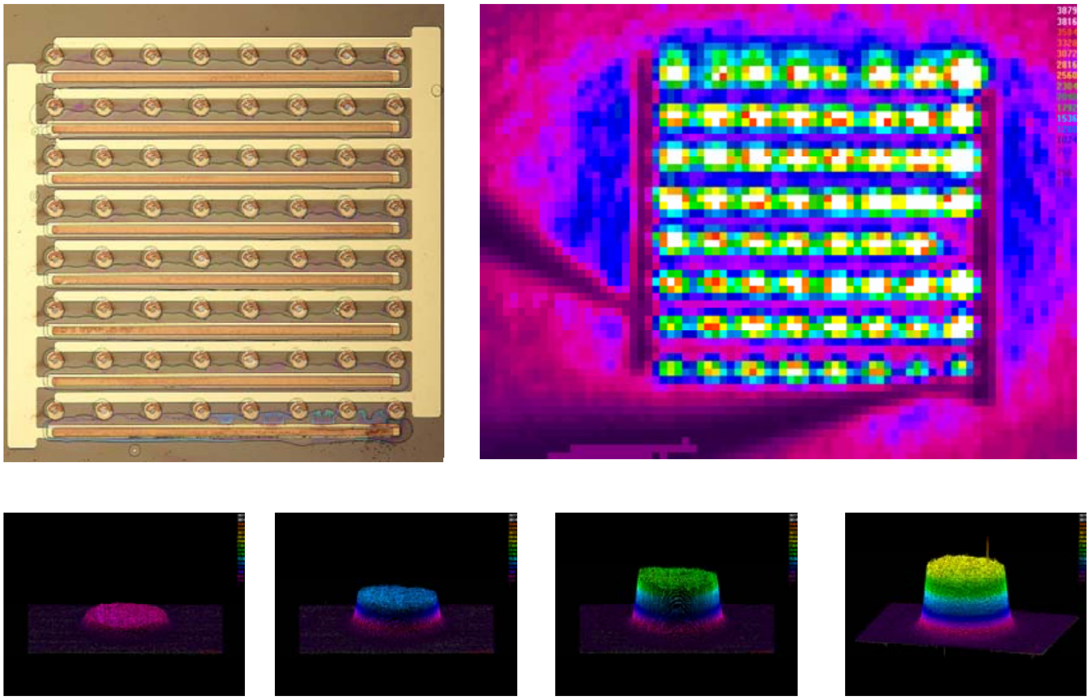

Figure 5.21 Near-field images for the InGaAsP QW LED array for different biasing levels.

5.5 Conclusions

In conclusion, RCLED device based on Si membrane reflectors (MR) have been demonstrated by optically pumping, with the feasibility of cavity modes control over a ~70nm range. Low temperature PL and Polarization characteristics have been demonstrated. The integration process of MR-VCSEL device is a challenging step, which involves very careful processing and alignment with photonic crystal patterned Si thin membrane.

More work is undergoing to improve the optically pumped device and to demonstrate electrically pumped MR-VCSEL.

CHAPTER 6

CONCLUSIONS AND FUTURE WORK

6.1 Research Summary

In this dissertation, different optoelectronic devices, based on photonic crystals, quantum dots/wells, and semiconductor nanomembranes, have been designed, fabricated and characterized. GaAs-based photonic crystal (PC) cavity quantum dot infrared photodetector (QDIP) with various cavity designs (in plane photonic crystal defect modes) and different operation spectra have been investigated. Si-based photonic crystal Fano-resonance filters for around 1550 nm with controlled cavity Q have been designed and made on SOI substrates and also have been successfully transferred onto foreign substrates such like on glass or on flexible plastics. Perfect Si membrane reflectors with nearly 100% reflection at designed wavelength range (bandwidth is up to 100 nm and 1550 nm is normal covered) have been realized on 340 nm thick SOI substrates, and the spectrally engineering has been achieved, theoretically and experimentally. The DBR free, so called ‘MR-VCSEL’ has been proposed and the MR cavity resonant emission have been measured with optically pumping. The optically pumped MR-VCSELs are constructed by Si-based membrane reflectors with an InGaAsP QW active layer in between, by a novel wet transfer technique. The spectra response and polarization characteristics have been performed; a 4 nm linewidth has been measured at 1545 nm. By further optimization of the transferred membrane reflectors, we can surely achieve single mode lasing with linewidth much less than 1 nm. The electrically pumped MR-VCSEL based on Si membrane reflectors has been also proposed; the MR cavities and quantum well gain structure have been simulated and demonstrated, and the integration of such device is undergoing.

6.1.1 GaAs-based Photonic Crystal (PC) Cavity with the Quantum Dot Infrared Photodetector (QDIP)

The GaAs-based quantum dot (InAs) in a well ($In_{0.15}Ga_{0.85}As$) infrared photodetectors with different photonic crystal cavity designs have been investigated. The quantum dot in a well heterostructures are designed and prepared via molecular beam epitaxy (MBE), and two n-i-n IR detector devices are fabricated based on such substrates. An enhanced absorption was observed in the single defect PC structures, with simultaneous absorption suppression observed in the photonic bandgap region. Dominant absorption occurs along the surface normal direction, similar the spontaneous emission process observed in photonic crystal surface-emitting lasers. The defect absorption properties remain largely the same for the coupled defect cavities, which is essential for large area infrared photodetector applications.

6.1.2 Si-based Fano-resonance Filters

An ultra-compact flexible 1550 nm optical filter with photonic crystal patterned Si thin film, which was transferred onto polyethylene terephthalate (PET) plastic, has been developed for the first time. By tuning the design parameters (lattice spacing a and air hole radius r) of the photonic crystal cavities, the selective spectrum has been achieved experimentally with very good agreement to our simulation. And the measured results also show that our Fano-resonance filters have desired angle/polarization sensitivities which agree well with the dispersion diagram. The feasibility of this technique is successfully demonstrated and such a spectrally-selective filter component can be used as the building blocks for a suite of flexible and vertically stacked ultra-compact high performance photonic devices, such as switches, modulators, and spectrally-selective photodetectors. The flexible integration schemes of stacked Si membranes can lead to simplified device fabrication processes for high performance flexible photonics and high density photonic integration systems.

6.1.3 Si-based Membrance Reflectors

An alternative high reflective semiconductor membrane mirror has been designed and fabricated with SOI substrates, the measured reflections are nearly 100% reflection over

50~100 nm in wavelength. Such spectrally-selective reflectors are realized with the controlled spectral locations based on the post-fabrication spectral processes. Spectral trimming was accomplished by partially removing the buried oxide layer (BOX) underneath the device layer, or by controlled SiO_2 film deposition on the top. Resonance tuning was demonstrated with a turning range over 50 nm for both blue- and red-shifts. This makes it feasible to engineer the desired working window in post-processes, and also releases the fabrication tolerance to a certain extent.

6.1.4 MR-VCSELs

A revolutionary 1550 nm Vertical Cavity Surface Emitting Laser (VCSEL) structure with single layer Si Membrane Reflector mirrors instead of conventional Distributed Bragg Reflectors (DBRs) has been proposed and developed both in optically pumping and in electrically pumping. The Si membrane reflectors provide efficient optical feedback over the wavelength and polarization of the emitted light. A 4 nm linewidth at 1545 nm was obtained experimentally under room temperature with a relatively low reflectivity of the transferred MR on glass, and output light has a reasonable polarization performance.

6.2 Suggestions for Future Work

6.2.1 High Performance Optical Modulators

Current research in photonic fields is to seek large scale, high efficiency optical integration and interconnects, more and more demand for high level optical commences such as light source, switch, filters and reflectors, etc. An instant application of our Fano-resonance Filter is flexible membrane modulators as shown in figure 6.1, which basically started with designing a proper p-i-n style Si membrane filter with a high cavity Q photonic crystal structure, and then embedded the membrane filter between two ITO-coated transparent PET plastic. By such stacking technique, we can achieve an ultra-compact, ultra-flexible thin film modulator, which will increase more practical capability in optoelectronic system integration and interconnection.

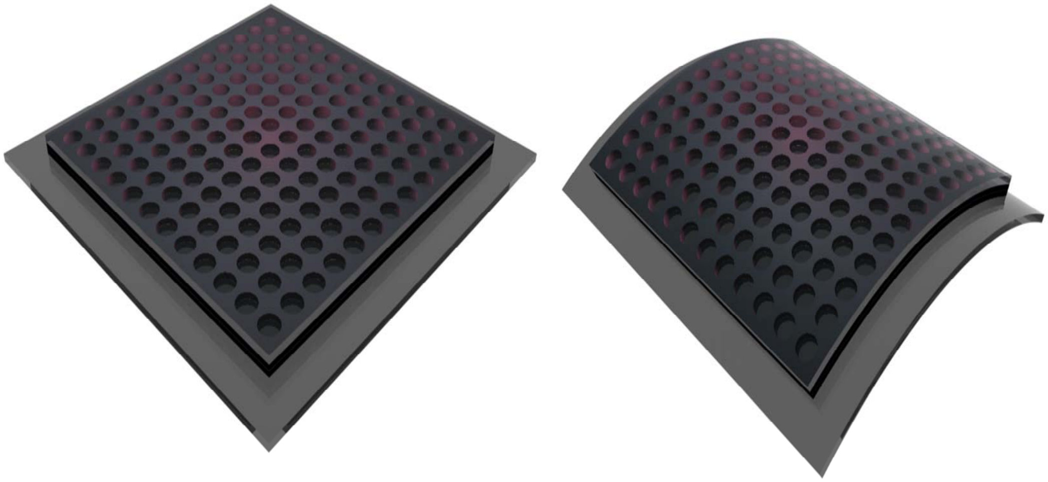

(a) (b)

Figure 6.1 (a) Schematic of Si Membrane Modulator embedded in ITO coated PET plastics and (b) Flexible Membrane Modulator.

6.2.2 Flexible Electrically Pumped MR-VCSEL

The ultimate objective of our Si membrane reflectors based VCSEL is to achieve electrically pumped lasing as shown in figure 6.2, which will dramatically reduce the VCSEL thickness without degradation of the laser performance. According to the achievements we have in Chapter 5, while we have obtained nearly 100% reflection for MR on SOI substrates, there is still room for improving the reflectivity of transferred MR mirrors; and meanwhile even the spontaneous emission factor of InGaAsP can be increased by optimizing heterostructure design, and by overcoming these issues and eliminating the experimental error in lithography and etching process, we will make it possible. Lastly, once we have MR-VCSEL, such devices are feasible to transfer to any foreign substrates like what we have done in Chapter 3.

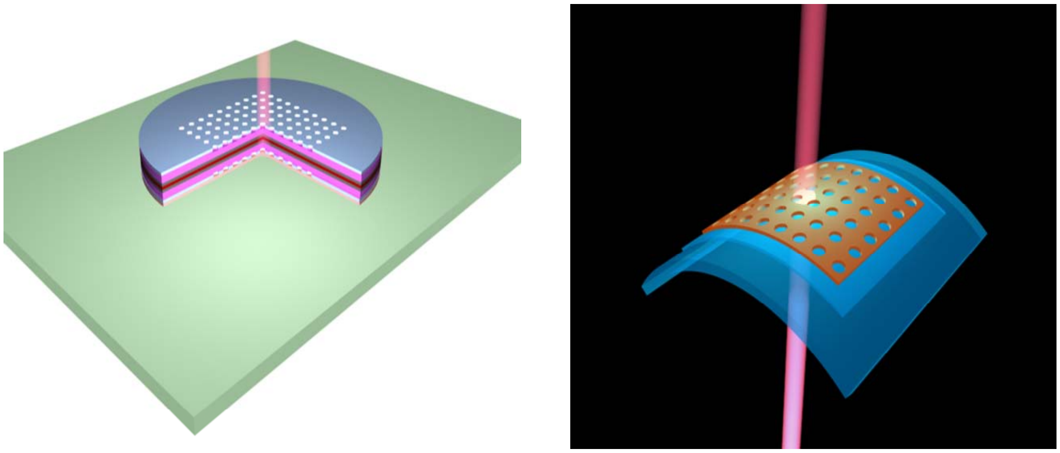

(a) (b)

Figure 6.2 (a) Schematic of electrically pumped MR-VCSEL transferred on glass and (b) Flexible MR-VCSEL.

6.3 Conclusion

Some novel spectrally selective optoelectronic devices have been developed and investigated in this dissertation work. Nonetheless the challenge of researching in smaller, faster and more efficient devices continues. Pursuing the Endless Frontier is my model role!

APPENDIX A

ABBREVIATIONS

IR	Infrared
QWIPs, QDIPs	Quantum well and quantum dot based IR photodetectors
PCs	Photonic crystals
PBG	Photonic bandgap
PCS	Photonic crystal slab
FDTD	Finite-difference time-domain
RCWA	Rigorous coupled-wave analysis
QD	Quantum dot
QW	Quantum well
RIE	Reactive ion etching
SEM	Scanning electron microscope
TEM	Transmission electron microscope
AFM	Atomic force microscope
PL	Photoluminescence
VCSELs	Vertical cavity surface emitting lasers
MRs	Membrane reflectors
DBRs	Distributed bragg reflectors
GMR	Guided mode resonance
PML	Perfectly matched layers
PBC	Periodic boundary condition
NMs	Nanomembranes
PET	Polyethylene terephthalate
BOX	Buried oxide
SOI	Silicon-on-insulator
SOG	Spin-on-glass
Q	Quality factor

SWG	Sub-wavelength grating
OSA	Optical spectrum analyzer
MBE	Molecular beam epitaxy

APPENDIX B

PUBLICATIONS

Journal papers

[1] W. Yang, **Hongjun Yang**, Guoxuan Qin, Zhenqiang Ma, Jesper Berggren, Mattias Hammar, Richard Soref, Weidong Zhou, "Large-area InP-based crystalline nanomembrane flexible photodetectors," *Applied Physics Letters,* vol. 96, p. 3, 2010.

[2] L. Chen, **Hongjun Yang**, Z. Qiang, H. Pang, L. Sun, Z. Ma, R. Pate, A. Stiff-Roberts, S. Gao, and J. Xu, "Colloidal quantum dot absorption enhancement in flexible Fano filters," *Applied Physics Letters,* vol. 96, p. 083111, 2010.

[3] W. Zhou, Z. Ma, **Hongjun Yang**, Z. Qiang, G. Qin, H. Pang, L. Chen, W. Yang, S. Chuwongin, and D. Zhao, "Flexible photonic-crystal Fano filters based on transferred semiconductor nanomembranes," *Journal of Physics D: Applied Physics,* vol. 42, pp. 234007-234017, 2009.

[4] **Hongjun Yang**, S. Chuwongin, Z. Qiang, L. Chen, H. Pang, Z. Ma, and W. Zhou, "Resonance control of membrane reflectors with effective index engineering," *Applied Physics Letters,* vol. 95, p. 023110, 2009.

[5] L. Chen, Z. Qiang, **Hongjun Yang**, H. Pang, Z. Ma, and W. D. Zhou, "Polarization and angular dependent transmissions on transferred nanomembrane Fano filters," *Optics Express,* vol. 17, pp. 8396-8406, 2009.

[6] Y. Wang, L. Chen, **H. Yang**, Q. Guo, W. D. Zhou, and M. Tao, "Hemispherical Antireflection Coatings by Large-Area Convective Assembly of Monolayer Silica Microspheres", *Solar Energy Materials & Solar Cells, vol. 93, 85-91,*

doi:10.1016/j.solmat.2008.08.008

[7] **Hongjun Yang**, Z. Qiang, H. Pang, Z. Ma, and W. D. Zhou, "Surface-Normal Fano Filters Based on Transferred Silicon Nanomembranes on Glass Substrates," *Electronics Letters,* vol. 44, pp. 858-9, 2008.

[8] Z. Qiang, **Hongjun Yang,** L. Chen, H. Pang, Z. Ma, and W. Zhou, "Fano filter modal analysis based on transferred silicon nanomembranes on flexible substrates," *Appl. Phys. Lett.,* vol. 93, p. 061106, 2008.

[9] W. Zhou, M. Tao, L. Chen, and **Hongjun Yang**, "Microstructured surface design for omnidirectional antireflection coatings on solar cells," *Journal of Applied Physics,* vol. 102, p. 103105, 2007.

[10] M. Tao, W. Zhou, **Hongjun Yang**, and L. Chen, "Surface texturing by solution deposition for omnidirectional antireflection," *Applied Physics Letters,* vol. 91, p. 081118, 2007.

Conference proceedings and presentations

[11] L. Chen, **Hongjun Yang**, Z. Qiang, L. Sun, Z. Ma, R.Pate, A. Stiff-Roberts, J. Xu, G. J. Brown, and W. D. Zhou, “Direct measurement of spectrally selective absorption enhancement in Fano resonance photonic crystal cavities on plastic substrates”, Proc. SPIE, vol. 2010.

[12] L. Chen, **Hongjun Yang**, Z. Qiang, H. Pang, Z. Ma, J. Xu, G. J. Brown, and W. D.

Zhou, "Angle and Polarization Dependent Characteristics of Colloidal Quantum Dot Absorption in Fano Filters on Flexible Substrates", Proc. SPIE, vol.7222, 72220V, 2009.

[13] W. D. Zhou, **Hongjun Yang**, Z. Qiang, L. Chen, and G. J. Brown, "Spectrally Selective Infrared Absorption Enhancement in Photonic Crystal Cavities (Invited)", Proc. SPIE, vol.7095, 709507, 2008.

[14] Z. Qiang, L. Chen, **Hongjun Yang**, H. Pang, Z. Ma, and W. D. Zhou, "Fano filter modal analysis based on transferred silicon nanomembranes on flexible substrates", Proc. SPIE, vol. 7031, 703109, 2008.

[15] L. Chen, **Hongjun Yang**, M. Tao, and W. D. Zhou "Microstructured anti-reflection surface design for the omni-directional solar cells", Proc. SPIE, vol. 7046, 704608, 2008.

[16] W. D. Zhou, **Hongjun Yang**, Z. Qiang, L. Chen, and G. J. Brown, "Spectrally Selective Infrared Absorption Enhancement in Photonic Crystal Cavities (Invited)", SPIE Annual Meeting, San Diego, CA, USA, Aug. 10-14, 2008.

[17] W. D. Zhou, **Hongjun Yang**, L. Chen, Z. Qiang, A. D. Stiff-Roberts, G. J. Brown, "Photonic crystals for spectrally selective infrared photonics (Invited)", The 6th Asia-Pacific Conference on Near-Field Optics, Yellow Mountain, China, June 13-17, 2007.

[18] **Hongjun Yang**, L. Chen, Z. X. Qiang, M. Lu, W.D. Zhou, G. J. Brown, A. Stiff-Roberts, S. Krishna, "Photonic Crystal Infrared Photodetector Design and Fabrication (Invited)", Texas SRPING Conference IV, Feb. 6-7, 2007.

[19] W. D. Zhou, L. Chen, G. Thiruvengadam, **Hongjun Yang**, " Novel photonic crystal structures for active nanophotonic devices (Invited)", ETIC'06, Aug. 10-12, 2006, Richardson, TX.

[20] L. Chen, **Hongjun Yang**, Z. Qiang, L. Sun, Z. Ma, R.Pate, A. Stiff-Roberts, J. Xu, G. J. Brown, and W. D. Zhou, "Direct measurement of spectrally selective absorption enhancement in Fano resonance photonic crystal cavities on plastic substrates", Photonics West 2010, Jan. 23-28, 2010, San Francisco, CA.

[21] W. Yang, **Hongjun Yang**, G. Qin, G. Pang, J. Berggren, M. Hammar, R. Soref, Z. Ma, and W. D. Zhou, "Crystalline Silicon Nanomembrane Stacking for Large-Area Flexible Photodetectors", IEEE 6th 6th International Conference on Group IV Photonics, September 9-11, 2009, San Francisco, CA.

[22] L. Chen, **Hongjun Yang**, Z. Qiang, H. Pang, Z. Ma, J. Xu, G. J. Brown, and W. D. Zhou, "Angle and Polarization Dependent Characteristics of Colloidal Quantum Dot Absorption in Fano Filters on Flexible Substrates", Photonics West, Jan.24-29, 2009, San Jose, CA.

[23] Y. Wang, L. Chen, **Hongjun Yang**, Q. Guo, W. D. Zhou, and M. Tao, "Large-Area Convective Assembly for Solution Processed Omni-Directional Antireflection Coatings", MRS Fall Meeting, Dec. 1-5, 2008, Boston, MA.

[24] Y. Wang, L. Chen, **Hongjun Yang**, Q. Guo, W. D. Zhou, and M. Tao, "Anti-Reflection and High-Reflection Optical Thin Films Based on Dip Coating of Inorganic Particles",

MRS Fall Meeting, Dec. 2008, Boston, MA.

[25] **Hongjun Yang**, S. Chuwongin, L. Chen, Z. Qiang, W. D. Zhou, H. Pang, and Z. Ma, “Spectral Trimming of Fano Reflectors on Silicon and Glass Substrates”, IEEE LEOS Annual Meeting, Long Beach, CA, Nov. 9-13, 2008.

[26] **Hongjun Yang**, L. Chen, Z. Qiang, H. Pang, Z. Ma, and W. D. Zhou, “Characteristics of Fano Filters Based on Transferred Silicon Nanomembranes on Glass and Plastic Substrates”, 2008 Asia Optical Fiber Communication & Optoelectronic Exposition & Conference (AOE’08), Shanghai, China, Oct. 30-Nov. 2, 2008. (Best student paper finalist)

[27] Z. Qiang, **Hongjun Yang**, L. Chen, H. Pang, Z. Ma, W. D. Zhou, and G. J. Brown, “Characteristics of Surface-Normal Fano Filters on Plastic Substrates”, IEEE Nano 2008, Aug. 18-21, 2008, Arlington, TX.

[28] Y. Wang, **Hongjun Yang**, L. Chen, W. D. Zhou, M. Tao and Q. Guo, “Solution Processed Large Area Surface Textures Based on Dip Coating”, IEEE Nano 2008, Aug. 18-21, 2008, Arlington, TX.

[29] **Hongjun Yang**, Z. Qiang, L. Chen, H. Pang, Z. Ma, and W. D. Zhou, “Surface-Normal Fano Filters and Broadband Reflectors Based on Transferred Silicon Nanomembranes on Glass Substrates”, IEEE Nano 2008, Aug. 18-21, 2008, Arlington, TX.

[30] L. Chen, **Hongjun Yang**, M. Tao, and W. D. Zhou “Microstructured anti-reflection surface design for the omni-directional solar cells”, SPIE Annual Meeting, San Diego,

CA Aug. 10-14, 2008.

[31] Z. Qiang, L. Chen, **Hongjun Yang**, H. Pang, Z. Ma, and W. D. Zhou, “Fano filter modal analysis based on transferred silicon nanomembranes on flexible substrates”, SPIE Annual Meeting, San Diego, CA Aug. 10-14, 2008.

[32] **Hongjun Yang**, Z. Qiang, H. Pang, Z. Ma, W. D. Zhou, M. Lu, and R. A. Soref, “Surface-Normal Fano Filters Based on Transferred Silicon Nanomembranes on Glass Substrates”, CLEO’08, San Jose, CA.

[33] M. Tao, W. D. Zhou, **Hongjun Yang**, Y. Wang, and Q. Guo, “A Universal Surface Texture by Solution coating”, 33rd IEEE Photovoltaic Specialists Conference, May 11-16, 2008, San Diego, CA.

[34] W.D. Zhou, **Hongjun Yang**, L. Chen, Z. Qiang, W. Zhang, A. Stiff-Roberts, S. Krishna, G. J. Brown, “Characteristics of Photonic Crystal Quantum Dot Infrared Photodetectors”, NSF CMMI Engineering Research and Innovation Conference, Knoxville, TN, Jan. 7-10, 2008.

[35] M. Tao, W. D. Zhou, **Hongjun Yang**, K. Han, “A solution-prepared surface texture for solar cells”, 17th International Photovoltaic Science and Engineering Conference (PVSEC-17), Fukuoka, Japan, December 3-7, 2007.

[36] **Hongjun Yang**, L. Chen, Z. Qiang, W. D. Zhou, W. Zhang, A. D. Stiff-Roberts, S. Krishna, G. J. Brown, “Characteristics of photonic crystal cavity based infrared photodetectors”, IEEE LEOS Annual Meeting, Oct. 17-21, 2007.

[37] **Hongjun Yang**, L. Chen, Z.X. Qiang, W. D. Zhou, “Photonic Crystal Infrared Photodetector Design and Fabrication”, The Best Little Nano Conference in Texas, April 4-5, 2007, Austin, TX**.**

[38] W. D. Zhou, L. Chen, **Hongjun Yang**, Z.X. Qiang, “Photonic crystals for spectrally selective infrared silicon photonics”, Nano and Giga Challenges in Electronics and Photonics(Symposium and Spring School), March 12-16, 2007, Phoenix, Arizona.

[39] G. Thiruvengadam, **Hongjun Yang**, W. D. Zhou, “Encapsulated photonic crystals and nanoparticle self assemblyon patterned photonic crystal structures”, JSPS – UNT Joint Symposium on Nanoscale Materials for Optoelectronics and Biotechnology, Feb. 2-3, 2006, University of North Texas, Denton, Texas.

REFERENCES

[1] M. Florescu*, et al.*, "Thermal emission and absorption of radiation in finite inverted-opal photonic crystals," *Physical Review A,* vol. 72, p. 33821, 2005.

[2] G. Veronis*, et al.*, "Metallic photonic crystals with strong broadband absorption at optical frequencies over wide angular range," *Journal of Applied Physics,* vol. 97, pp. 93104-93104, 2005.

[3] S. Fan and J. D. Joannopoulos, "Analysis of guided resonances in photonic crystal slabs," *Physical Review B,* vol. 65, p. 235112, 2002.

[4] H. Yang*, et al.*, "Surface-normal Fano filters based on transferred silicon nanomembranes on glass substrates," *Electron. Lett.,* vol. 44, p. 858, 2008.

[5] E. Yablonovitch*, et al.*, "Photonic band structure: The face-centered-cubic case employing nonspherical atoms," *Physical Review Letters,* vol. 67, pp. 2295-2298, 1991.

[6] T. Krauss*, et al.*, "Two-dimensional photonic-bandgap structures operating at near-infrared wavelengths," *Nature,* vol. 383, pp. 699-702, 1996.

[7] E. Yablonovitch, "Inhibited spontaneous emission in solid-state physics and electronics," *Physical Review Letters,* vol. 58, pp. 2059-2062, 05/18/ 1987.

[8] M. Fujita*, et al.*, "Simultaneous inhibition and redistribution of spontaneous light emission in photonic crystals," *Science,* vol. 308, pp. 1296-1298, 05/27/ 2005.

[9] S. G. Johnson*, et al.*, "Guided modes in photonic crystal slabs," *Physical Review B (Condensed Matter),* vol. 60, pp. 5751-5758, 08/15/ 1999.

[10] O. Painter*, et al.*, "Two-dimensional photonic band-gap defect mode laser," *Science,* vol. 284, pp. 1819-1821, 06/11/ 1999.

[11] J. K. Hwang*, et al.*, "Continuous room-temperature operation of optically pumped two-dimensional photonic crystal lasers at 1.6 um," *IEEE Photonics Technology Letters,* vol. 12, pp. 1295-1297, 10// 2000.

[12] W. D. Zhou*, et al.*, "Characteristics of a photonic bandgap single defect microcavityelectroluminescent device," *IEEE Journal of Quantum Electronics* vol. 37, pp. 1153-1160, 2001.

[13] R. Colombelli*, et al.*, "Quantum Cascade Surface-Emitting Photonic Crystal Laser," *Science,* vol. 302, pp. 1374-7, 2003.

[14] H. G. Park*, et al.*, "Electrically Driven Single-Cell Photonic Crystal Laser," *Science,* vol. 305, pp. 1444-7, 2004.

[15] H. Altug and J. Vuckovic, "Photonic crystal nanocavity array laser," *Optics Express,* vol. 13, pp. 8819-8828, 2005.

[16] S. Y. Lin*, et al.*, "Origin of absorption enhancement in a tungsten, three-dimensional photonic crystal," *Journal of the Optical Society of America B (Optical Physics),* vol. 20, pp. 1538-41, 2003.

[17] S. Noda and T. Baba, *Roadmap on Photonic Crystals* Springer, 2003.

[18] Y. Xi*, et al.*, "Modification of absorption of a bulk material by photonic crystals," *Chinese Physics Letters,* vol. 19, pp. 1819-21, 2002.

[19] J. Yu*, et al.*, "Absorption in one-dimensional metallic-dielectric photonic crystals," *Journal of Physics: Condensed Matter,* vol. 16, pp. L51-56, 2004.

[20] K. T. Posani*, et al.*, "Nanoscale quantum dot infrared sensors with photonic crystal cavity," *Applied Physics Letters,* vol. 88, p. 151104, 2006.

[21] B. Temelkuran*, et al.*, "Resonant cavity enhanced detectors embedded in photonic crystals," *Applied Physics Letters,* vol. 72, p. 2376, 1998.

[22] J. G. Fleming*, et al.*, "All-metallic three-dimensional photonic crystals with a large infrared bandgap," *Nature,* vol. 417, pp. 52-55, 2002.

[23] S. Y. Lin*, et al.*, "Three-dimensional photonic-crystal emitter for thermal photovoltaic power generation," *Applied Physics Letters,* vol. 83, pp. 380-382, 2003.

[24] M. S. Unlu and S. Strite, "Resonant cavity enhanced photonic devices," *Journal of Applied Physics,* vol. 78, pp. 607-639, 1995.

[25] P. Bhattacharya*, et al.*, "Quantum dot opto-electronic devices," *Annu. Rev. Mater. Res.,* vol. 34, pp. 1-40, 2004.

[26] O. Painter*, et al.*, "Lithographic tuning of a two-dimensional photonic crystal laser array," *IEEE Photonics Technology Letters,* vol. 12, pp. 1126-1128, 09// 2000.

[27] J. B. Pendry and A. MacKinnon, "Calculation of photon dispersion relations," *Physical Review Letters,* vol. 69, pp. 2772-2775, 1992.

[28] A. Taflove and S. C. Hagness, *Computational Electrodynamics: The Finite-difference Time-domain Method*: Artech House, 2000.

[29] S. G. Johnson*, et al.*, "Guided modes in photonic crystal slabs," *Physical Review B,* vol. 60, pp. 5751-5758, 1999.

[30] Z. Qiang*, et al.*, "Optical add-drop filters based on photonic crystal ring resonators," *Optics Express,* vol. 15, pp. 1823-1831, 2007.

[31] U. Fano, "Effects of Configuration Interaction on Intensities and Phase Shifts," *Physical Review,* vol. 124, p. 1866, 1961.

[32] R. Magnusson and S. S. Wang, "New principle for optical filters," *Applied Physics Letters,* vol. 61, p. 1022, 1992.

[33] S. T. Thurman and G. M. Morris, "Controlling the spectral response in guided-mode resonance filter design," *Appl. Opt,* vol. 42, pp. 3225-3233, 2003.

[34] A. Rosenberg*, et al.*, "Guided resonances in asymmetrical GaN photonic crystal slabs observed in the visible spectrum," *Optics Express,* vol. 13, pp. 6564-6571, 2005.

[35] W. Suh, "Displacement-sensitive photonic crystal structures based on guided resonance in photonic crystal slabs," *Applied Physics Letters,* vol. 82, p. 1999, 2003.

[36] Y. Kanamori*, et al.*, "Control of guided resonance in a photonic crystal slab using microelectromechanical actuators," *Applied Physics Letters,* vol. 90, p. 031911, 2007.

[37] K. B. Crozier*, et al.*, "Air-bridged photonic crystal slabs at visible and near-infrared wavelengths," *Physical Review B,* vol. 73, p. 115126, 2006.

[38] C. Grillet*, et al.*, "Characterization and modeling of Fano resonances in chalcogenide photonic crystal membranes," *Optics Express,* vol. 14, pp. 369-376, 2006.

[39] L. Zhou and A. W. Poon, "Fano resonance-based electrically reconfigurable add-drop filters in silicon microring resonator-coupled Mach-Zehnder interferometers," *Optics Letters,* vol. 32, pp. 781-783, 2007.

[40] S. Fan, "Sharp asymmetric line shapes in side-coupled waveguide-cavity systems," *Applied Physics Letters,* vol. 80, p. 908, 2002.

[41] L. Y. Mario*, et al.*, "Asymmetric Fano resonance and bistability for high extinction ratio, large modulation depth, and low power switching," *Optics Express,* vol. 14, pp. 12770-12781, 2006.

[42] C. Y. Chao, "Biochemical sensors based on polymer microrings with sharp asymmetrical resonance," *Applied Physics Letters,* vol. 83, p. 1527, 2003.

[43] W. Suh*, et al.*, "Displacement sensing using evanescent tunneling between guided resonances in photonic crystal slabs," *Journal of Applied Physics,* vol. 98, p. 033102, 2005.

[44] D. L. C. Chan*, et al.*, "Emulating one-dimensional resonant Q-matching behavior in a two-dimensional system via Fano resonances," *Physical Review A,* vol. 74, p. 64901, 2006.

[45] V. Lousse*, et al.*, "Angular and polarization properties of a photonic crystal slab mirror," *Optics Express,* vol. 12, pp. 1575-1582, 2004.

[46] S. Boutami*, et al.*, "Broadband and compact 2-D photonic crystal reflectors with controllable polarization dependence," *Photonics Technology Letters, IEEE,* vol. 18, pp. 835-837, 2006.

[47] B. B. Bakir*, et al.*, "Surface-emitting microlaser combining two-dimensional photonic crystal membrane and vertical Bragg mirror," *Applied Physics Letters,* vol. 88, p. 081113, 2006.

[48] A. M. Yacomotti*, et al.*, "All-optical bistable band-edge Bloch modes in a two-dimensional photonic crystal," *Applied Physics Letters,* vol. 88, p. 231107, 2006.

[49] M. F. Yanik and S. Fan, "Stopping and storing light coherently," *Physical Review A,* vol. 71, p. 13803, 2005.

[50] Z. Qiang*, et al.*, "Fano filters based on transferred silicon nanomembranes on plastic substrates," *Applied Physics Letters,* vol. 92, p. In press, 2008.

[51] A. Krier, *Mid-infrared semiconductor optoelectronics*: Springer, 2006.

[52] E. Yablonovitch, "Photonic band-gap structures," *Journal of the optical society of America B,* vol. 10, pp. 283-295, 1993.

[53] O. Painter*, et al.*, "Two-dimensional photonic band-gap defect mode laser," *Science,* vol. 284, p. 1819, 1999.

[54] W. Zhou*, et al.*, "Characteristics of a photonic bandgap single defect microcavityelectroluminescent device," *IEEE Journal of Quantum Electronics,* vol. 37, pp. 1153-1160, 2001.

[55] M. Fujita*, et al.*, "Simultaneous inhibition and redistribution of spontaneous light emission in photonic crystals," *Science,* vol. 308, p. 1296, 2005.

[56] S. Lin*, et al.*, "Three-dimensional photonic-crystal emitter for thermal photovoltaic power generation," *Applied Physics Letters,* vol. 83, p. 380, 2003.

[57] J. Fleming*, et al.*, "All-metallic three-dimensional photonic crystals with a large infrared bandgap," *Nature,* vol. 417, pp. 52-55, 2002.

[58] G. Von Freymann*, et al.*, "NT étreault, S. Wong, V. Kitaev, and GA Ozin,"Tungsten inverse opals: The influence of absorption on the photonic band structure in the visible spectral region,"" *Appl. Phys. Lett,* vol. 84, p. 224, 2004.

[59] G. Veronis*, et al.*, "Metallic photonic crystals with strong broadband absorption at optical frequencies over wide angular range," *Journal of Applied Physics,* vol. 97, p. 093104, 2005.

[60] A. Stiff*, et al.*, "Normal-incidence, high-temperature, mid-infrared, InAs-GaAs vertical quantum-dot infrared photodetector," *IEEE Journal of Quantum Electronics,* vol. 37, pp. 1412-1419, 2001.

[61] S. Krishna, "Quantum dots-in-a-well infrared photodetectors," *Journal of Physics D: Applied Physics,* vol. 38, 2005.

[62] S. Gunapala*, et al.*, "Demonstration of 640× 512 pixels long-wavelength infrared (LWIR) quantum dot infrared photodetector (QDIP) focal plane array (Proceedings Paper)," 2007, p. 15.

[63] R. Magnusson and S. S.Wang, "New principle for optical filters," *Appl. Phys. Lett.,* vol. 61, pp. 1022-1024, 1992.

[64] V. Lousse*, et al.*, "Angular and polarization properties of a photonic crystal slab mirror," *Opt. Express,* vol. **12** pp. 1575-1582 2004.

[65] J. Rogers*, et al.*, "Paper-like electronic displays: Large-area rubber-stamped plastic sheets of electronics and microencapsulated electrophoretic inks," *Proceedings of the National Academy of Sciences,* vol. 98, pp. 4835-4840, 2001.

[66] O. G. Schmidt and K. Eberl, "Nanotechnology: Thin solid films roll up into nanotubes," *Nature,* vol. 410, p. 168, 2001.

[67] H. C. Yuan*, et al.*, "High-speed strained-single-crystal-silicon thin-film transistors on flexible polymers," *Journal of Applied Physics,* vol. 100, p. 013708, 2006.

[68] S. A. Scott and M. G. Lagally, "Elastically strain-sharing nanomembranes: flexible and transferable strained silicon and silicon-germanium alloys," *J. Phys. D.,* vol. **40**, pp. R75-R92, 2007.

[69] H. C. Yuan*, et al.*, "7.8-GHz flexible thin-film transistors on a low-temperature plastic substrate," *Journal of Applied Physics,* vol. 102, p. 034501, 2007.

[70] Z. Qiang*, et al.*, "Fano filter modal analysis based on transferred silicon nanomembranes on flexible substrates," *Appl. Phys. Lett.,* vol. 93, p. 061106, 2008.

[71] Z. Qiang*, et al.*, "Fano filter modal analysis based on transferred silicon nanomembranes on flexible substrates," *Appl. Phys. Lett,* vol. 93, p. 061106, 2008.

[72] R. Magnusson and M. Shokooh-Saremi, "Physical basis for wideband resonant reflectors," *Optics Express,* vol. 16, pp. 3456-3462, 2008.

[73] C. F. R. Mateus*, et al.*, "Broadband mirror (1.12-1.62 μm) using single-layer sub-wavelength grating," *IEEE Photon. Technol. Lett,* vol. 16, pp. 1676-1678, 2004.

[74] M. C. Y. Huang*, et al.*, "A surface-emitting laser incorporating a high-index-contrast subwavelength grating," *Nature Photonics,* vol. 119-22, p. 11, 2007.

[75] S. Boutami*, et al.*, "Compact 1.55 μm room-temperature optically pumped VCSEL using photonic crystal mirror," *Electronics Letters,* vol. 43, p. 282, 2007.

[76] A. Rosenberg*, et al.*, "Guided resonances in asymmetrical GaN photonic crystal slabs observed in the visible spectrum," *Opt. Express,* vol. **13** pp. 6564-6571 2005.

[77] C. Lin*, et al.*, "Experimentally demonstrated filters based on guided resonance of photonic-crystal films," *Appl. Phys. Lett.,* vol. 87, p. 091102, 2005.

[78] W. Suh and S. Fan, "All-pass transmission or flattop reflection filters using a single photonic crystal slab," *Appl. Phys. Lett.,* vol. 84, p. 4905, 2004.

[79] S. Boutami*, et al.*, "Broadband and compact 2-D photonic crystal reflectors with controllable polarization dependence," *Photonics Technology Letters, IEEE,* vol. 18, pp. 835-837, 2006.

[80] H. Yang*, et al.*, "Spectral trimming of fano reflectors on silicon and glass substrates," presented at the IEEE LEOS Annual Meeting, 2008.

[81] H. Yang*, et al.*, "Surface-Normal Fano Filters Based on Transferred Silicon Nanomembranes on Glass Substrates," *Electronics Letters,* vol. 44, pp. 858-9, 2008.

[82] H.-C. Yuan*, et al.*, "7.8-GHz flexible thin-film transistors on a low-temperature plastic substrate," *J. Appl. Phys.,* vol. **102**, p. 034501, 2007.

[83] L. Chen*, et al.*, "Polarization and angular dependent transmissions on transferred nanomembrane Fano filters," *Optics Express,* vol. 17, pp. 8396-8406, 2009.

[84] Z. Qiang*, et al.*, "Fano Resonance Enhanced Infrared Absorption for Infrared Photodetectors," *Proceedings of SPIE,* vol. 6901, p. 69010F, 2008.

[85] H. Yang*, et al.*, "Resonance control of membrane reflectors with effective index engineering," *Applied Physics Letters,* vol. 95, p. 023110, 2009.

[86] H. Soda*, et al.*, "GaInAsP/InP surface emitting injection lasers," *Jpn. J. Appl. Phys,* vol. 18, pp. 2329–2330, 1979.

[87] N. Niskiyama*, et al.*, "Highly strained GaInAs-GaAs quantum-well vertical-cavitysurface-emitting laser on GaAs (311) B substrate for stable polarizationoperation," *IEEE Journal of Selected Topics in Quantum Electronics,* vol. 7, pp. 242-248, 2001.

[88] P. Sundgren*, et al.*, "High-performance 1.3/spl mu/m InGaAs vertical cavity surface emitting lasers," *Electronics Letters,* vol. 39, pp. 1128-1129, 2003.

[89] S. Blokhin*, et al.*, "Vertical-cavity surface-emitting lasers based on submonolayer InGaAs quantum dots," *IEEE Journal of Quantum Electronics,* vol. 42, pp. 851-858, 2006.

[90] A. Filios*, et al.*, "Transmission performance of a 1.5-mm 2.5-Gb/s directly modulated tunable VCSEL," *IEEE Photonics Tech. Lett,* vol. 15, p. 599, 2003.

[91] X. Zhao*, et al.*, "Room-temperature tunable ultraslow light in 1550 nm VCSEL amplifier," 2005.

[92] P. Dowd*, et al.*, "Long wavelength GaAsP/GaAs/GaAsSb VCSELs on GaAs substrates for communications applications," *Electronics Letters,* vol. 39, pp. 987-988, 2003.

[93] A. Mereuta*, et al.*, "1.5 [mu] m VCSEL structure optimization for high-power and high-temperature operation," *Journal of Crystal Growth,* vol. 272, pp. 520-525, 2004.

[94] E. Goobar, C. Mahon, F. H. Peters, M. G. Peters, and L. A. Coldren, "Low-temperature operation of vertical cavity surface-emitting lasers," *IEEE Photonics Technology Letters,* vol. 7, p. 3, 1995.

[95] H. Y. W. Yang, Guoxuan Qin, Zhenqiang Ma, Jesper Berggren, Mattias Hammar, Richard Soref, Weidong Zhou, "Large-area InP-based crystalline nanomembrane flexible photodetectors," *Applied Physics Letters,* vol. 96, p. 3, 2010.

BIOGRAPHICAL INFORMATION

Hongjun Yang is a PhD candidate at the University of Texas at Arlington and a student member of IEEE and LEOS; he received his B.S. and M.S.E. degrees both in Electrical Engineering from Jilin University in 2000 and in 2004, respectively. He has been working in Nanophotonic Lab (NPLAB) led by Dr. Weidong Zhou since 2005, with focusing various active research projects in the areas of photonic crystal infrared photodetectors, silicon based detectors, sources, and modulators, cost effective solar cells, VCSELs, etc, based on photonic crystals, semiconductor nanomembranes, quantum dots, and other nanoscale structure.